

Twisted bilayer graphene. I. Matrix elements, approximations, perturbation theory, and a $k \cdot p$ two-band model

B. Andrei Bernevig,^{1,*} Zhi-Da Song,¹ Nicolas Regnault,^{1,2} and Biao Lian^{1,†}

¹*Department of Physics, Princeton University, Princeton, New Jersey 08544, USA*

²*Laboratoire de Physique de l'Ecole normale supérieure, ENS, Université PSL, CNRS, Sorbonne Université, Université Paris-Diderot, Sorbonne Paris Cité, Paris, France*



(Received 28 October 2020; revised 15 April 2021; accepted 16 April 2021; published 11 May 2021)

We investigate the twisted bilayer graphene (TBG) model of Bistritzer and MacDonald (BM) [Bistritzer and MacDonald, *Proc. Natl. Acad. Sci.* **108**, 12233 (2011)] to obtain an analytic understanding of its energetics and wave functions needed for many-body calculations. We provide an approximation scheme for the wave functions of the BM model, which first elucidates why the BM K_M -point centered original calculation containing only four plane waves provides a good analytical value for the first magic angle ($\theta_M \approx 1^\circ$). The approximation scheme also elucidates why most of the many-body matrix elements in the Coulomb Hamiltonian projected to the active bands can be neglected. By applying our approximation scheme at the first magic angle to a Γ_M -point centered model of six plane waves, we analytically understand the reason for the small Γ_M -point gap between the active and passive bands in the isotropic limit $w_0 = w_1$. Furthermore, we analytically calculate the group velocities of the passive bands in the isotropic limit, and show that they are *almost* doubly degenerate, even away from the Γ_M point, where no symmetry forces them to be. Furthermore, moving away from the Γ_M and K_M points, we provide an explicit analytical perturbative understanding as to why the TBG bands are flat at the first magic angle, despite the first magic angle is defined by only requiring a vanishing K_M -point Dirac velocity. We derive analytically a connected “magic manifold” $w_1 = 2\sqrt{1 + w_0^2} - \sqrt{2 + 3w_0^2}$, on which the bands remain extremely flat as w_0 is tuned between the isotropic ($w_0 = w_1$) and chiral ($w_0 = 0$) limits. We analytically show why going away from the isotropic limit by making w_0 less (but not larger) than w_1 increases the Γ_M -point gap between the active and the passive bands. Finally, by perturbation theory, we provide an analytic Γ_M point $k \cdot p$ two-band model that reproduces the TBG band structure and eigenstates within a certain w_0, w_1 parameter range. Further refinement of this model are discussed, which suggest a possible faithful representation of the TBG bands by a two-band Γ_M point $k \cdot p$ model in the full w_0, w_1 parameter range.

DOI: [10.1103/PhysRevB.103.205411](https://doi.org/10.1103/PhysRevB.103.205411)

I. INTRODUCTION

The interacting phases in twisted bilayer graphene (TBG) are one of the most important new discoveries of the last few years in condensed matter physics [1–111]. The theoretical prediction that interacting phases would appear in this system was made based on the appearance of flat bands in the noninteracting Bistritzer-MacDonald (BM) Hamiltonian [1]. This Hamiltonian is at the starting point of the understanding of every aspect of strongly correlated TBG (and other moiré systems) physics [2–27]. Remarkably, it even predicts quite accurately the so-called “magic angles” at which the bands become flat, and is versatile enough to accommodate the presence of different hoppings in between the AA and the AB stacking regions of the moiré lattice. The BM Hamiltonian is in fact a large class of $k \cdot p$ models, which we will call BM-like models, where translational symmetry emerges at a small twist angle even though the actual sample does not have an exact lattice commensuration.

This paper is the first of a series of six papers on TBG [107–111], for which we present a short summary here. In this paper we investigate the spectra and matrix elements of the single-particle BM model by studying the $k \cdot p$ expansion of the BM model at Γ_M point of the moiré Brillouin zone. In TBG II [107] we prove that the BM model with the particle-hole (PH) symmetry defined in Ref. [43] is always *stable topological*, rather than fragile topological as revealed without PH symmetry [43–45,76]. We further study TBG with Coulomb interactions in Refs. [108–111]. In TBG III [108] we show that the TBG interaction Hamiltonian projected into any number of bands is always a Kang-Vafeek type [71] positive semi-definite Hamiltonian (PSDH), and generically exhibit an enlarged $U(4)$ symmetry in the flat band limit due to the PH symmetry. This $U(4)$ symmetry for the lowest eight bands (two per spin valley) was previously shown in Ref. [72]. We further reveal two chiral-flat limits, in both of which the symmetry is further enhanced into $U(4) \times U(4)$ for any number of flat bands. The $U(4) \times U(4)$ symmetry for the lowest eight flat bands in the first chiral limit was first discovered in Ref. [72]. With kinetic energy, the symmetry in the chiral limits will be lowered into $U(4)$. TBG in the second chiral limit is also proved in TBG II [107] to be a perfect

*bernevig@princeton.edu

†biao@princeton.edu

metal without single-particle gaps [112]. In TBG IV [109], under a condition called flat metric condition (FMC) which is defined in this paper [Eq. (20)], we derive a series of exact insulator ground/low-energy states of the TBG PSDH within the lowest eight bands at integer fillings in the first chiral-flat limit and even fillings in the nonchiral-flat limit, which can be understood as $U(4) \times U(4)$ or $U(4)$ ferromagnets. We also examine their perturbations away from these limits. In the first chiral-flat limit, we find exactly degenerate ground states of Chern numbers $\nu_C = 4 - |\nu|, 2 - |\nu|, \dots, |\nu| - 4$ at integer filling ν relative to the charge neutrality. Away from the chiral limit, we find the Chern number 0 (± 1) state is favored at even (odd) fillings. With kinetic energy further turned on, up to second order perturbations, these states are intervalley coherent if their Chern number $|\nu_C| < 4 - |\nu|$, and are valley polarized if $|\nu_C| = 4 - |\nu|$. At even fillings, this agrees with the K-IVC state proposed in Ref. [72]. At fillings $\nu = \pm 1, \pm 2$, we also predict a first order phase transition from the lowest to the highest Chern number states in magnetic field, which is supported by evidences in recent experiments [14–16, 24–27]. In TBG V [110] we further derive a series of exact charge 0, $\pm 1, \pm 2$ excited states in the (first) chiral-flat and nonchiral-flat limits. In particular, the exact charge neutral excitations include the Goldstone modes (which are quadratic). This allows us to predict the charge gaps and Goldstone stiffness. In the last paper of our series TBG VI [111] we present a full Hilbert space exact diagonalization (ED) study at fillings $\nu = -3, -2, -1$ of the projected TBG Hamiltonian in the lowest eight bands. In the (first) chiral-flat and nonchiral-flat limits, our ED calculation with FMC verified that the exact ground states we derived in TBG IV [109] are the only ground states at nonzero integer fillings. We further show that in the (first) chiral-flat limit, the exact charge ± 1 excitations we found in TBG V [110] are the lowest excitations for almost all nonzero integer fillings. In the nonchiral case with kinetic energy, we find the $\nu = -3$ ground state to be Chern number ± 1 insulators at small w_0/w_1 [ratio of AA and AB interlayer hoppings, see Eq. (4)], while undergoing a phase transition to other phases at large w_0/w_1 , in agreement with the recent density matrix renormalization group studies [80,81]. For $\nu = -2$, while we are restricted within the fully valley polarized sectors, we find the ground state prefers ferromagnetic (spin singlet) in the nonchiral-flat (chiral-nonflat) limit, in agreement with the perturbation analysis in Refs. [72,109].

To date, most of our understanding of the BM-like models comes from numerical calculations of the flat bands, which can be performed in a momentum lattice of many moiré Brillouin zones, with a cutoff on their number. The finer details of the band structure so far seem to be peculiarities that vary with different twisting angles. However, with the advent of interacting calculations, where the Coulomb interaction is projected into the active, flat bands of TBG, a deeper, analytic understanding of the flat bands in TBG is needed. In particular, there is a clear need for an understanding of what quantitative and qualitative properties are not band-structure details. So far the analytic methods have produced the following results: by solving a model with only four plane waves (momentum space lattice sites, on which the BM is defined), Bistritzer and MacDonald [1] found a value for the twist angle for which the Dirac velocity at the K_M moiré point vanishes. This is

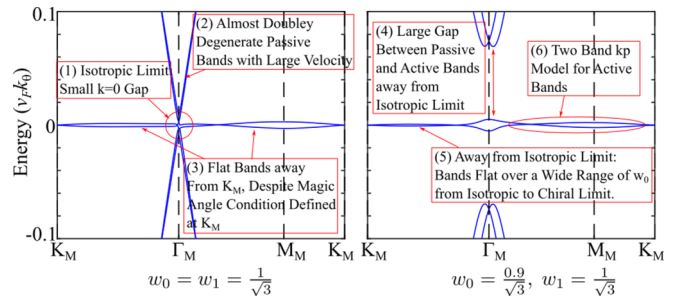


FIG. 1. Several quantitative characteristics of the Bistritzer and MacDonald model that require explanation. In particular, an analytic understanding of the active band flatness is available only in the chiral limit $w_0 = 0$. However, the band is very flat far away from the chiral limit. Several other features of the bands are pointed out.

called the magic angle. In fact, the full band away from the K_M point is flat, a fact which is not analytically understood. A further analytic result is the discovery that, in a limit of vanishing AA hopping, there are angles for which the band is *exactly* flat. This limit, called the *chiral limit* [37], has an extra chiral symmetry. However, it is not analytically known why the bands remain flat in the whole range of AA coupling between the isotropic limit ($AA = AB$ coupling) and the chiral limit. We note that the realistic magic angle TBG is in between these two limits due to lattice relaxations [113–116]. A last analytical result is the proof that, when particle-hole symmetry is maintained in the BM model [43], the graphene active bands are topological [42–47, 76, 117, 118].

This leaves a large series of unanswered questions. Rather than listing them in writing, we find it more intuitive to visualize the questions in a plot of the band structure of TBG in the isotropic limit at the magic angle and away from it, towards the chiral limit. In Fig. 1 we plot the TBG low-energy band structure in the moiré Brillouin zone, and the questions that will be answered in the current paper. To distinguish them with the high symmetry points (Γ, M, K, K') of the monolayer graphene Brillouin zone (BZ), we use a subindex M to denote the high symmetry points (Γ_M, M_M, K_M, K'_M) of the moiré BZ (MBZ). Some salient features of this band structure are: (1) In the isotropic limit, around the first magic angle, it is hard to obtain two separate flat bands; it is hard to stabilize the gap to passive bands over a wide range of angles smaller than the first magic angle. In fact, Ref. [43] computes the active bands separated regions as a function of twist angle, and finds a large region of gapless phases around the first magic angle. (2) The passive bands in the isotropic limit are *almost* doubly degenerate, even away from the Γ_M point, where no symmetry forces them to be. Moreover, their group velocities seem very high, i.e., they are very dispersive. (3) While the analytic calculation of the magic angle [1] shows that the Dirac velocity vanishes in the isotropic limit at AA -coupling $w_0 = 1/\sqrt{3}$ (in the appropriate units, see below), it does not explain why the band is so flat even away from the Dirac point, for example on the K_M - Γ_M - M_M - K_M line. (4) Away from the isotropic limit, while keeping $w_1 = 1/\sqrt{3}$, the gap between the active and passive bands increases immediately, while the bandwidth of the active bands does not increase. (5) The flat bands remain flat, over the wide range of $w_0 \in [0, 1/\sqrt{3}]$,

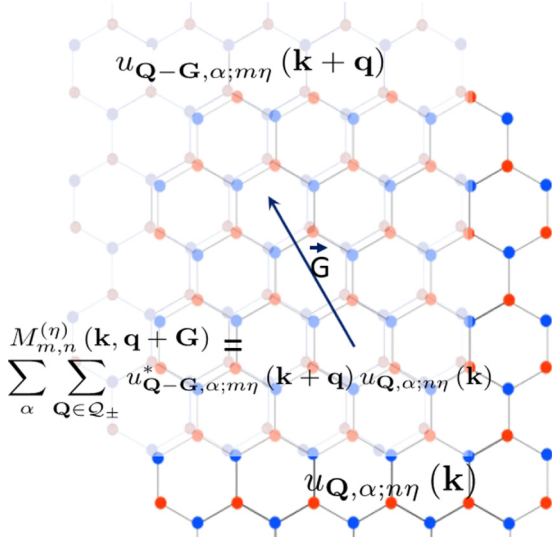


FIG. 2. Matrix elements needed for the interacting problem. Specifically, the form factors $M_{m,n}^{(\eta)}(\mathbf{k}, \mathbf{q} + \mathbf{G}) = \sum_{\alpha} \sum_{\mathbf{Q} \in \mathcal{Q}_{\pm}} u_{\mathbf{Q}-\mathbf{G}, \alpha; m\eta}^*(\mathbf{k} + \mathbf{q}) u_{\mathbf{Q}, \alpha; n\eta}(\mathbf{k})$ of the Coulomb interaction are needed. They correspond to the overlap of the Bloch state at momentum \mathbf{k} , on the momentum lattice \mathbf{Q} , $u_{\mathbf{Q}, \alpha; n\eta}(\mathbf{k})$ with the Bloch state at momentum $\mathbf{q} + \mathbf{k}$ on the momentum lattice $\mathbf{Q} + \mathbf{G}$, $u_{\mathbf{Q}-\mathbf{G}, \alpha; m\eta}^*(\mathbf{k} + \mathbf{q})$. Here m, n are band indices, $\alpha = A, B$ is the graphene sublattice index, η is the valley index, \mathbf{G} is a reciprocal momentum, and \mathbf{Q} is the honeycomb momentum lattice generated by the moiré reciprocal vectors shown in this figure.

from chiral to the isotropic limit. Also, our observation (6) in Fig. 1 shows that since the gap between the active and passive bands is large in the chiral limit compared to the bandwidth of active bands, a possible $k \cdot p$ Hamiltonian for the active bands might be possible.

A further motivation for the analytic investigation of the TBG Bistritzer-MacDonald model is to understand the behavior of the matrix elements $M_{m,n}^{(\eta)}(\mathbf{k}, \mathbf{q} + \mathbf{G}) = \sum_{\alpha} \sum_{\mathbf{Q} \in \mathcal{Q}_{\pm}} u_{\mathbf{Q}-\mathbf{G}, \alpha; m\eta}^*(\mathbf{k} + \mathbf{q}) u_{\mathbf{Q}, \alpha; n\eta}(\mathbf{k})$ as a function of \mathbf{G} , which we call the *form factor* (or *overlap matrix*). These are the overlaps of different Bloch states in the TBG momentum space lattice (see Fig. 2) and their behavior is important for the form factors of the interacting problem [108,109]. These will be of crucial importance for the many-body matrix elements [107,111] as well as for justifying the approximations made in obtaining exact analytic expressions for the many-body ground states [109] and their excitations [110].

We provide an analytic answer to all the above questions and observations. We will focus on the vicinity of the first magic angle. We first provide an analytic perturbative framework in which to understand the BM model, and show that for the two flat bands around the first magic angle, only a very small number of momentum shells is needed. We justify our framework analytically, and check it numerically. This perturbative framework also shows that $M_{m,n}^{(\eta)}(\mathbf{k}, \mathbf{q} + \mathbf{G})$ is negligible for \mathbf{G} more than two times the moiré BZ (MBZ) momentum—at the first magic angle, irrespective of \mathbf{k}, \mathbf{q} . We then provide two approximate models involving a very small number of momentum lattice sites, the tripod model (K_M centered, also discussed in Ref. [1]), and a new, Γ_M centered

model. The tripod model captures the physics around the K_M point (but not around the Γ_M point), and we show that the Dirac velocity vanishes when $w_1 = 1/\sqrt{3}$ irrespective of w_0 . The Γ_M centered model captures the physics around the Γ_M point extremely well, as well as the physics around the K_M point. Moreover, an approximation of the Γ_M centered model with only six plane waves, which we call the hexagon model, has an analytic sixfold exact degeneracy at the Γ_M point in the isotropic limit $w_1 = w_0 = 1/\sqrt{3}$, which is the reason for feature (1) in Fig. 1. By performing a further perturbative theory in these six degenerate bands away from the Γ_M point, we obtain a model with an exact flat band at zero energy on the Γ_M - K_M line, and almost flat bands on the Γ_M - M_M line, answering (3) in Fig. 1. In the same perturbative model, the velocity of the dispersive bands—which can be shown to be degenerate—can be computed and found to be the same with the bare Dirac velocity (with some directional dependence), answering (2) in Fig. 1. Away from the isotropic limit, our perturbative model, which we still show to be valid for $w_0 \leq w_1$ (but not for $w_0 \gg w_1$), allows for finding the analytic energy expressions at the Γ_M point, and seeing a strong dependence on w_0 answering (3) in Fig. 1. At the same time, one can obtain *all* the eigenstates of the hexagon model at the Γ_M point after tedious algebra, which can serve as the starting point of a perturbative $k \cdot p$ expansion of the two-active band Hamiltonians. With this, we provide an approximate two-band continuum model of the active bands, and find the manifold $w_1(w_0) = 2\sqrt{1 + w_0^2} - \sqrt{2 + 3w_0^2}$ with $w_0 \in [0, 1/\sqrt{3}]$, where the bandwidth of the active bands is the smallest, in this approximation. The radius of convergence for the $k \cdot p$ expansion is great around the Γ_M point but is not particularly good around the K_M point for all w_0, w_1 parameters, but can be improved by adding more shells perturbatively, which we leave for further work. A series of useful matrix element conventions are also provided.

II. NEW PERTURBATION THEORY FRAMEWORK FOR LOW-ENERGY STATES IN $k \cdot p$ CONTINUUM MODELS

In this section we provide a general perturbation theory for the $k \cdot p$ BM-type Hamiltonians that exist in moiré lattices. We exemplify it in the TBG BM model, but the general characteristics of this model allow this perturbation theory to be generalizable to other moiré system. The TBG BM Hamiltonian is defined on a momentum lattice of plane waves. Its symmetries and expressions have been extensively exposed in the literature (including in our paper [107]), and we only briefly mention them here for consistency. We first define $k_{\theta} = 2|K| \sin(\theta/2)$ as the momentum difference between K point of the lower layer and K point of the upper layer of TBG, and denote the Dirac Fermi velocity of monolayer graphene as v_F . To make the TBG BM model dimensionless, we measure all the energies in units of $v_F k_{\theta}$, and measure all the momentum in units of k_{θ} . Namely, any quantity $E(\mathbf{k})$ with the dimension of energy (momentum) is redefined as dimensionless parameters

$$E \rightarrow E/(v_F k_{\theta}), \quad \mathbf{k} \rightarrow \mathbf{k}/k_{\theta}. \quad (1)$$

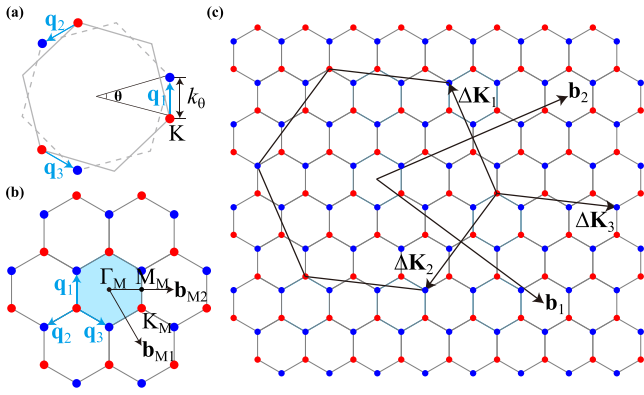


FIG. 3. (a) The Brillouin zones of two graphene layers. The gray solid line and red dots represent the BZ and Dirac cones of the top layer, and the gray dashed line and blue dots represent the BZ and Dirac cones of the bottom layer. (b) The lattice formed by adding $\mathbf{q}_{1,2,3}$ iteratively. Red and blue circles represent \mathcal{Q}_+ and \mathcal{Q}_- , respectively. (c) Relation of graphene BZ and moiré BZ in the commensurate case. Here we take the graphene BZ reciprocal vectors $\mathbf{b}_1 = 3\mathbf{b}_{M1} + 2\mathbf{b}_{M2}$, $\mathbf{b}_2 = -2\mathbf{b}_{M1} + 5\mathbf{b}_{M2}$.

We will then work with the dimensionless single particle Hamiltonian for the valley $\eta = +$, which in the second quantized form reads [1,43,107]

$$\hat{H}_0^{(+)} = \sum_{\mathbf{k} \in \text{MBZ}} \sum_{s\alpha\beta} \sum_{\mathbf{Q} \in \mathcal{Q}_{\pm}} H_{\mathbf{Q}\alpha, \mathbf{Q}'\beta}(\mathbf{k}) c_{\mathbf{k}, \mathbf{Q}, +, \alpha s}^{\dagger} c_{\mathbf{k}, \mathbf{Q}', +, \beta s}, \quad (2)$$

where MBZ stands for moiré BZ, the momentum \mathbf{k} is measured from the center (Γ_M as shown in Fig. 3) point of the MBZ, $s = \uparrow, \downarrow$ is spin, and α, β denotes the two indices of A, B sublattices. Here the dimensionless first quantized Hamiltonian $H_{\mathbf{Q}\alpha, \mathbf{Q}'\beta}(\mathbf{k})$ is given by

$$H_{\mathbf{Q}\alpha, \mathbf{Q}'\beta}(\mathbf{k}) = \delta_{\mathbf{Q}, \mathbf{Q}'} [(\mathbf{k} - \mathbf{Q}) \cdot \boldsymbol{\sigma}]_{\alpha\beta} + \sum_{j=1}^3 (\delta_{\mathbf{Q}-\mathbf{Q}', \mathbf{q}_j} + \delta_{\mathbf{Q}'-\mathbf{Q}, \mathbf{q}_j}) (T_j)_{\alpha\beta}, \quad (3)$$

where

$$T_j = w_0 \sigma_0 + w_1 \left[\cos \frac{2\pi}{3} (j-1) \sigma_x + \sin \frac{2\pi}{3} (j-1) \sigma_y \right], \quad (4)$$

with w_0 being the interlayer AA hopping and w_1 being the interlayer AB hopping, $\boldsymbol{\sigma} = (\sigma_x, \sigma_y)$, and $\sigma_{0,x,y,z}$ stand for the identity and Pauli matrices in the two-dimensional sublattice space. \mathbf{k} takes value in MBZ, and $\mathbf{k} = \mathbf{0}$ corresponds to the Γ_M point in the moiré BZ. We define \mathbf{q}_1 as the difference between the K momentum of the lower layer of graphene and the rotated K of the upper layer, and \mathbf{q}_2 and \mathbf{q}_3 as the C_{3z} and C_{3z}^{-1} rotations of \mathbf{q}_1 (see Fig. 3). The moiré reciprocal lattice \mathcal{Q}_0 is then generated by the moiré reciprocal vectors $\mathbf{b}_{M1} = \mathbf{q}_3 - \mathbf{q}_1$ and $\mathbf{b}_{M2} = \mathbf{q}_3 - \mathbf{q}_2$, which contains the origin. We also define $\mathcal{Q}_+ = \mathbf{q}_1 + \mathcal{Q}_0$ and $\mathcal{Q}_- = -\mathbf{q}_1 + \mathcal{Q}_0$ as the moiré reciprocal lattices shifted by \mathbf{q}_1 and $-\mathbf{q}_1$, respectively. $\mathcal{Q} \in \mathcal{Q}_{\pm}$ is then in the combined momentum lattice $\mathcal{Q}_+ \oplus \mathcal{Q}_-$, which is a honeycomb lattice. For valley $\eta = +$, the fermion degrees of freedom $c_{\mathbf{k}, \mathbf{Q}, +, \alpha s}^{\dagger}$ with $\mathbf{Q} \in \mathcal{Q}_+$ and $\mathbf{Q} \in \mathcal{Q}_-$ are from layers 1 and 2, respectively. Since energy and momen-

tum are measured in units of $v_F k_{\theta}$ and k_{θ} , we have that $|\mathbf{q}_i| = 1$, and both w_0 and w_1 are dimensionless energies. It should be noticed that, for infinite cutoff in the lattice \mathcal{Q} , we have $c_{\mathbf{k}+\mathbf{b}_{Mi}, \mathbf{Q}, \eta\alpha s}^{\dagger} = c_{\mathbf{k}, \mathbf{Q}-\mathbf{b}_{Mi}, \eta\alpha s}^{\dagger} \neq c_{\mathbf{k}, \mathbf{Q}, \eta\alpha s}^{\dagger}$, as proved in Refs. [43,107]. In practice, we always choose a finite cutoff $\Lambda_{\mathcal{Q}}$ for \mathcal{Q} ($\Lambda_{\mathcal{Q}}$ denotes the set of \mathcal{Q} sites kept).

We note that in the Hamiltonian (3) we have adopted the zero angle approximation [1,107], namely, we have approximated the Dirac kinetic energy $\mathbf{k} \cdot \boldsymbol{\sigma}_{\pm\theta/2}$ (\pm for layers 1 and 2, respectively) as $\mathbf{k} \cdot \boldsymbol{\sigma}$, where $\boldsymbol{\sigma}_{\pm\theta/2}$ are the Pauli matrices $\boldsymbol{\sigma}$ rotated as a vector by angle $\pm\theta/2$ about the z axis. With the zero angle approximation, the Hamiltonian (3) acquires a unitary particle-hole symmetry [43], which is studied in detail in another paper of ours [107]. In the absence of the zero angle approximation, the particle-hole symmetry is only broken up to 1% [107] near the first magic angle, and is exact in the (first) chiral limit $w_0 = 0$ [106]. We also note that different variants of the TBG BM model exist in the literature, which further include nonlocal tunnelings, interlayer strains, or \mathbf{k} dependent tunnelings [119–122]. However, we shall only focus on the BM model in Eq. (3) in this paper.

It is the cutoff $\Lambda_{\mathcal{Q}}$ that we are after: we need to quantize what is the proper cutoff $\mathbf{Q} \in \Lambda_{\mathcal{Q}}$ in order to obtain a fast convergence of the Hamiltonian. We devise a perturbation theory which gives us the error of taking a given cutoff in the diagonalization of the Hamiltonian in Eq. (3). For the first magic angle we will see that this cutoff is particularly small, allowing for analytic results.

A. Setting up the shell numbering of the momentum lattice and Hamiltonian

We now consider the question of what momentum shell cutoff $\Lambda_{\mathcal{Q}}$ should we keep in performing a perturbation theory of the BM model. In effect, considering an infinite cutoff for the \mathcal{Q} lattice, we can build the BM model centered around any point \mathbf{k}_0 in the MBZ, by sending

$$\mathbf{k} \rightarrow \mathbf{k} - \mathbf{k}_0, \quad \mathbf{Q} \rightarrow \mathbf{Q} - \mathbf{k}_0 \quad (5)$$

in Eq. (3); however, it makes sense to pick \mathbf{k}_0 as a high-symmetry point in the MBZ, and try to impose a finite cutoff $\Lambda_{\mathcal{Q}}$ in the shifted lattice \mathcal{Q} . Two important shifted lattices \mathbf{k}_0 can be envisioned, see Fig. 4. These lattices will be developed and analyzed in Sec. III; here we only focus on the perturbative framework of Eq. (3), which is the same for either of these two lattices (and in fact, on a lattice with any \mathbf{k}_0 center).

We introduce a numbering of the “shells” in momentum space \mathcal{Q} on this lattice. In the K_M -centered lattice [Fig. 4(b)] which is a set of hexagonal lattices but centered at one of the “sites” (the K_M point, corresponding to the choice $\mathbf{k}_0 = -\mathbf{q}_1$), the sites of shells n are denoted An_i , with $n-1$ being the minimal graph distance (minimal number of bonds traveled on the honeycomb lattice from one site to another) from the center $A1_1$, while i goes to the number of \mathcal{Q} sites with the same graph distance $n-1$. The truncation in \mathcal{Q} corresponds to a truncation in the graph distance $n-1$. In particular, with lattice \mathcal{Q} centered at the K_M point, the momentum hopping T_j in the BM Hamiltonian Eq. (3) then *only* happens between sites in two different shells $n \leftrightarrow n+1$ but not between sites in the same shell. The simplest version of this model, with a

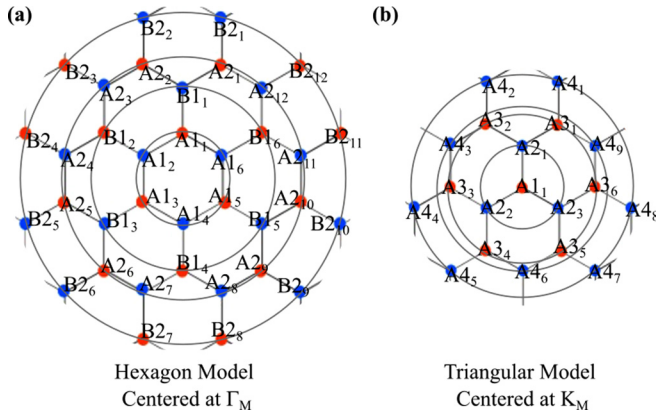


FIG. 4. Lattices centered around momentum \mathbf{k}_0 on which one can calculate the TBG Hamiltonian. (a) The hexagon centered model (Γ_M -centered model, in which we build “shells” by graph distance from the hexagon centered at the Γ_M point. The circles denote the different shells, although going to a larger graph distance will make the circles into hexagons. There are two different types of subshells in each shell, the A and the B subshells in this model. The A shells connect to the B shells, but the A sites within a shell also contain hoppings within themselves. The B sites hop only to A sites. (b) The triangle centered at the K_M -point model in which we build shells by graph distance from the K_M point centered at the origin. The circles denote the different shells, although going to a larger graph distance will make the circles into triangles. There are only one type of shells, the A shells in this model. The A sites within a shell do not hop to other sites within each shell.

truncation at $n = 2$, with sites $A1_1$ and $A2_1, A2_2, A2_3$ was used by Bistritzer and MacDonald to show the presence of a “magic angle”—defined as the angle for which the Dirac velocity vanishes. We call this the tripod model. This truncated model (the tripod model) does not respect the *exact* C_{2x} symmetry, although it becomes asymptotically good as more shells are added. The magic angle also does not explain analytically the flatness of bands, since it only considers the velocity vanishing at one point K_M . However, the value obtained by BM [1] for the first magic angle is impressive: despite considering only two shells (four sites), and despite obtaining this angle from the vanishing velocity of bands at only one point (K_M in the BZ), the bands do not change much after adding more shells. Moreover, they are flat throughout the whole BZ, not only around the K_M point. The Dirac velocity also does not change considerably upon introducing more shells.

We now introduced a yet unsolved lattice, the Γ_M -centered model in Fig. 4(a), which corresponds to the choice $\mathbf{k}_0 = \mathbf{0}$ in Eq. (5). This model, which we call Γ_M centered was not solved by BM, perhaps because of the larger Hilbert space dimension than the K_M -centered one. It however respects all the symmetries of the TBG (except Bloch periodicity, which is only fully recovered in the large cutoff Λ_Q limit) at any finite number of shells and not only in the large shell number limit. While not relevant for the perturbation theory described here, we find it useful to partition one shell n in the Γ_M -centered lattice into two subshells An and Bn , each of which has $6n$ sites. The first shell is $A1$ given by the six corners of the first MBZ; then we define An as the shell with a minimal graph distance $2(n - 1)$ to shell $A1$, and Bn as the shell with a minimal graph distance

$2n - 1$ to shell $A1$. An_i and Bn_i where $i = 1, \dots, 6n$ is the index of sites in the subshell An or Bn . The partitioning in subshells is useful when we realize that the hopping T_i in the BM Hamiltonian Eq. (3) can only happen between An and Bn shells, between Bn and $An + 1$ shells, and *within* an An shell, but *not* within the same Bn shell. In Appendix A we provide an explicit efficient way of implementing the scattering matrix elements of the BM Hamiltonian Eq. (3), and provide a block matrix form of the BM Hamiltonian in the shell basis defined here. Written compactly, the expanded matrix elements in Appendix A read

$$(H_{An,An})_{\mathbf{Q}_1, \mathbf{Q}_2} = \begin{cases} T_j & \text{if } \mathbf{Q}_1 - \mathbf{Q}_2 = \pm \mathbf{q}_j, \\ 0 & \text{otherwise} \end{cases}, \quad (6)$$

for the hopping terms, and similarly for $H_{An, Bn}$ where $\mathbf{Q}_1, \mathbf{Q}_2$ are the initial and final momenta in their respective shells. Finally for \mathbf{k} -dependent dispersion we take a linearized model:

$$(H_{k, An/Bn})_{\mathbf{Q}_1, \mathbf{Q}_2} = (\mathbf{k} - \mathbf{Q}_1) \cdot \sigma \delta_{\mathbf{Q}_1, \mathbf{Q}_2}, \quad (7)$$

which is accurate in the small-angle low-energy approximations we make. Recall that the momentum is measured in units of $k_\theta = 2|K| \sin(\theta/2)$ with θ the twist angle, while the energy (and Hamiltonian matrix elements) are in units of $v_F k_\theta$. We may now write the dimensionless BM Hamiltonian $H(\mathbf{k})$ in Eq. (3) in block form as

$$H = \begin{pmatrix} H_{kA1} + H_{A1, A1} & H_{A1, B1} & 0 & \dots \\ H_{A1, B1}^\dagger & H_{kB1} & H_{B1, A2} & \dots \\ 0 & H_{B1, A2}^\dagger & H_{kA2} + H_{A2, A2} & \dots \\ \vdots & 0 & \ddots & \ddots \end{pmatrix} \equiv \begin{pmatrix} M_1 & N_1 & 0 & 0 & \dots & 0 & 0 \\ N_1^\dagger & M_2 & N_2 & 0 & \dots & 0 & 0 \\ 0 & N_2^\dagger & M_3 & N_3 & \dots & 0 & 0 \\ \dots & \dots & \dots & \dots & \dots & \dots & \dots \\ 0 & 0 & 0 & 0 & \dots & M_{L-1} & N_{L-1} \\ 0 & 0 & 0 & 0 & \dots & N_{L-1}^\dagger & M_L \end{pmatrix}, \quad (8)$$

where L is the shell cutoff that we choose. In the above equation, the M, N block form of the matrix is a schematic, in the sense that both the Γ_M -centered model Fig. 4(a) and the K_M -centered model Fig. 4(b) can be written in this form, albeit with different $M_n, N_n, n = 1, \dots, L$. Also, each M_n depends on \mathbf{k} , which for space purposes was not explicitly written in Eq. (8).

B. General Hamiltonian perturbation for bands close to zero energy with ramp-up term

In general, Eq. (8), with generic matrices M_i, N_i represents *any* Hamiltonian with short range hopping (here on a momentum lattice), and not much progress can be made. However, for our BM Hamiltonians, we *know* several facts which render them special:

(1) The Hamiltonian in Eq. (3) has very flat bands, at close to zero energy $|E| \leq 0.02 v_F k_\theta$. Numerically, the energy of the flat bands $\ll w_1$ and w_0 , since numerically we know that the first magic angle happens at w_1 (or w_0) around $1/\sqrt{3}$.

(2) The block-diagonal terms M_n contain a ramping up diagonal term Eq. (7), of eigenvalue $|\mathbf{k} - \mathbf{Q}|$. The \mathbf{k} momentum

runs in the first MBZ, which means that $|\mathbf{k}| \leq 1$. Since Q for the n th shell is proportional to n , higher order shells contribute larger terms to the diagonal of the BM Hamiltonian.

We now show that, despite the higher shell diagonal terms being the largest in the BM Hamiltonian, they contribute exponentially little to the physics of the low-energy (flat) bands. This should be a generic property of the moiré systems.

The M_n, N_n Block Hamiltonian Eq. (8) acts on the spinor wave function $(\psi_1, \psi_2, \psi_3, \dots, \psi_{L-1}, \psi_L)$ where the ψ_n 's are the components of the wave function on the shells $n = 1, 2, 3, \dots, L-1, L$, and L is the cutoff shell. Notice that they likely have different dimensions: in the Γ_M -centered model, ψ_1 is a 12-dimensional spinor (six vertices of the first hexagon momentum Q —for subshell $A1_i$, $i = 1, \dots, 6$ —times 2 for the $\alpha\beta$ indices), ψ_2 is also a 12-dimensional spinor (six legs coming out of the vertices of the first hexagon momentum Q —for subshell $B1_i$, $i = 1, \dots, 6$ —times 2 for the $\alpha\beta$ in-

dices), ψ_3 is a 24-dimensional spinor (12 vertices of the momentum Q —for subshell $A2_i$, $i = 1, \dots, 12$ —times 2 for the $\alpha\beta$ indices), and ψ_4 is also a 24-dimensional spinor (12 legs coming out of the vertices of the previous momentum shell Q —for subshell $B2_i$, $i = 1, \dots, 12$ —times 2 for the $\alpha\beta$ indices), etc. To diagonalize H we write down the action of H in Eq. (8) on the wave function $\psi = (\psi_1, \psi_2, \dots, \psi_L)$:

$$\begin{aligned} M_1\psi_1 + N_1\psi_2 &= E\psi_1, \\ &\dots \\ N_{n-1}^\dagger\psi_{n-1} + M_n\psi_n + N_n\psi_{n+1} &= E\psi_n, \\ &\dots \\ N_{L-1}^\dagger\psi_{L-1} + M_L\psi_L &= E\psi_L, \end{aligned} \quad (9)$$

and solve iteratively for ψ_1 starting from the *last* shell. We find that

$$\begin{aligned} \psi_L &= (E - M_L)^{-1}N_{L-1}^\dagger\psi_{L-1}, \\ \psi_{L-1} &= [E - M_{L-1} - N_{L-1}(E - M_L)^{-1}N_{L-1}^\dagger]^{-1}N_{L-2}^\dagger\psi_{L-2}, \\ \psi_{L-2} &= \{E - M_{L-2} - N_{L-2}[E - M_{L-1} - N_{L-1}(E - M_L)^{-1}N_{L-1}^\dagger]^{-1}N_{L-2}^\dagger\}^{-1}N_{L-3}^\dagger\psi_{L-3} \\ &\dots \end{aligned} \quad (10)$$

We notice three main properties:

(1) $M_n \approx n$ for large shells $n \gg 1$ is generically an invertible matrix with eigenvalues of the order $\pm n$ for the n th shell. This is because M_n is just the ramp-up term, block diagonal with the diagonal being $(\mathbf{k} - \mathbf{Q}) \cdot \boldsymbol{\sigma}$ for Q in the n th subshell of B type; if the subshell is of A type, then the matrix is still generically invertible, as it contains the diagonal term $(\mathbf{k} - \mathbf{Q}) \cdot \boldsymbol{\sigma}$ plus the small (since $w_0, w_1 \approx 1/\sqrt{3}$) hopping Hamiltonian $H_{An,An}$ (see Appendix A). Nonetheless, because the magnitude of the momentum term increases linearly with $|\mathbf{k} - \mathbf{Q}| \gg 1$ for momenta \mathbf{Q} outside the first two shells $n > 2$, while the hopping term has constant magnitude, H_{kAn} dominates the BM Hamiltonian.

(2) Since we are interested in the flat bands $E \approx 0$ ($E \approx 0.02$ in $v_F k_\theta$), we can expand in E/M_n terms, especially after the first $n > 2$ shells, and keep only the zeroth and first order terms. We use

$$(E - M)^{-1} \approx -M^{-1} - M^{-1}EM^{-1} \quad (11)$$

if the eigenvalues of E are smaller than those of $ME \ll M$.

(3) For the first magic angle, the off-diagonal terms are also smaller than the diagonal terms, for the first magic angle, and for $|\mathbf{Q}| \geq 2$, we have that $N_{n-1}M_n^{-1}N_{n-1}^\dagger \ll 1$ for $n \geq 2$ and for $w_0, w_1 \approx 1/\sqrt{3}$ (more details on this will be given later).

With these approximations, we obtain that the general solution is

$$\psi_n = (EP_n - M_n + R_n)^{-1}N_{n-1}^\dagger\psi_{n-1}m, \quad (12)$$

where P_n is defined recursively as

$$P_{L-n} = N_{L-n}M_{L-n+1}^{-1}P_{L-n+1}M_{L-n+1}^{-1}N_{L-n}^\dagger + 1 \quad (13)$$

subject to $P_L = 1$ and R_n is

$$\begin{aligned} R_{L-n} &= N_{L-n}M_{L-n+1}^{-1}R_{L-n+1}M_{L-n+1}^{-1}N_{L-n}^\dagger \\ &\quad + N_{L-n}M_{L-n+1}^{-1}N_{L-n}^\dagger, \end{aligned} \quad (14)$$

with $R_L = 0$, $R_{L-1} = N_{L-1}M_L^{-1}N_{L-1}^\dagger$, $P_L = 1$. This continues until the first shell, where we have

$$\psi_2 = [EP_2 - M_2 + R_2]^{-1}N_1^\dagger\psi_1. \quad (15)$$

C. Form factors and overlaps from the general perturbation framework

Notice that the wave function for the $E \approx 0$ bands decays exponentially ($\psi_n \approx \frac{1}{n}\psi_{n-1}$) over the momentum space \mathbf{Q} as we go to larger and larger shells. This is due to the inverses in the linear ramp-up term $M_n \propto n$ of Eq. (12) [a consequence of the \mathbf{Q} term in Eq. (7)]. This has immediate implications for the form factors. For example, in Refs. [108–110] we have to compute

$$M_{m,n}^{(\eta)}(\mathbf{k}, \mathbf{q} + \mathbf{G}) = \sum_{\alpha} \sum_{\mathbf{Q} \in \mathcal{Q}_{\pm}} u_{\mathbf{Q}-\mathbf{G},\alpha;m\eta}^*(\mathbf{k} + \mathbf{q})u_{\mathbf{Q},\alpha;n\eta}(\mathbf{k}) \quad (16)$$

for m, n the indices of the active bands, and for different $\mathbf{G} \in \mathcal{Q}_0$. Notice that almost all $|\mathbf{G}| \leq |\mathbf{Q}|$ change the shells (with the exception of $|\mathbf{G}| = 1$): if \mathbf{Q} is in the subshell An/Bn , while \mathbf{G} is of order $|\mathbf{G}| \geq 2|\mathbf{b}_1|$ with \mathbf{b}_1 the moiré reciprocal vector, then $\mathbf{Q} - \mathbf{G}$ is *not* in the subshell An/Bn . Hence, considering $|\mathbf{Q} - \mathbf{G}| > |\mathbf{Q}|$ without loss of generality, we have, for $2|\mathbf{b}_1| \leq |\mathbf{G}| \leq |\mathbf{Q}|$:

$$u_{\mathbf{Q}-\mathbf{G},\alpha;m\eta}^*(\mathbf{k} + \mathbf{q}) \leq \frac{|\mathbf{Q}|!}{|(\mathbf{Q} - \mathbf{G})!}| u_{\mathbf{Q},\alpha;n\eta}^*(\mathbf{k} + \mathbf{q}) \quad (17)$$

for any m, n . Since the wave functions of the active flat bands at (or close to) zero energy exponentially decay with the shell distance from the center we can approximate

$$M_{m,n}^{(\eta)}(\mathbf{k}, \mathbf{q} + \mathbf{G}) \approx \sum_{\alpha} \sum_{\mathbf{Q} \text{ or } \mathbf{Q}-\mathbf{G} \in A_n, B_n, n \leq n_0} u_{\mathbf{Q}-\mathbf{G}, \alpha; m\eta}^*(\mathbf{k} + \mathbf{q}) u_{\mathbf{Q}, \alpha; m\eta}(\mathbf{k}), \quad (18)$$

with n_0 a cutoff. For any \mathbf{k}, \mathbf{q} , the (maximum of any components of the) wave functions on the subshells $A2, B2$ are of order $1/3!, 2!/4!$ times the components of the wave functions on the subshells $A1, B1$. Hence we can restrict to small shell cutoff in the calculation of form factor matrices $n_0 = 1$ (meaning only the subshells $A1, B1$ are taken into account), while paying at most a 15% error. Conservatively, we can keep $n_0 = 2$ and pay a much smaller error $< 3\%$.

Next, we ask for which \mathbf{G} momenta are the function $M_{m,n}^{(\eta)}(\mathbf{k}, \mathbf{q} + \mathbf{G})$ considerably small. Employing Eq. (17), we see that $M_{m,n}^{(\eta)}(\mathbf{k}, \mathbf{q} + \mathbf{G})$ falls off exponentially with increasing \mathbf{G} , and certainly for $|\mathbf{G}| > 2|\tilde{\mathbf{b}}_1|$ they are negligible. The largest contributions are for $\mathbf{G} = 0$ and for $|\mathbf{G}| = |\tilde{\mathbf{b}}_1|$, i.e., for \mathbf{G} being one of the fundamental reciprocal lattice vectors. We hence make the approximation:

$$M_{m,n}^{(\eta)}(\mathbf{k}, \mathbf{q} + \mathbf{G}) \approx \sum_{\alpha} \sum_{\mathbf{Q} \text{ or } \mathbf{Q}-\mathbf{G} \in A1, B1} u_{\mathbf{Q}-\mathbf{G}, \alpha; m\eta}^*(\mathbf{k} + \mathbf{q}) \times u_{\mathbf{Q}, \alpha; m\eta}(\mathbf{k}) (\delta_{\mathbf{G}, 0} + \delta_{|\mathbf{G}|, |\tilde{\mathbf{b}}_1|}). \quad (19)$$

This is one of the most important results of our perturbative scheme. In Refs. [108–111] we employ heavily an approximation called the “flat metric condition” (see [110] for the link between this condition and the quantum metric tensor) to show that some exact eigenstates of the interacting Hamiltonian are in fact, ground states. The flat metric condition requires that

$$\text{Flat metric condition: } M_{m,n}^{(\eta)}(\mathbf{k}, \mathbf{G}) = \xi(\mathbf{G}) \delta_{m,n}. \quad (20)$$

In light of our findings on the matrix elements Eq. (19), we see that the flat metric condition is satisfied for $|\mathbf{G}| \geq 2|\tilde{\mathbf{b}}_1|$, as the matrix element vanishes $M_{m,n}^{(\eta)}(\mathbf{k}, \mathbf{G}) \approx 0 \rightarrow \xi(\mathbf{G}) \approx 0$ for $|\mathbf{G}| \geq 2|\tilde{\mathbf{b}}_1|$. For $\mathbf{G} = 0$, the condition Eq. (20) is always satisfied, even without *any* approximation Eq. (19), as it represents the block wave function orthonormality. Hence, the flat metric condition Eq. (20) is almost always satisfied, with one exception: the only requirement in the flat metric condition is $M_{m,n}^{(\eta)}(\mathbf{k}, \mathbf{G}) = \xi(\mathbf{G}) \delta_{m,n}$ for $|\mathbf{G}| = |\tilde{\mathbf{b}}_1|$. There are six \mathbf{G} vectors that satisfy this condition, namely $\mathbf{G} = \pm\tilde{\mathbf{b}}_1, \pm\tilde{\mathbf{b}}_2, \pm(\tilde{\mathbf{b}}_2 - \tilde{\mathbf{b}}_1)$. The overlaps are all related by symmetry.

In Fig. 5(a) we plot the eigenvalues at $\mathbf{q} = 0$ of the $M^\dagger M$ matrix. We see clearly that these eigenvalues are virtually negligible for $|\mathbf{G}| \geq 2\tilde{\mathbf{b}}_i$, and that for $|\mathbf{G}| = |\tilde{\mathbf{b}}_i|$ they are at most $1/3$ of the value for $|\mathbf{G}| = 0$.

D. Further application of general perturbation framework to TBG

While Eqs. (12) to (14) represent the general perturbation theory of Hamiltonians with a linear (growing) ramping term for almost zero energy bands, we need further simplifications

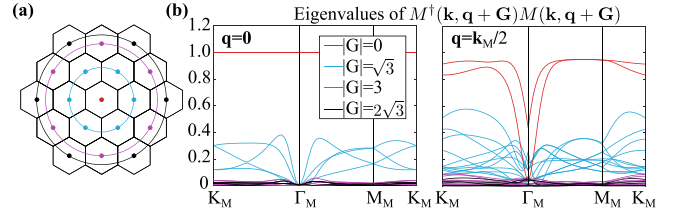


FIG. 5. The magnitude of the form factor (overlap matrix) $M^{(\eta=+)}(\mathbf{k}, \mathbf{q} + \mathbf{G})M(\mathbf{k}, \mathbf{q} + \mathbf{G})$, calculated for $w_0 = 0.4745$ and $w_1 = 0.5931$. (a) The colored dots are the \mathbf{G} vectors we consider in $M^{(\eta=+)}(\mathbf{k}, \mathbf{q} + \mathbf{G})$. Different colors represent different length of \mathbf{G} . (b) The eigenvalues of $M^{(\eta=+)\dagger}(\mathbf{k}, \mathbf{q} + \mathbf{G})M^{(\eta=+)}(\mathbf{k}, \mathbf{q} + \mathbf{G})$ as functions of \mathbf{k} . In the left and right panels we choose $\mathbf{q} = \mathbf{0}$ and $\mathbf{q} = \frac{1}{2}\mathbf{k}_M$, respectively, where \mathbf{k}_M is the M_M momentum in the moiré BZ.

to practically apply them to the TBG problem. However, the form of the $(\mathbf{k} - \mathbf{Q}) \cdot \sigma + H_{A_n, A_n}$, which is not nicely invertible (although it can be inverted), and the form of H_{B_{n-1}, A_n} (see Appendix A for the notation of these matrix elements), which is not diagonal, makes the matrix manipulations difficult, and unfeasible analytically for more than two shells. Hence further approximations are necessary in order to make analytic progress.

First, we want to estimate the order of magnitudes of P_{L-n} and R_{L-n} terms in Eqs. (13) and (14). Recall that our energy is measured in units of $v_F k_\theta$, which for angle of 1° is around 180 meV. We note the following facts:

(1) The diagonal terms $H_{\mathbf{k}A_n}$ are of order $|n - |\mathbf{k}||$, while the $H_{\mathbf{k}B_n}$ are of order $|n + 1 - |\mathbf{k}||$ with \mathbf{k} in the first Brillouin zone ($|\mathbf{k}| < 1$). Therefore, $H_{\mathbf{k}B1} \geq 1, H_{\mathbf{k}A2} > 1$, and all the other $H_{\mathbf{k}A_n}, H_{\mathbf{k}B_n}$ are considerably larger. This shows that M_{n+1} in Eq. (8) is of order n , due to the dominance of the momentum term in relation to the hopping terms.

(2) $H_{A_n B_n}$ and $H_{B_{n-1} A_n}$ are proportional to T_j , so they are of order $\alpha = w_1 / (v_F k_\theta)$. Near the first magic angle ($\theta \approx 1^\circ$, or $w_1 \approx 1/\sqrt{3}$ in units of $v_F k_\theta$), $\alpha \approx 0.6/\theta$ with the angle in degrees (hence *smaller angles have larger* α). By Eq. (8), this means the matrices $N_n \sim H_{B_n A_{n+1}}$ are of order α .

These facts allow us to estimate P_n in Eq. (13):

$$P_n \propto |N_n|^2 |M_{n+1}|^{-2} |P_{n+1}| + 1 \propto (v_F k_\theta)^2 \alpha^2 (v_F k_\theta)^{-2} |P_{n+1}| + 1 = \alpha^2 n^{-2} |P_{n+1}| + 1. \quad (21)$$

For $n \geq 2$ therefore $P_n = 1$ up to a correction term no more than $\alpha^2 n^{-2} < 0.1$. Therefore we are justified (up to a 10% error) of neglecting all $P_n, n \geq 2$ terms. Similarly, using these estimates and substituting into R_n in Eq. (14), we see that

$$|R_n| \leq \frac{\alpha^2}{(n+1)^2} |R_{n+1}| + \frac{(v_F k_\theta) \alpha^2}{(n+1)} \leq 0.04 |R_{n+1}| + 0.09 (v_F k_\theta) \quad (22)$$

when $n \geq 2$ at the first magic angle $\alpha \approx 0.6$. Again this will allow us to neglect the R_n term for $n \geq 2$.

This means that shells after the first one can be neglected at the first magic angle. More generally, only the first N shells will be needed for understanding the N th magic angle.

In order to see the validity of the above approximations more concretely, it is instructive to write down the two-shell

($A1, B1, A2, B2$) Hamiltonian explicitly, and estimate the contribution of the second shell. $A1$ and $B1$ are 12-dimensional Hilbert spaces while $A2$ and $B2$ are 24-dimensional Hilbert

spaces, see Appendix A. Further shells are only a generalization of the ones below. We write the eigenvalue equation:

$$\begin{aligned} (H_{kA1} + H_{A1,A1})\psi_{A1} + H_{A1,B1}\psi_{B1} &= E\psi_{A1}, \\ H_{A1,B1}^\dagger\psi_{A1} + H_{kB1}\psi_{B1} + H_{B1,A2}\psi_{A2} &= E\psi_{B1}, \\ H_{B1,A2}^\dagger\psi_{B1} + (H_{kA2} + H_{A2,A2})\psi_{A2} + H_{A2,B2}\psi_{B2} &= E\psi_{A2}, \\ H_{A2,B2}\psi_{A2} + H_{kB2}\psi_{B2} &= E\psi_{B2}. \end{aligned} \quad (23)$$

We integrate out from the outer shell to the first to obtain the equations

$$\begin{aligned} (H_{kA1} + H_{A1,A1})\psi_{A1} + H_{A1,B1}\psi_{B1} &= E\psi_{A1}, \\ H_{A1,B1}^\dagger\psi_{A1} + \{H_{kB1} + H_{B1,A2}[E - (H_{kA2} + H_{A2,A2}) - H_{A2,B2}(E - H_{kB2})^{-1}H_{A2,B2}^\dagger]^{-1}H_{B1,A2}^\dagger\}\psi_{B1} &= E\psi_{B1}, \end{aligned} \quad (24)$$

and to finally obtain

$$\begin{aligned} E\psi_{A1} &= (H_{kA1} + H_{A1,A1} + H_{A1,B1}\{E - H_{kB1} - H_{B1,A2}[E - (H_{kA2} + H_{A2,A2}) \\ &\quad - H_{A2,B2}(E - H_{kB2})^{-1}H_{A2,B2}^\dagger]^{-1}H_{B1,A2}^\dagger\}^{-1}H_{A1,B1}^\dagger)\psi_{A1}. \end{aligned} \quad (25)$$

Solving the above equation would give us the eigenstate energies, as well as the reduced eigenstate wave functions ψ_{A1} . However, even for two shells above, this is not analytically solvable, hence further approximations are necessary. We implement our approximations here.

(1) First, focusing on the first magic angle of 1° , from numerical calculations we know that the energy of the active bands $|E| < 60$ meV $\approx 0.3v_Fk_\theta$. Hence $EH_{kB1}^{-1} < 0.3$ and furthermore $EH_{kBn}^{-1}, EH_{kAn}^{-1} < 0.3n^{-1}$ for $n \geq 2$. This justifies the approximation around the first magic angle:

$$(E - H_{kB1})^{-1} = -H_{kB1}^{-1} - EH_{kB1}^{-2} \quad (26)$$

and

$$(E - H_{k(A,B)n})^{-1} = -H_{k(A,B)n}^{-1} - EH_{k(A,B)n}^{-2} \quad (27)$$

for $n \geq 2$. *Region of validity of this approximation:* this approximation is independent on w_0, w_1 , the interlayer tunneling. It, however, depends on θ as well as on the energy range of the bands we are trying to approximate. For example, for $\theta = 0.3^\circ$, an energy range $|E| \leq 60$ meV would mean that $|E/v_Fk_\theta| \leq 1$. This gives $|EH_{kBn}^{-1}|, |EH_{kAn}^{-1}| < n^{-1}$ and hence we would only be able to neglect shells larger than $n = 3$. In particular, in order to obtain convergence for bands of energy E at angle θ , we can neglect the shells at distance $n = 2 + [E/v_Fk_\theta]$ (where x means the integer part of x). Hence, as the twist angle is decreased, and if we are interested in obtaining convergent results for bands at a fixed energy, we will need to increase our shell cutoff to obtain a faithful representation of the energy bands. If we keep the number of shells fixed, we will obtain faithful (meaning in good agreement with the infinite cutoff limit) energies only for bands in a smaller energy window as we decrease the twist angle. Notice that this approximation does not depend on w_0, w_1 and hence it is *not* an approximation in the interlayer coupling.

(2) The second approximation is regarding w_0, w_1 : because $\alpha = w_1/v_Fk_\theta \approx 0.6$ at the first magic angle, we can do

a perturbation expansion in the powers of α . We remark that $H_{k,Bn}, H_{k,A_n} \sim n \gg \alpha$ for $n \geq 2$ and $\theta = 1^\circ$. We also remark that $H_{k,B1}^{-1}\alpha \leq 0.6$ for all \mathbf{k} in the first BZ (the largest value, $H_{K_M,B1}^{-1}\alpha = 0.6$ is reached for \mathbf{k} at the K_M corner of the moiré BZ). As such, we find terms of the following form scale as

$$\begin{aligned} H_{AnBn}H_{kA,Bn}^{-1}H_{AnBn}^\dagger &\sim \alpha^2n^{-1} \quad (n \geq 2), \\ H_{Bn-1An}H_{kA,Bn}^{-1}H_{Bn-1An}^\dagger &\sim \alpha^2n^{-1} \quad (n \geq 2), \\ H_{B1A1}H_{kB1}^{-1}H_{B1A1}^\dagger &\sim \alpha^2. \end{aligned} \quad (28)$$

With Eqs. (26)–(28) one can see that in Eq. (25) the leading order contributions of the terms involving the second shell ($A2, B2$) are roughly $\sim |H_{A1,B1}|^2|H_{kB1}|^{-2}|H_{B1,A2}|^2|H_{kA2}|^{-1} \sim \alpha^4/2 \sim 0.05$. It is hence a relatively good approximation to neglect shells higher than $n = 1$ for angle $\theta = 1^\circ$. For example, at the K_M point, neglecting the $n = 2$ shell will induce a less than 10% percent error. *Region of validity of this approximation:* Notice that as the twist angle is decreased, α increases. In general, the relative error of the n th shell is roughly $H_{Bn-1An}H_{kAn}^{-2}H_{Bn-1An}^\dagger \sim \alpha^2/n^2$, so we can neglect the shells for which $n \gg \alpha$ where \gg should be considered twice the value of α . Hence, for an angle of 0.5° ($\alpha = 1.2$) we can neglect all shells greater than 3, etc. For angle $1/n$ of the first magic angle we can neglect all shells above $n + 1$.

All the above remarks, which were made for the Γ_M -centered model, can also be extended to the K_M -centered model in Fig. 4(b). In particular, the tripod model in Fig. 8(b), containing only the $A1, A2$ shells, is a good approximation to the infinite model around the Dirac point, giving the correct first magic angle.

E. Further approximation of the one-shell ($A1, B1$) Hamiltonian in TBG

In the previous section we claimed that, remarkably, a relatively good approximation of the low-energy BM model can be obtained by taking a cutoff of one shell, where we

only consider the *first* A subshell and the first B subshell. The eigenvalue equations are

$$\begin{aligned} (H_{\mathbf{k}A1} + H_{A1,A1})\psi_{A1} + H_{A1,B1}\psi_{B1} &= E\psi_{A1}, \\ H_{A1,B1}^\dagger\psi_{A1} + H_{\mathbf{k}B1}\psi_{B1} &= E\psi_{B1}, \end{aligned} \quad (29)$$

which can be solved for ψ_{B1} to obtain

$$\psi_{B1} = (E - H_{\mathbf{k}B1})^{-1}H_{A1,B1}^\dagger\psi_{A1}. \quad (30)$$

Eliminating ψ_{B1} we find the eigenvalue equation for the first A shell (which includes the coupling to the first B shell):

$$[H_{\mathbf{k}A1} + H_{A1,A1} + H_{A1,B1}(E - H_{\mathbf{k}B1})^{-1}H_{A1,B1}^\dagger]\psi_{A1} = E\psi_{A1}. \quad (31)$$

This is a 12×12 nonlinear eigenvalue equation in E . At this point we will make a few assumptions in order to simplify the eigenvalue equation. In particular, we would like to make this a linear matrix eigenvalue equation. Since we are interested close to $E = 0$ we may assume that $E \ll H_{\mathbf{k}B1}$. This allows us to treat the B shell perturbatively, obtaining

$$(H_{\mathbf{k}A1} + H_{A1,A1} - H_{A1,B1}H_{\mathbf{k}B1}^{-1}H_{A1,B1}^\dagger)\psi_{A1} = E\psi_{A1}. \quad (32)$$

Our approximation Hamiltonian is

$$H_{\text{Approx1}}(\mathbf{k}) = H_{\mathbf{k}A1} + H_{A1,A1} - H_{A1,B1}H_{\mathbf{k}B1}^{-1}H_{A1,B1}^\dagger. \quad (33)$$

We note that $H_{\text{Approx1}}(\mathbf{k})$ is a further perturbative Hamiltonian for the $n = 1$ shell ($A1, B1$). For \mathbf{k} small, around the Γ_M point, we expect this to be an excellent approximation of the $n = 1$ shell Hamiltonian [and since the $n = 1$ shell is a good approximation of the infinite shell, then $H_{\text{Approx1}}(\mathbf{k})$ is expected to be an excellent approximation of the full BM Hamiltonian close to the Γ_M point]. The good approximation is expected to deteriorate as \mathbf{k} gets closer to the boundary of the MBZ, since $H_{A1,B1}H_{\mathbf{k}B1}^{-1}H_{A1,B1}^\dagger$ increases as \mathbf{k} approaches the MBZ boundary. This is because $H_{\mathbf{k}B1}^{-1}$ has larger terms as \mathbf{k} approaches the MBZ boundary. However, we expect still moderate qualitative agreement with the BM Hamiltonian. We also predict that taking two shells ($A1, B1, A2, B2$) would give an extremely good approximation to the infinite shell BM model.

F. Numerical confirmation of our perturbation scheme

The series of approximations performed in Secs. IID and IIE are thoroughly numerically verified at length in Appendix B. We here present only a small part of the highlights. In Fig. 6 we present the $n = 1, 2, 3$ shell (one shell is made out of A, B subshells) results of the BM Hamiltonian in Eq. (3), for two values of w_0, w_1 . We virtually see no change between two and three shells (see also Appendix B), we verify this for higher shells and for many more values of w_0, w_1 , around—and away from, within some manifolds (w_0, w_1) explained in Sec. III—the magic angle. Hence our perturbation framework works well, and confirms the irrelevance of the $n > 2$ shells. The $n = 1$ shell band structure in Fig. 6, while in excellent agreement to the $n = 2$ shells around the Γ_M point, contains some quantitative differences from the $n = 2$ shell (equal to the infinite cutoff) away from the Γ_M point. However, the generic aspects of the band structure, low bandwidth, almost exact degeneracy (at $n = 1$, becoming exact with machine precision in the $n > 2$) at the K_M point are still present even

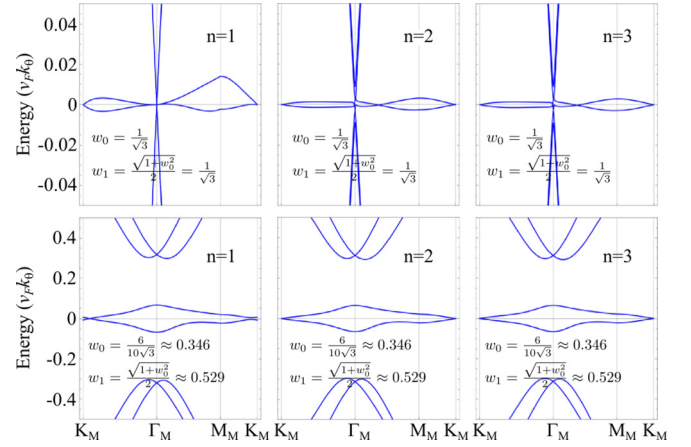


FIG. 6. Comparison of the different cutoff shells of the BM model in Eq. (3), for two values of w_0, w_1 . (more data available in Appendix B). We clearly see that $n = 2$ has reached the infinite cutoff limit (the band structure does not change from $n = 2$ and $n = 3$, while $n = 1$ (only one shell, $A1, B1$ subshells) shows excellent agreement around the Γ_M point, and good agreement even away from the Γ_M point (for example see the second row).

in the $n = 1$ case, as our perturbative framework predicts in Secs. IID and IIE.

Our approximations of the $n = 1$ shell Hamiltonian in Sec. IIE have brought us to the perturbative $H_{\text{Approx1}}(\mathbf{k})$ in Eq. (33). Around the first magic angle we claim that this Hamiltonian is a good approximation to the band structure of the $n = 1$ shell, especially away from MBZ boundary. The $n = 1$ shell is only a 15% difference on the $n = 2$ shell and that the $n = 1$ shell is within 5% of the thermodynamic limit, we then make the approximation that H_{Approx1} explains the band structure of TBG within about 20%. The approximations are visually presented in Fig. 8(a), and the band structure of the approximation H_{Approx1} to the one-shell Hamiltonian is presented in Fig. 7. We see that around the Γ_M point, the Hamiltonian $H_{\text{Approx1}}(\mathbf{k})$ in Eq. (33) has a very good match to the BM Hamiltonian Eq. (3), while away from the Γ_M point the qualitative agreement, small bandwidth, crossing at (close to) K_M (the crossing is at K_M for the infinite shell

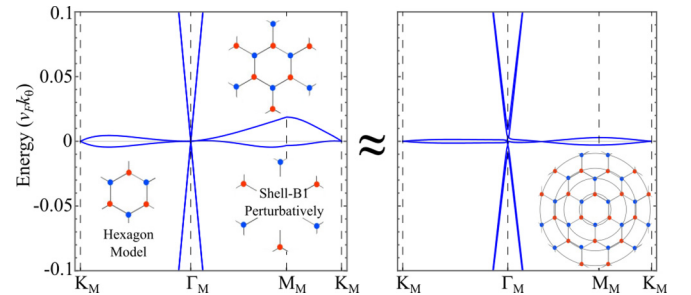


FIG. 7. Band structure of the approximation $H_{\text{Approx1}}(\mathbf{k})$ to the one-shell Hamiltonian, versus the infinite limit approximation, for the $w_0 = w_1 = 1/\sqrt{3}$ magic point. The $n = 1$ shell Hamiltonian band structure is indistinguishable from $H_{\text{Approx1}}(\mathbf{k})$, and is plotted in Appendix B.

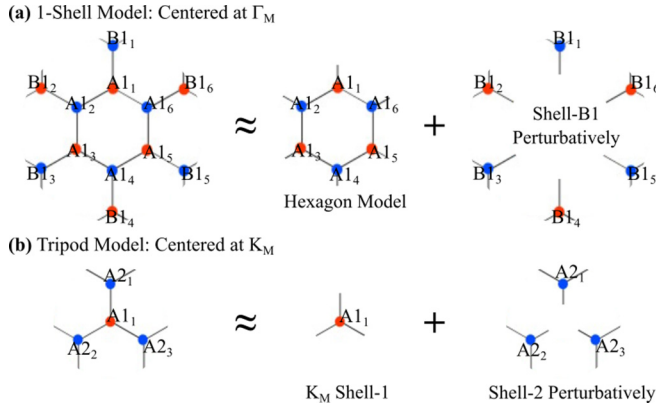


FIG. 8. The two types of approximate models used for analytics. (a) The one-shell ($A1, B1$) model which we have theoretically argued and numerically substantiated to represent a good approximation for values $w_0, w_1 \leq 1/\sqrt{3}$. Analytically we will first solve it by perturbation theory around the hexagon model, which involves only the $A1$ sites. The shell $B1$ will be added perturbatively to obtain $H_{\text{Approx1}}(\mathbf{k})$ in Eq. (33). (A second way to solve for this Hamiltonian will be presented later.) (b) The tripod model, which involves the two shells $A1$ (also known as the K_M point) and $A2$. Due to the same considerations as for the Γ_M -centered model, this should be a good approximation for the infinite shell model for $w_0, w_1 \leq 1/\sqrt{3}$. This is the same model as solved by Bistritzer and MacDonald [1]. We find that the magic angle at which the Dirac velocity vanishes at the K_M point is given by $w_1 = 1/\sqrt{3}, \forall w_0$.

cutoff by symmetry, but can deviate slightly from K_M for finite cutoff).

In Appendix B we present many different tests which confirm all aspects of our perturbative framework, different twist angles and AA, AB coupling. We test the $n = 1, 2, 3, 4, \dots$ shells, and also further test the validity of the approximation $H_{\text{Approx1}}(\mathbf{k})$ to the $n = 1$ shell Hamiltonian in Sec. II E.

III. ANALYTIC CALCULATIONS ON THE BM MODEL: STORY OF TWO LATTICES

We will now analytically study the approximate Hamiltonian in Eq. (33). While in Secs. II D and II E we have focused on the Γ_M -centered lattice, the same approximations can be made in the K_M -centered lattice, where the $H_{\text{Approx1}}(\mathbf{k})$ changes to $H_{\text{Approx1}}(\mathbf{k}) = H_{kA1} + H_{A1,A2} H_{kA2}^{-1} H_{A1,A2}^\dagger$. The two types of approximations are schematically shown in Fig. 8 in the Γ_M - and K_M -centered lattice. First, we start with the tripod model [Fig. 8(b)] to extend the Bistritzer-MacDonald calculation of the magic angle in the isotropic limit and find a “first magic manifold,” where the Dirac velocity vanishes in the tripod model (and is very close to vanishing in the infinite shell BM model). We then solve the 1-shell Γ_M -centered model [Fig. 8(a)], defined by Eq. (33), which is supposed to faithfully describe TBG at and above the magic angle, as proved in Sec. II. This is a 12×12 Hamiltonian, with no known analytic solutions, formed by shell 1: $A1, B1$, where the B part of the first shell $B1$ is taken into account perturbatively, as $H_{A1,B1} H_{kB1}^{-1} H_{A1,B1}^\dagger$.

A. The K_M -centered “tripod model” and the first magic manifold

For completeness we solve for the magic angle in the model in the K_M -centered model of Fig. 4 by taking only four sites, one in shell $A1$ and three in shell $A2$. We call this approximation, depicted in Fig. 8(b), the tripod model. This model is identical to the one solved by Bistritzer and MacDonald in the isotropic limit. However, we will solve for the Dirac velocity away from the isotropic limit, to find a manifold $w_1(w_0)$ where the Dirac velocity vanishes. The tripod Hamiltonian $H_{\text{Tri}}(\mathbf{k}, w_0, w_1)$, with \mathbf{k} measured from the K_M point, reads

$$H_{\text{Tri}}(\mathbf{k}, w_0, w_1) = \begin{pmatrix} \mathbf{k} \cdot \sigma & T_1(w_0, w_1) & T_2(w_0, w_1) & T_3(w_0, w_1) \\ T_1(w_0, w_1) & (\mathbf{k} - \mathbf{q}_1) \cdot \sigma & 0 & 0 \\ T_2(w_0, w_1) & 0 & (\mathbf{k} - \mathbf{q}_2) \cdot \sigma & 0 \\ T_3(w_0, w_1) & 0 & 0 & (\mathbf{k} - \mathbf{q}_3) \cdot \sigma \end{pmatrix}. \quad (34)$$

The Schrödinger equation in the basis $(\psi_{A1}, \psi_{A2}, \psi_{A2}, \psi_{A2})$ reads

$$\mathbf{k} \cdot \sigma \psi_{A1} + \sum_{i=1,2,3} T_i(w_0, w_1) \psi_{A2_i} = E \psi_{A1}, \quad (35)$$

$$T_i \psi_{A1} + (\mathbf{k} - \mathbf{q}_i) \cdot \sigma \psi_{A2_i} = E \psi_{A2_i}, \quad i = 1, 2, 3. \quad (36)$$

From the second equation we find $\psi_{A2_i} = [E - (\mathbf{k} - \mathbf{q}_i) \cdot \sigma_i]^{-1} T_i \psi_{A1}$ and plug it into the first equation to obtain

$$\begin{aligned} E \psi_{A1} &= \mathbf{k} \cdot \sigma \psi_{A1} + \sum_{i=1}^3 T_i \frac{E + (\mathbf{k} - \mathbf{q}_i) \cdot \sigma}{E^2 - (\mathbf{k} - \mathbf{q}_i)^2} T_i \psi_{A2_i} \\ &\approx \mathbf{k} \cdot \sigma \psi_{A1} - \sum_{i=1}^3 T_i [(E + (\mathbf{k} - \mathbf{q}_i) \cdot \sigma] \\ &\quad \times (1 + 2\mathbf{k} \cdot \mathbf{q}_i) T_i \psi_{A2_i}, \end{aligned} \quad (37)$$

where we neglect E^2 as small and expand the denominator to first order in \mathbf{k} to focus on momenta near the K_M Dirac point. Keeping only first order terms in E, \mathbf{k} (not their product as they are both similarly small), and using that $|q_i| = 1, \forall i = 1, 2, 3$, we find

$$(1 - 3w_1^2) \mathbf{k} \cdot \sigma \psi_{A1} = [1 + 3(w_0^2 + w_1^2)] E \psi_{A1} \quad (38)$$

and hence we find that the Dirac velocity vanishes on a manifold of w_0, w_1 given by $w_1 = \frac{1}{\sqrt{3}}$ and $\forall w_0$, which we call the first magic manifold. The angle for which the Dirac velocity vanishes at the K_M point is hence not a magic angle but a magic manifold. However, a further restriction needs to be imposed: w_0 cannot be too large, since from our approximation scheme in Secs. II D and II E, if $w_0 \gg 1/\sqrt{3}$, the tripod model would not be a good approximation for the BM model with a large number of shells; hence we restrict ourselves to $w_0 \leq 1/\sqrt{3}$, and define

$$\text{First magic manifold: } w_0 \leq w_1 = \frac{1}{\sqrt{3}}. \quad (39)$$

The tripod model, Fig. 4(b), in which we found the first magic manifold, does not respect the *exact* C_{2x} symmetry of the lattice, although it becomes asymptotically accurate as the number of shells increases. The magic angle also does not

explain analytically the flatness of bands, since it only considers the velocity vanishing at one point. However, the value obtained by BM for the magic angle is impressive; despite considering only four sites and the K_M point, the bands do not change much after adding more shells, and they are flat throughout the whole Brillouin zone, not only around the K_M point. Why is the entire band so flat at this value? We answer this question by examining the Γ_M -centered model below.

B. The Γ_M -centered hexagon model and the second magic manifold

In Sec. II E we introduced a yet unsolved approximate model $H_{\text{Approx1}}(\mathbf{k})$ in Eq. (33), the Γ_M -centered model in

$$H_{\text{Hex}}(\mathbf{k}, w_0, w_1) = \begin{pmatrix} (\mathbf{k} - \mathbf{q}_1) \cdot \sigma & T_2(w_0, w_1) & 0 & 0 & 0 & T_3(w_0, w_1) \\ T_2(w_0, w_1) & (\mathbf{k} + \mathbf{q}_3) \cdot \sigma & T_1(w_0, w_1) & 0 & 0 & 0 \\ 0 & T_1(w_0, w_1) & (\mathbf{k} - \mathbf{q}_2) \cdot \sigma & T_3(w_0, w_1) & 0 & 0 \\ 0 & 0 & T_3(w_0, w_1) & (\mathbf{k} + \mathbf{q}_1) \cdot \sigma & T_2(w_0, w_1) & 0 \\ 0 & 0 & 0 & T_2(w_0, w_1) & (\mathbf{k} - \mathbf{q}_3) \cdot \sigma & T_1(w_0, w_1) \\ T_3(w_0, w_1) & 0 & 0 & 0 & T_1(w_0, w_1) & (\mathbf{k} + \mathbf{q}_2) \cdot \sigma \end{pmatrix}. \quad (40)$$

This is still a 12×12 Hamiltonian and its eigenstates cannot be analytically obtained at general \mathbf{k} . In particular, it is also not illuminating to focus on a 12×12 Hamiltonian when we want to focus on the physics of the two active bands and the low-energy physics of the dispersive passive bands. As such we make a series of approximations, which also elucidate some of the questions posed in Fig. 1. We first analytically find a set of bands which can act as a perturbation theory treatment.

1. Energies of the hexagon model at $\mathbf{k} = \mathbf{0}$ for arbitrary w_0, w_1

The only momentum where the hexagon model $H_{\text{Hex}}(\mathbf{k}, w_0, w_1)$ can be solved is the Γ_M point. This is fortunate, as this point preserves all the symmetries of TBG, and is a good starting point for a perturbative theory. We find the 12 eigenenergies of $H_{\text{Hex}}(\mathbf{k} = \mathbf{0}, w_0, w_1)$ given in Table I.

By analyzing these energies as a function of w_0, w_1 , we can answer the question (1) in Fig. 1 and give arguments for question (3) in Fig. 1. Numerically, at (and around) the first magic angle—which as per the tripod model is defined as

TABLE I. Eigenvalues of the hexagon model in Eq. (40) at Γ_M point ($\mathbf{k} = \mathbf{0}$). The values for general w_0, w_1 and for $w_0 = w_1 = \frac{1}{\sqrt{3}}$ are given, and Dege. is short for degeneracy.

Band	Energy at $\mathbf{k} = \mathbf{0}$ for any w_0, w_1	$w_0 = w_1 = \frac{1}{\sqrt{3}}$	Dege.
E_1	$2w_1 - \sqrt{1 + w_0^2}$	0	1
E_2	$-2w_1 + \sqrt{1 + w_0^2}$	0	1
$E_{3,4}$	$-\frac{1}{2}(\sqrt{4 + w_0^2} - \sqrt{9w_0^2 + 4w_1^2})$	0	2
$E_{5,6}$	$\frac{1}{2}(\sqrt{4 + w_0^2} - \sqrt{9w_0^2 + 4w_1^2})$	0	2
$E_{7,8}$	$-\frac{1}{2}(\sqrt{4 + w_0^2} + \sqrt{9w_0^2 + 4w_1^2})$	$-\sqrt{13/3}$	2
$E_{9,10}$	$\frac{1}{2}(\sqrt{4 + w_0^2} + \sqrt{9w_0^2 + 4w_1^2})$	$\sqrt{13/3}$	2
E_{11}	$-2w_1 - \sqrt{1 + w_0^2}$	$-4/\sqrt{3}$	1
E_{12}	$2w_1 + \sqrt{1 + w_0^2}$	$4/\sqrt{3}$	1

Fig. 4(a). This model respects all the symmetries of TBG, and we have showed in Appendix B that it represents a good approximation to the infinite cutoff limit. As we can see in Fig. 15, the band dispersions of the $n = 1$ shell model is very similar to that of $n = 2$. After $n = 2$ shells the difference to the infinite cutoff band structure is not visible by eye.

An analytic solution for the 12×12 Hamiltonian $H_{\text{Approx1}}(\mathbf{k})$ in Eq. (33) is *not possible* at every \mathbf{k} . We hence separate the Hamiltonian into $H_{\text{Hex}}(\mathbf{k}, w_0, w_1) = H_{kA1} + H_{A1,A1}$, then treat the smaller part $H_{A1,B1} H_{kB1}^\dagger H_{A1,B1}^\dagger$ perturbatively, for $w_0, w_1 \leq \sqrt{3}$. We will try to solve the first (largest) part of $H_{\text{Approx1}}(\mathbf{k})$: the A1 shell model $H_{\text{Hex}}(\mathbf{k}, w_0, w_1) = H_{kA1} + H_{A1,A1}$ which we call the hexagon model:

$w_1 = 1/\sqrt{3}$ —and in the isotropic limit $w_0 = w_1$, the system exhibits two very flat active bands, not only around the K_M point but everywhere in the MBZ. It also exhibits a very small gap (sometimes nonexistent) between the active bands and the passive bands, around the values $w_0 = w_1 = 1/\sqrt{3}$. The hexagon model $H_{\text{Hex}}(\mathbf{k}, w_0, w_1)$ explains both these observations. We find that the eigenenergies of $H_{\text{Hex}}(\mathbf{k} = \mathbf{0}, w_0 = 1/\sqrt{3}, w_1 = 1/\sqrt{3})$, in the isotropic limit, are given in the third column of Table I. Remarkably, in the isotropic limit $w_0 = w_1$, and at the first magic angle $w_1 = 1/\sqrt{3}$, the bands at the Γ_M point are sixfold degenerate at energy 0. The two active bands are degenerate with the two passive bands above them and the two passive bands below them. This degeneracy is fine tuned, but the degeneracy breaking terms in the next shells (subshells $B1, A2, B2$, etc.) are perturbative. Hence the gap between the active and the passive bands will remain small in the isotropic limit, answering question (1) in Fig. 1.

From the tripod model, the two active bands have energy zero at the K_M point, and vanishing velocity at $w_1 = \frac{1}{\sqrt{3}}$. Moreover, they also have energy zero at the Γ_M point in the hexagon model (a good approximation for the infinite case at the Γ_M point). This now gives us *two* points (Γ_M, K_M) in the MBZ where the bands have zero energy; at one of those points, the band velocity vanishes. This gives us more analytic arguments that the band structure remains flat than just the K_M point velocity, i.e., point (3) in Fig. 1. We further try to establish band properties away from the Γ_M, K_M points by performing a further perturbative treatment of $H_{\text{Hex}}(\mathbf{k}, w_0, w_1)$ using the eigenstates at Γ_M .

2. $\mathbf{k} \neq \mathbf{0}$ six-band approximation of the hexagon model in the isotropic limit

In the isotropic limit at $w_0 = w_1 = 1/\sqrt{3}$, the sixfold degeneracy point of the hexagon model $H_{\text{Hex}}(\mathbf{k}, w_0, w_1)$ at Γ_M

prevents the development of a Hamiltonian for the two active bands. However, since the gap ($=\sqrt{13/3}$) between the six zero modes $E_{1,\dots,6}(\mathbf{k}=0, w_0 = \frac{1}{\sqrt{3}}, w_1 = \frac{1}{\sqrt{3}})$ in Table I and the rest of the bands $E_{7,\dots,12}(\mathbf{k}=0, w_0 = \frac{1}{\sqrt{3}}, w_1 = \frac{1}{\sqrt{3}})$ is large at Γ_M , we can build a six-band $k \cdot p$ Hamiltonian away from the Γ_M point:

$$\begin{aligned} H_{ij}^{6\text{-band}}(\mathbf{k}) &= \langle \psi_{E_i} | H_{\text{Hex}} \left(\mathbf{k}, w_0 = w_1 = \frac{1}{\sqrt{3}} \right) \\ &\quad - H_{\text{Hex}} \left(\mathbf{k} = 0, w_0 = w_1 = \frac{1}{\sqrt{3}} \right) | \psi_{E_j} \rangle \\ &= \langle \psi_{E_i} | I_{6 \times 6} \otimes \mathbf{k} \cdot \vec{\sigma} | \psi_{E_j} \rangle, \end{aligned} \quad (41)$$

where $|\psi_{E_j}\rangle$ with $j = 1, \dots, 6$ are the zero energy eigenstates of $H_{\text{Hex}}(\mathbf{k} = 0, w_0 = w_1 = \frac{1}{\sqrt{3}})$. We find these eigenstates in Appendix C, where we place them in C_3, C_{2x} eigenvalue multiplets. The 6×6 Hamiltonian is the smallest effective Hamiltonian at the isotropic point, due to the sixfold degeneracy of bands at Γ_M .

The explicit form of the Hamiltonian $H^{6\text{-band}}(\mathbf{k})$ is given in Appendix C, Eq. (C7). Due to the large gap between the six bands (degenerate at Γ_M) and the rest of the bands, it should present a good approximation of the hexagon model at finite \mathbf{k} for $w_0 = w_1 = \sqrt{3}$. The approximate $H^{6\text{-band}}(\mathbf{k})$ is still not generically diagonalizable (solvable) analytically. However, we can obtain several important properties analytically. First, the characteristic polynomial

$$\begin{aligned} \text{Det}[E - H^{6\text{-band}}(\mathbf{k})] &= 0 \\ \Rightarrow [13E^2 - 12(k_x^2 + k_y^2)E + k_x(k_x^2 - 3k_y^2)]^2 &= 0. \end{aligned} \quad (42)$$

Or, parametrizing $(k_x, k_y) = k(\cos \theta, \sin \theta)$, where $|\mathbf{k}| = k$, we have

$$[13E^3 - 12k^2E + k^3 \cos(3\theta)]^2 = 0. \quad (43)$$

The characteristic polynomial reveals several properties of the six-band approximation to the hexagon model.

(1) The exponent of 2 in the characteristic polynomial reveals that all bands of this approximation to the hexagon model are exactly doubly degenerate. This explains the almost degeneracy of the flat bands [point (3) in Fig. 1], but furthermore it explains why the passive bands, even though highly dispersive, are almost degenerate for a large momentum range around the Γ_M point in the full model (see Fig. 14): they are exactly degenerate in the six-band approximation to the hexagon model; corrections to this approximation come from the remaining six bands of the hexagon model, which reside extremely far (energy $\sqrt{13/3}$), or from the B_1 shell, which we established is at most 20% in the MBZ—and smaller around the Γ_M point. Thus, the almost double degeneracy of the passive bands pointed out in (2) of Fig. 1 is explained.

(2) Along the Γ_M - K_M line we have $k_x = 0, k_y = k$ and hence the characteristic polynomial becomes

$$\Gamma_M - K_M: (13E^3 - 12k_y^2E)^2 = 0. \quad (44)$$

This implies two further properties: (1) The “active” bands of the approximation of the hexagon mode are exactly flat at $E = 0$ for the whole Γ_M - K_M line, thereby explaining their flatness for a range of momenta; notice that our prior derivations

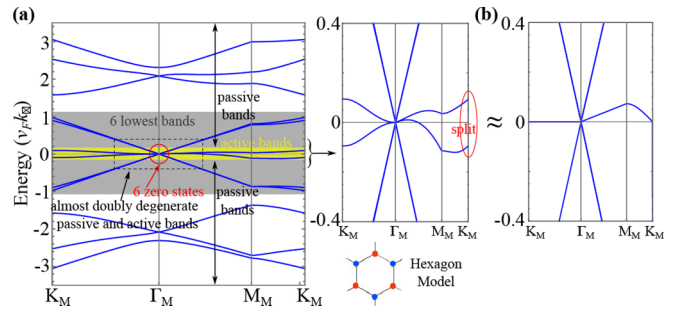


FIG. 9. Band structure of the six-band approximation $H^{6\text{-band}}$ to the hexagon model for the $w_0 = w_1 = 1/\sqrt{3}$ magic point. (a) The six zero energy eigenstates at Γ_M marked by the red circle are used to obtain a perturbative Hamiltonian for the six lowest bands across all the BZ. As the six bands are very well separated from the other six, we expect a good approximation over a large part of the BZ. The active and passive bands in the dashed square are almost doubly degenerate. In the right panel, the six lowest bands of the hexagon model, for a smaller energy range, are shown. Notice the passive bands are undistinguishably twofold degenerate by eye (not an exact degeneracy, they split close to K_M , see left plot) Note the Dirac feature of the passive bands. The active bands split at K_M in the hexagon model, but the B_1 shell addition makes them degenerate. (b) The first order approximation to the hexagon model using the six zero energy bands at the Γ_M point gives exactly doubly degenerate bands over the whole BZ. It gives the correct velocity of the Dirac nodes, zero dispersion of active bands on Γ_M - K_M , and a small dispersion of active bands on Γ_M - M_M , with known velocities. Along these lines, all eigenstates are \mathbf{k} independent.

found that the active bands have zero energy at K_M, Γ_M and vanishing Dirac velocity at K_M for $w_0 = w_1 = \sqrt{3}$; our current derivation shows that the approximately flat bands along the whole Γ_M - K_M line originate from the doubly degenerate zero energy bands of the hexagon model. (2) The dispersive (doubly degenerate) passive bands, for $w_0 = w_1 = \sqrt{3}$, have a linear dispersion

$$E = \pm\sqrt{12/13}k \quad (45)$$

along Γ_M - K_M , with velocity $2\sqrt{3/13} = 0.960769$, close to the Dirac velocity. This explains property (2) in Fig. 1. Note that the velocity is equal to $2/[E_{9,10}(\mathbf{k}=0, w_0 = 1/\sqrt{3}, w_1 = 1/\sqrt{3})]$ or two over the gap to the first excited state. This approximation is visually shown in Fig. 9.

(3) Remarkably, the eigenstates along along the Γ_M - K_M line can also be obtained (see Appendix D). Along this line, the eigenstates of all bands of the $H^{6\text{-band}}$ Hamiltonian approximation to the hexagon model are k_y independent (see Appendix D)!

(4) Along the Γ_M - M_M line ($k_x = k, k_y = 0$) the characteristic polynomial becomes

$$\Gamma_M - M_M: (k + E)^2(k^2 - 13kE + 13E^2)^2 = 0. \quad (46)$$

Hence the energies are $E = -k$, a highly dispersive (doubly degenerate) hole branch passive band of velocity -1 ; $E = \frac{1}{2}(1 + \frac{3}{\sqrt{13}})k$ ($\approx 0.916025k$), another highly dispersive doubly degenerate electron branch passive band. This explains property (2) in Fig. 1. Notice that this velocity is $\frac{1}{2}(1 + \frac{1}{E_{9,10}(\mathbf{k}=0, w_0=1/\sqrt{3}, w_1=1/\sqrt{3})})$. The third dispersion is

TABLE II. Eigenvalues of the hexagon model in Eq. (40) at Γ_M point ($\mathbf{k} = \mathbf{0}$) at the second magic manifold $w_1 = \frac{\sqrt{1+w_0^2}}{2}$. The notation Dege. is short for degeneracy.

Band	Energy at $\mathbf{k} = \mathbf{0}$ at $w_1 = \frac{\sqrt{1+w_0^2}}{2}$	Dege.
$E_{1,2}$	0	2
$E_{3,4}$	$\frac{\sqrt{10w_0^2+1}-\sqrt{w_0^2+4}}{2}$	2
$E_{5,6}$	$-\frac{\sqrt{10w_0^2+1}-\sqrt{w_0^2+4}}{2}$	2
$E_{7,8}$	$-\frac{\sqrt{10w_0^2+1}+\sqrt{w_0^2+4}}{2}$	2
$E_{9,10}$	$\frac{\sqrt{10w_0^2+1}+\sqrt{w_0^2+4}}{2}$	2
E_{11}	$-2\sqrt{1+w_0^2}$	1
E_{12}	$2\sqrt{1+w_0^2}$	1

$E = \frac{1}{2}(1 - \frac{3}{\sqrt{13}})k$ ($\approx 0.0839749k$), a weakly dispersive doubly degenerate active band. This explains the very weak, but nonzero dispersion of the bands on Γ_M - M_M . The eigenstates along this line can also be obtained (see Appendix D). The approximation is visually shown in Fig. 9.

(5) Along the Γ_M - M_M , the eigenstates of all bands of the $H^{6\text{-band}}$ Hamiltonian approximation to the hexagon model are k_x independent (see Appendix D)!

(6) In the six-band model, eigenstates are independent of \mathbf{k} on the manifold $k_x = k_y$.

3. Energies of the hexagon model at $\mathbf{k} = \mathbf{0}$ away from the isotropic limit and the second magic manifold

In the isotropic limit (which coincides with the magic angle of the tripod model), $w_0 = w_1 = 1/\sqrt{3}$, due to the sixfold degeneracy of the Γ_M point, it is impossible to obtain an approximate Hamiltonian that is less than a 6×6 matrix. Moving away from the isotropic limit, and staying in the range of approximations $w_0, w_1 \leq \frac{1}{\sqrt{3}}$, the hexagon model is a good starting point for a perturbative expansion. We now ask what values of w_1, w_0 might have a “simple” expression for their energies.

We see that if $w_1 = \frac{\sqrt{1+w_0^2}}{2}$, the sixfold degeneracy at the Γ_M point at zero energy for $w_1 = 1/\sqrt{3}$ splits into a 2(enforced) + 2(accidental) + 2(enforced)-fold degeneracy. There is an *accidental* twofold degeneracy of the active bands at zero energy, and a gap to the passive bands which have an *symmetry enforced* degeneracy. The twofold accidental degeneracy at zero energy along $w_1 = \frac{\sqrt{1+w_0^2}}{2}$ is the important property of this manifold in parameter space. The eigenvalues of the hexagon model in this case are given in Table II.

Although the perturbative addition of the $B1$ shell will split the Γ_M point $E_{1,2}(\mathbf{k} = \mathbf{0}, w_0, w_1 = \frac{\sqrt{1+w_0^2}}{2}) = 0$ degeneracy, we find that this zero energy doublet of the hexagon model is particularly useful to calculate a $k \cdot p$ perturbation theory of the active bands, as many perturbative terms cancel. In particular, we see that the gap between the active band zero energy doublet and the passive bands $[E_{3,4}(\mathbf{k} =$

$\mathbf{0}, w_0, w_1 = \frac{\sqrt{1+w_0^2}}{2})]$ of the hexagon model becomes large in the chiral limit $[E_{3,4}(\mathbf{k} = \mathbf{0}, w_0 = 0, w_1 = \frac{\sqrt{1+w_0^2}}{2} = 1/2) = -1/2]$. We note that this explains property (4) of Fig. 1: from the hexagon model, the gap between the active and the passive bands is, in effect, proportional to $w_1 - w_0$. Since the bandwidth of the TBG model is known to be smaller than this gap, we will use the Γ_M point doublet of states $E_{1,2}(\mathbf{k} = \mathbf{0}, w_0, w_1 = \frac{\sqrt{1+w_0^2}}{2}) = 0$ to perform a perturbative expansion. We define this parameter manifold as the “second magic manifold”:

$$\text{Second magic manifold: } w_1 = \frac{\sqrt{1+w_0^2}}{2}, \quad w_0 \leq 1/\sqrt{3}.$$

IV. TWO-BAND APPROXIMATIONS ON THE MAGIC MANIFOLDS

A. Differences between the first and second magic manifolds

We have defined two manifolds in parameter space where the two active bands of the hexagon model are separated from the passive bands. Hence, we can do a perturbative expansion in the inverse of the gap from the passive to the active bands. We first briefly review the differences between the two magic manifolds

First magic manifold: $w_0 \leq w_1 = 1/\sqrt{3}$.

(1) For these values of w_0, w_1 , the Dirac velocity at K_M vanishes in the tripod model, which is a good approximation to the infinite cutoff model. Hence the velocity at the K_M point in the infinite model should be small. The Dirac node is at $E = 0$.

(2) One end of the first magic manifold, the isotropic point $w_0 = w_1 = 1/\sqrt{3}$ is also the endpoint of the second magic manifold, and exhibits the sixfold degeneracy at $E = 0$ at the Γ_M point in the hexagon model.

(3) Away from the isotropic point, on the first magic manifold, a gap opens everywhere between the six states of the hexagon model. At the Γ_M point, the sixfold degenerate bands at the isotropic limit split when going away from this limit, into a 2 (symmetry enforced) -1-1-2 (symmetry enforced) degeneracy configuration. Hence the two active bands, in the hexagon model, split from each other in the first magic manifold.

(4) The splitting of the active bands in the hexagon model in the first magic manifold is corrected by the addition of the $B1$ shell as the term $H_{A1,B1}H_{KB1}^{-1}H_{A1,B1}^\dagger$ in Eq. (33).

(5) The active bands, when computed with the full Hamiltonian without approximation, are very flat on the first magic manifold (much flatter than on the second magic manifold), and there is a full, large gap to the passive bands (see Fig. 10).

Second magic manifold: $w_1 = \frac{\sqrt{1+w_0^2}}{2}, w_0 \leq 1/\sqrt{3}$.

(1) The hexagon model exhibits a doublet of zero energy active bands at Γ_M along the entire second magic manifold.

(2) One end of the second magic manifold, the isotropic point $w_1 = w_0 = 1/\sqrt{3}$ is also the endpoint of the first magic manifold, and exhibits a sixfold degeneracy at $E = 0$ at the Γ_M point in the hexagon model and a vanishing Dirac velocity in the tripod model.

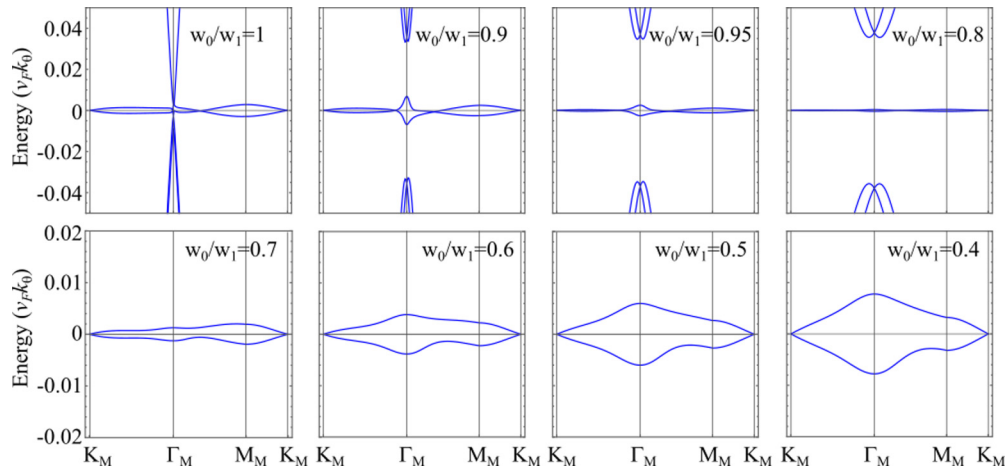


FIG. 10. Plots of the active bands band structure on the first magic manifold, $w_1 = 1/\sqrt{3}$, $w_0 \leq \sqrt{3}$, for a large number of shells. In the second row, the gap to the passive bands is large and outside the range. The Dirac velocity is small for all values of w_0/w_1 (it vanishes in the tripod model, but has a finite value once further shells are included), and the bands are extremely flat. The ratio of active bands bandwidth to the active-passive band gap decreases upon decreasing w_0/w_1 .

(3) Away from the isotropic point, on this manifold, the bands do not have a vanishing velocity at the Dirac point.

(4) The eigenstates of the active bands are simple (simpler than on the first magic manifold) on this manifold, with simple matrix elements (as proved below). A perturbation theory can be performed away from the Γ_M point and away from this manifold to obtain a general Hamiltonian for \mathbf{k} , w_0 , w_1 . The $B1$ shell can then also be included perturbatively as the term $H_{A1,B1} H_{kB1}^{-1} H_{A1,B1}^\dagger$ in Eq. (33).

(5) The active bands are not the flattest on this manifold. They are much less flat than on the first magic manifold, due to the fact that the Dirac velocity does not vanish (is not small) at the K_M point on the second magic manifold.

B. Two-band approximation for the active bands of the hexagon model on the second magic manifold

We now try to obtain a two-band model on the manifold $w_1 = \sqrt{1 + w_0^2}/2$, $\forall w_0 \leq 1/\sqrt{3}$, for which we use the Γ_M -point $H_{\text{Hex}}(\mathbf{k} = 0, w_0, w_1 = \frac{\sqrt{1+w_0^2}}{2})$ as a zeroth order Hamiltonian and perform a $\mathbf{k} \cdot \mathbf{p}$ expansion away from the Γ_M point.

Figure 10 shows that away from the isotropic limit, the gap that opens at the Γ_M point between the formerly sixfold degenerate bands can be much larger than the bandwidth of the active bands even for modest deviations from the isotropic limit. We have explained this from the behavior of the six-band approximation to the hexagon model, and from knowing the analytic form of the Γ_M -point energy levels in the hexagon model. We have also obtained the eigenstates of all the Γ_M -energy levels in Appendix E 2. It is then sufficiently accurate to treat the manifold of the *two* Γ_M -point zero energy states at $w_1 = \frac{\sqrt{1+w_0^2}}{2}$, $\forall w_0 \leq 1/\sqrt{3}$ as the bases of the perturbation theory.

To perform a two-band model approximation to the hexagon model, we take the unperturbed Hamiltonian to be $H_{\text{Hex}}(\mathbf{k} = 0, w_0, w_1 = \sqrt{1 + w_0^2}/2)$ (the hexagon model on

the second magic manifold) in Eq. (40). For this Hamiltonian we are able to obtain *all the eigenstates analytically* in Appendix E 2. The perturbation Hamiltonian, on the second magic manifold, is

$$\begin{aligned} H_{\text{perturb}}(\mathbf{k}, w_0) &= H_{\text{Hex}}\left(\mathbf{k}, w_0, w_1 = \frac{\sqrt{1 + w_0^2}}{2}\right) \\ &\quad - H_{\text{Hex}}\left(\mathbf{k} = 0, w_0, w_1 = \frac{\sqrt{1 + w_0^2}}{2}\right) \\ &= I_{6 \times 6} \otimes \mathbf{k} \cdot \vec{\sigma}. \end{aligned} \quad (47)$$

The manifold of states which are kept as “important” are the two zero energy eigenstates of $H_{\text{Hex}}(\mathbf{k} = 0, w_0, w_1 = \sqrt{1 + w_0^2}/2)$, given in Eq. (E7). This manifold will be denoted as ψ with a band index $m \in \{1, 2\}$. The manifold of “excited” states, which will be integrated out, is made up of the eigenstates Eqs. (E8), (E9), (E10), and (E11), each doubly degenerate, and Eqs. (E12) and (E13), each nondegenerate. This manifold will be denoted as ψ with a band index $l \in \{3, 4, \dots, 12\}$. We now give the expressions for the perturbation theory up to fifth order. We here give only the final results, for the expression of the matrix elements computed in perturbation theory, see Appendix F 2.

We first note that the first order (linear in \mathbf{k}) perturbation term is $H_{mm'}^{(1)}(\mathbf{k}, w_0) = \langle \psi_m | H_{\text{perturb}}(\mathbf{k}, w_0) | \psi_{m'} \rangle = 0$. This is a particular feature of the second magic manifold and renders the perturbation theory simple. Furthermore, it implies that, on the second magic manifold, the active bands of the hexagon model have a quadratic touching at the Γ_M point, as confirmed numerically. Due to the vanishing of these matrix elements, one can perform quite a large order perturbative expansion.

It can be shown that the n th order perturbation is proportional to $1/(3w_0^2 - 1)^{n-1}$, with symmetry-preserving functions of \mathbf{k} (see Appendix F 2). Up to the fifth order, the full two-band approximation to the hexagon Hamiltonian can

be expressed as

$$H_{2\text{-band}}^{\text{Hex}}\left(\mathbf{k}, w_0, w_1 = \frac{\sqrt{1+w_0^2}}{2}\right) = d_0(\mathbf{k}, w_0)\sigma_0 + d_1(\mathbf{k}, w_0)(\sigma_y + \sqrt{3}\sigma_x),$$

where

$$d_0(\mathbf{k}, w_0) = \frac{4w_0}{9\sqrt{w_0^2+1}(1-3w_0^2)^2} \left[(w_0^2-3) - \frac{4(29w_0^6-223w_0^4-357w_0^2-9)}{9(1-3w_0^2)^2(w_0^2+1)} (k_x^2+k_y^2) \right] \times k_x(k_x^2-3k_y^2) \quad (48)$$

and

$$d_1(\mathbf{k}, w_0) = \frac{4w_0^2}{3\sqrt{w_0^2+1}(3w_0^2-1)} \times \left[-1 + \frac{2(35w_0^4+68w_0^2+9)(k_x^2+k_y^2)}{9(w_0^2+1)(3w_0^2-1)^2} \right] \times (k_x^2+k_y^2), \quad (49)$$

while the Pauli matrices σ_j here are in the basis defined in Appendix E 2 a (rather than the basis of graphene sublattice). In particular, we note that the eigenstates of the $k \cdot p$ model $H_{2\text{-band}}^{\text{Hex}}(\mathbf{k}, w_0, w_1 = \frac{\sqrt{1+w_0^2}}{2})$ are independent of \mathbf{k} up to the fifth order perturbation within the hexagon model.

C. Away from the second magic manifold: Two-band active bands approximation of the hexagon model

We now want to perform calculations away from the second magic manifold, and possibly connect the perturbation theory with the first magic manifold. There are two ways of doing this, while still using the Γ_M -point wave functions as a basis (we cannot solve the hexagon model exactly at any other \mathbf{k} point). One way is to solve for the wave functions at the Γ_M point for all w_0, w_1 , and use these states to build a perturbation theory that way. However, away from the special first and second magic manifolds, the expression of the ground states is complicated. The second way is to use the eigenstates already obtained for the second magic manifold $w_1 = \frac{\sqrt{1+w_0^2}}{2}$ and obtain a perturbation away from the second magic manifold. In this section we choose the latter.

We take the unperturbed Hamiltonian to be $H_{\text{Hex}}(\mathbf{k} = 0, w_0, w_1 = \sqrt{1+w_0^2}/2)$ (the hexagon model on the second magic manifold) in Eq. (40). For this Hamiltonian we are able to obtain *all the eigenstates analytically* in Appendix E 2. The perturbation Hamiltonian, away the second magic

manifold, is

$$H_{\text{perturb}}(\mathbf{k}, w_0, w_1) = H_{\text{Hex}}(\mathbf{k}, w_0, w_1) - H_{\text{Hex}}\left(\mathbf{k} = 0, w_0, w_1 = \frac{\sqrt{1+w_0^2}}{2}\right) = I_{6 \times 6} \otimes \mathbf{k} \cdot \vec{\sigma} + H_{\text{Hex}}\left(\mathbf{k} = 0, 0, w_1 = \frac{\sqrt{1+w_0^2}}{2}\right). \quad (50)$$

We now give the expressions for the perturbation theory up to fourth order. We here give only the final results, for the expression of the matrix elements computed in perturbation theory, see Appendices F 2 and F 3.

We first note that the first order Hamiltonian is

$$H_{mm'}^{(1)}(\mathbf{k}, w_0, w_1) = \left(\frac{\sqrt{w_0^2+1}}{2} - w_1 \right) (\sigma_y + \sqrt{3}\sigma_x). \quad (51)$$

Hence we find there is now a linear order term in the Hamiltonian—as it should since the two states degenerate at Γ_M on the second magic manifold are no longer degenerate away from it. Because of this, many other terms in the further degree perturbation theory become nonzero, and the perturbation theory has a more complicated form. We present all details in Appendix F 3 and here show only the final result, up to fourth order. We can label the two-band Hamiltonian as

$$H_{2\text{-band}}^{\text{Hex}}(\mathbf{k}, w_0, w_1) = d_0(\mathbf{k}, w_0, w_1)\sigma_0 + d_1(\mathbf{k}, w_0, w_1)(\sigma_y + \sqrt{3}\sigma_x), \quad (52)$$

where the expressions of $d_0(\mathbf{k}, w_0, w_1)$ and $d_1(\mathbf{k}, w_0, w_1)$ are given in Eqs. (F35) and (F36) in Appendix F 3. The perturbation is made on the zero energy eigenstates of $H_{\text{Hex}}(\mathbf{k} = 0, w_0, w_1 = \frac{\sqrt{1+w_0^2}}{2})$. If $w_1 = \frac{\sqrt{1+w_0^2}}{2}$, then the expressions reduce to our previous Hamiltonian Eq. (F20). Notice that so far, remarkably the eigenstates are not \mathbf{k} dependent, they are just the eigenstates of $(\sigma_y + \sqrt{3}\sigma_x)$.

D. Two active bands approximation of the $n = 1$ shell model $H_{\text{Approx1}}(\mathbf{k})$ on the second magic manifold

In Sec. IV B we have obtained an effective model for the two active bands of the hexagon model on the second magic manifold $w_1 = \frac{\sqrt{1+w_0^2}}{2}$, $\forall w_0 \leq 1/\sqrt{3}$ using the Γ_M -point $H_{\text{Hex}}(\mathbf{k} = 0, w_0, w_1 = \frac{\sqrt{1+w_0^2}}{2})$ as zeroth order Hamiltonian. We expect this to be valid around the Γ_M point. We know that a good approximation of the TBG involves at least $n = 1$ shells: the A1 subshell, which is the hexagon model, and the B1 subshell, which is taken into account perturbatively in $H_{\text{Approx1}}(\mathbf{k})$ of Eq. (33). After detailed calculations given in Appendix F 4, we find the first order perturbation Hamiltonian given by

$$H^{(B1)}(\mathbf{k}, w_0, w_1) = \frac{1}{\prod_{i=1,2,3} |k - 2q_i|^2 |k + 2q_i|^2} \times \sum_{\mu=0,x,y,z} \tilde{d}_\mu(\mathbf{k}, w_0, w_1)\sigma_\mu, \quad (53)$$

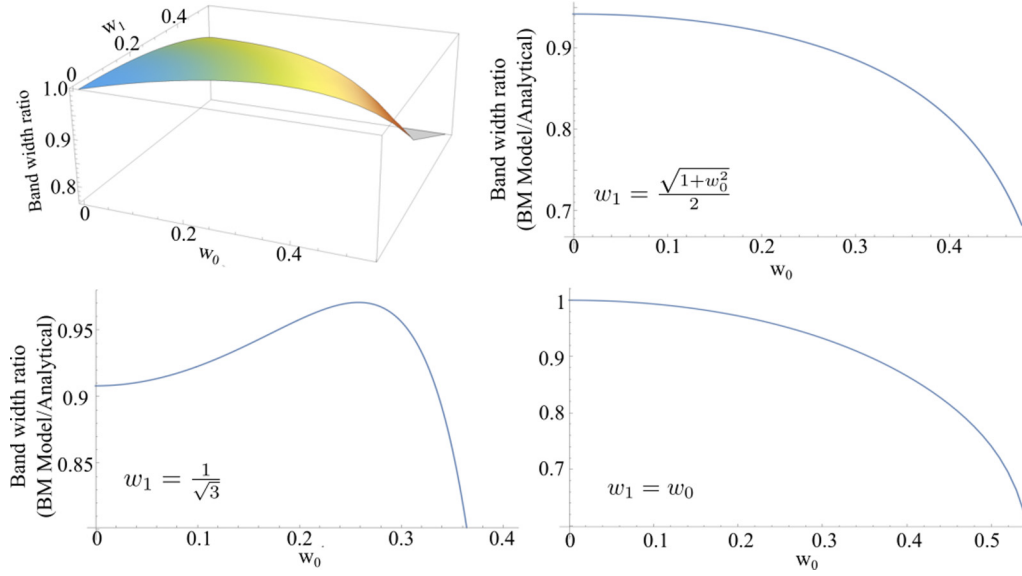


FIG. 11. Plots of the ratio of the bandwidth of the active bands for the large number of shells to the analytic bandwidth Δ in Eq. (56), for different values of w_0, w_1 , including the two magic manifolds. In the regime of validity of our approximations, we can see that this ratio is substantially above 90%.

where $\tilde{d}_\mu(\mathbf{k}, w_0, w_1)$ are given in Eqs. (F39)–(F42) of Appendix F 4. This represents the first order $H_{\text{Approx1}}(\mathbf{k})$ projected into the zero energy bands of the hexagon model on the second magic manifold. We note that the $B1$ shell perturbation expressions can only be obtained to first order. Second and higher orders are particularly tedious and not illuminating. Note that, to first order in perturbation theory on the second magic manifold, only the term $H_{A1,B1}H_{kB1}^{-1}H_{A1,B1}^\dagger$ contributes to the approximate two-band Hamiltonian. Also, we obtained the perturbation of $H_{A1,B1}H_{kB1}^{-1}H_{A1,B1}^\dagger$ for *generic* w_0, w_1 projected into the second magic manifold Γ_M point bands of the hexagon model.

E. Two-band approximation for the active bands of the $n = 1$ shell model $H_{\text{Approx1}}(\mathbf{k})$ in Eq. (33) for any $w_0, w_1 \leq \frac{1}{\sqrt{3}}$

We are now in a position to describe the two active bands of the approximate Hamiltonian of the one-shell model in Eq. (33), $H_{\text{Approx1}} = H_{kA1} + H_{A1,A1} - H_{A1,B1}H_{kB1}^{-1}H_{A1,B1}^\dagger$ by adding $H^{(B1)}(\mathbf{k}, w_0, w_1)$ of Eq. (54) to $H_{2\text{band}}^{\text{Hex}}(\mathbf{k}, w_0, w_1)$ of Eq. (53). We note that this is still perturbation theory performed by using the Γ_M -point $H_{\text{Hex}}(\mathbf{k} = 0, w_0, w_1 = \frac{\sqrt{1+w_0^2}}{2})$ as a zeroth order Hamiltonian:

$$H_{2\text{-band}}(\mathbf{k}, w_0, w_1) = H_{2\text{-band}}^{\text{Hex}}(\mathbf{k}, w_0, w_1) + H^{(B1)}(\mathbf{k}, w_0, w_1). \quad (54)$$

We now find some of the predictions of this Hamiltonian.

The energies of the two bands of Eq. (55) at Γ_M point are

$$E_\pm(w_0, w_1) = \pm \left(\frac{-4\sqrt{w_0^2 + 1}w_1 + w_0^2 + w_1^2 + 2}{2\sqrt{w_0^2 + 1}} \right) \quad (55)$$

over the full range of $w_0, w_1 \leq 1/\sqrt{3}$. Remarkably we find an amazing agreement between the energy of the bands at Γ_M point and the numerics. We find that the bandwidth of the flat

band at Γ_M point is

$$\Delta(w_0, w_1) = 2|E_\pm(w_0, w_1)|. \quad (56)$$

This matches incredibly well with the actual values. In Fig. 11 we plot the ratio of actual active bandwidth at Γ_M point from the large number of shell model to Δ in Eq. (56), for values $w_0 < 1/\sqrt{3}, w_0 < w_1 < 1/\sqrt{3}$. Note that even though we are sometimes going far from the second magic manifold values $w_0, w_1 = \sqrt{1 + w_0^2}/2$ where the perturbation theory is valid, the ratio holds up well, and is actually never smaller than 0.8 or larger than 1. We are using $w_0 < w_1$ because the perturbation theory is around the manifold $w_0, w_1 = \sqrt{1 + w_0^2}/2 \leq \frac{1}{\sqrt{3}}$ for which $w_0 < w_1$. For $w_1 < w_0$ the approximation becomes worse, but is outside of the validity regime.

For the two magic manifolds, also shown in Figs. 11 and 12, the agreement is very good. We point out several consistency checks. First, remarkably, the set of approximations that led us to finding a two-band Hamiltonian becomes *exact* at some points.

(1) The Γ_M point bandwidth at $w_0 = w_1 = 1/\sqrt{3}$ vanishes $\Delta(\frac{1}{\sqrt{3}}, \frac{1}{\sqrt{3}}) = 0$. This degeneracy reproduces the exact result, in the one-shell model (see $n = 1$ in Fig. 13, the sixfold degeneracy at the Γ_M point). The approximate model of the one-shell H_{Approx1} of Eq. (33) also has an exact sixfold degeneracy at the Γ_M point at $w_0 = w_1 = 1/\sqrt{3}$ (the two bands here being part of the sixfold manifold). It is remarkable that our two-band projection perturbation approximation reproduces this degeneracy exactly, especially since it is supposed *not* to work close to $w_0 = w_1 = 1/\sqrt{3}$ —where the gap to the active bands is 0 and the Γ_M point becomes sixfold degenerate.

(2) At $w_0 = w_1 = 0$, the bandwidth at Γ_M is $\Delta(0, 0) = 2$. This is again an exact result for the *infinite shell model*. Indeed, at the Γ_M point, the BM Hamiltonian with zero interlayer coupling has a gap $= 2|q_1| = 2$.

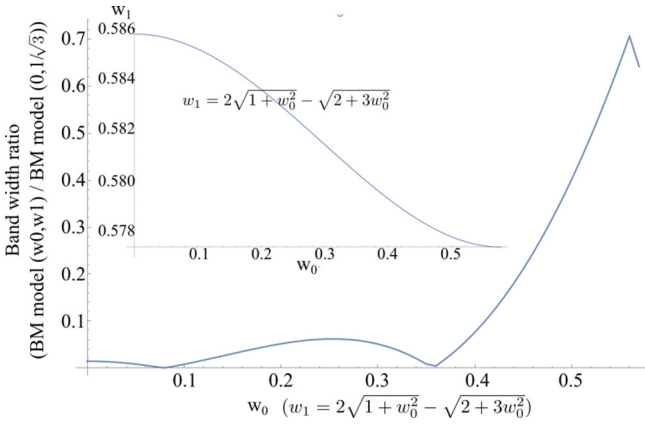


FIG. 12. Γ_M point bandwidth of the active bands (large number of shells) on the manifold $\Delta(w_0, w_1) = 0$ ($w_1 = 2\sqrt{1+w_0^2} - \sqrt{2+3w_0^2}$) of zero analytic bandwidth [Eq. (56)] divided by the bandwidth of the active bands in the chiral limit [$(w_0, w_1) = (0, \frac{1}{\sqrt{3}})$]. Note that this number is extremely small away from $w_0 = w_1 = \frac{1}{\sqrt{3}}$, showing that our analytic manifold of smallest bandwidth [$\Delta(w_0, w_1) = 0$] also exhibits small bandwidth in the large cell number. Inset: The curve $w_1 = 2\sqrt{1+w_0^2} - \sqrt{2+3w_0^2}$ for which $\Delta(w_0, w_1) = 0$ for $0 \leq w_0 \leq \frac{1}{\sqrt{3}}$. Note that w_1 changes extremely little 1% (stays within 1% of $\frac{1}{\sqrt{3}}$) during the entire sweeping of w_0 .

(3) We now ask: what is the w_0, w_1 manifold, under this approximation, for which the Γ_M point bandwidth is zero? This is easily solved to give:

Two-band model with zero bandwidth at Γ_M :

$$w_1 = 2\sqrt{w_0^2 + 1} - \sqrt{3w_0^2 + 2}, \quad w_0 \in \left[0, \frac{1}{\sqrt{3}}\right]. \quad (57)$$

Figure 12 plots the ratio of the bandwidth of the full BM model on this manifold to the bandwidth at the chiral limit $w_0 = 0, w_1 = \frac{1}{\sqrt{3}}$ (which is already really small!). We can see that, for most of the $w_0 \in (0, 1/\sqrt{3})$, this ratio is below 0.1, showing us that we have identified an extremely small bandwidth manifold.

(4) What are the values of w_1 on this manifold? Remarkably, as can be seen in Fig. 12, $w_1 = 2\sqrt{w_0^2 + 1} - \sqrt{3w_0^2 + 2}$ is an almost fully constant over the interval $w_0 \in (0, 1/\sqrt{3})$: it changes by around 1% only. Moreover, its values (0.578–0.586) are very close to $1/\sqrt{3} \approx 0.57735$. Hence our approximation explains the flatness of the bands over the *first magic manifold*, $0 \leq w_0 \leq \frac{1}{\sqrt{3}}, w_1 = \frac{1}{\sqrt{3}}$: This manifold is almost the same as the one for which our analytical approximate calculation gives zero gap. Hence property (6) of Fig. 1 is answered.

(5) At $w_0 = 0$, one has $w_1 = 2\sqrt{w_0^2 + 1} - \sqrt{3w_0^2 + 2} = 2 - \sqrt{2}$ in Eq. (57), for which the bandwidth is 0 in our perturbative model. As we show in Appendix F 5, this value of w_1 coincides with the exact value for which the Γ_M bandwidth is zero in the approximation Hamiltonian H_{Approx1} of Eq. (33). Furthermore, at $w_0 = 0$, the value $w_1 = 2 - \sqrt{2}$ also coincides with the exact value of zero Γ_M bandwidth in the

no-approximation Hamiltonian of the $n = 1$ shell Hamiltonian (of $A1, B1$ subshells) (see Appendix F 5).

(6) At $w_0 = 0$, the value $w_1 = 2\sqrt{w_0^2 + 1} - \sqrt{3w_0^2 + 2} = 2 - \sqrt{2}$ for which the bandwidth of our approximate two-band model is projected to be zero is numerically *very* close to the value of 0.586 quoted for the first magic angle in the chiral limit [37]. In fact, at $w_0 = 0, w_1 = 2 - \sqrt{2}$ the bandwidth of the active bands is half of that at $w_1 = 0.586$.

F. Region of validity of the two-band model and further fine tuning

The two-band approximation to the $n = 1$ shell model has a radius of convergence in \mathbf{k} space in the first MBZ. This radius of convergence is easily estimated from the following argument. In Table II, the (maximum) gap, at the Γ_M point, between the active and the passive bands in the hexagon model (and in the region $w_0 \leq 1/\sqrt{3}$) is at $w_0 = 0$ and equals 1/2. The distance, in the MBZ between Γ_M and K_M points, equals 1. Hence we expect that our two-band model will work for $|\mathbf{k}| \ll 1/2$, as our numerical results confirm. The form factor matrices can be computed for this range of \mathbf{k} analytically, by using the full hexagon Hamiltonian in Eq. (52) plus the $B1$ shell perturbation in Eq. (53). They will be presented in a future publication.

The $\mathbf{k} = K_M$ point is outside the range of validity of the two-band model, and hence this does not capture the gapless Dirac point for all values of w_0, w_1 . However, with some physical intuition, we can obtain a two-band model that has a gap closing at the K_M point. In Fig. 9 we see that the hexagon model does not have a gap closing between the active bands at the K_M point. However, in Figs. 18, 19, and 20 we see that $H_{\text{Approx1}}(\mathbf{k})$ in Eq. (33) has a gap closing close to, or almost at the K_M point. This means that one of the main roles of the $B1$ shell is to close the K_M gap, leading to the Dirac point.

Hence we can use the two-band model of the first order approximation to the hexagon model, Eq. (51), $H_{mn}^{(1)}(\mathbf{k}, w_0, w_1) = (\frac{\sqrt{w_0^2+1}}{2} - w_1)(\sigma_y + \sqrt{3}\sigma_x)$ along with the two-band model first order approximation for the $B1$ -shell $H^{(B1)}(\mathbf{k}, w_0, w_1)$ to obtain a first order two-band approximation Hamiltonian: $H^{(1)}(\mathbf{k}, w_0, w_1) + H^{(B1)}(\mathbf{k}, w_0, w_1)$. Note that $H^{(1)}(\mathbf{k}, w_0, w_1)$, the two-band first order approximation to the hexagon model, has two flat \mathbf{k} independent bands. We now impose the condition: $H^{(1)}(\mathbf{k} = K_M, w_0, w_1) + H^{(B1)}(\mathbf{k} = K_M, w_0, w_1) = 0$ to find the manifold (w_1, w_0) on which this condition happens. Notice that, *a priori*, there is no guarantee that the result of this condition will give a manifold that is anywhere near the values of w_1, w_0 considered in this paper, for which our set of approximations is valid (i.e., w_0, w_1 not much larger than $1/\sqrt{3}$). We find

$$H^{(1)}(\mathbf{k} = K_M, w_0, w_1) + H^{(B1)}(\mathbf{k} = K_M, w_0, w_1) = 0 \quad (58)$$

\Rightarrow

Two-band model degenerate at K_M :

$$w_1 = \frac{1}{32}(63\sqrt{w_0^2 + 1} - \sqrt{2977w_0^2 + 1953}). \quad (59)$$

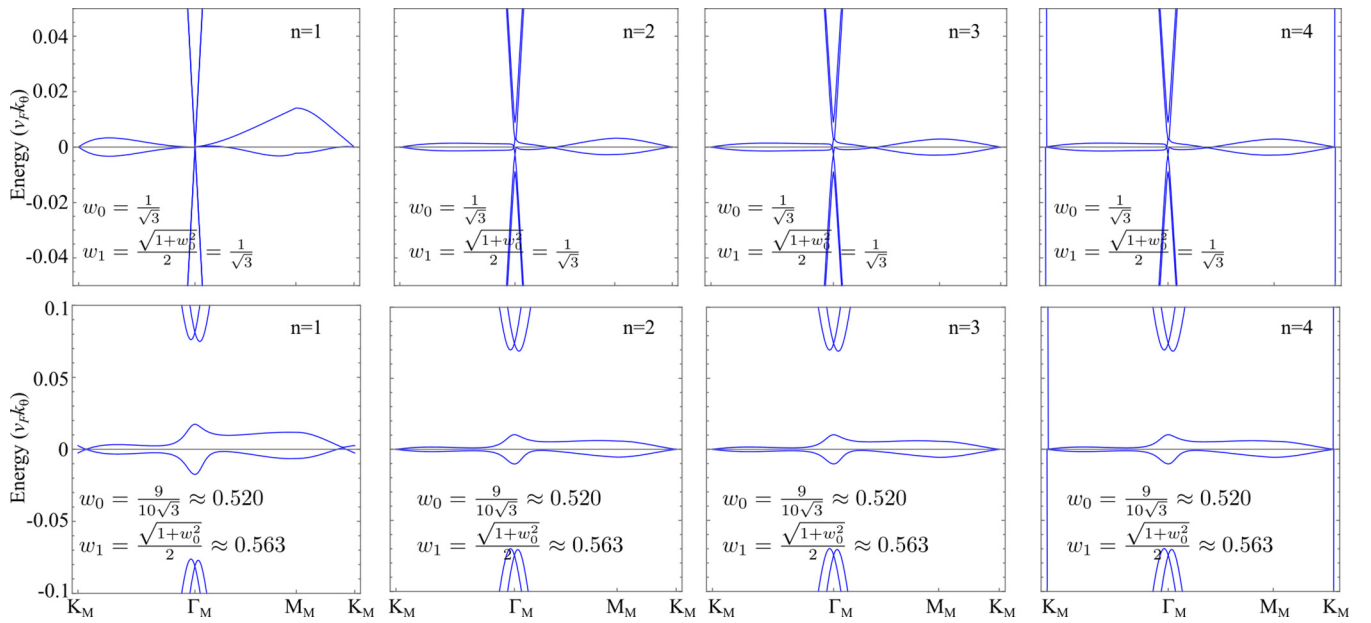


FIG. 13. Plots of the band structure for different parameters around the first magic angle, and for different ranges of the y axis. Notice no change from $n = 2$ to $n = 4$, in agreement with the theoretical discussions.

Remarkably, we note that as w_0 is tuned from $1/\sqrt{3}$ to 0, w_1 only changes from $(1/\sqrt{3}) = 0.57735$ and $\frac{3}{32}(21 - \sqrt{217}) = 0.587726$! Hence the isotropic point is included in this manifold, and w_1 changes by only about 2% as w_0 is tuned from the isotropic point to the chiral limit. We hence propose this model as a first, heuristic $k \cdot p$ model for the active bands on the $w_1(w_0)$ manifold in Eq. (58). Importantly, this model will have (A) flat bands with small bandwidth; (B) identical gap between the active bands at the Γ_M point with the TBG BM model; and (C) gap closing at the K_M point (Fig. 14).

V. CONCLUSIONS

In this paper we presented a series of analytically justified approximations to the physics of the BM model [1]. These

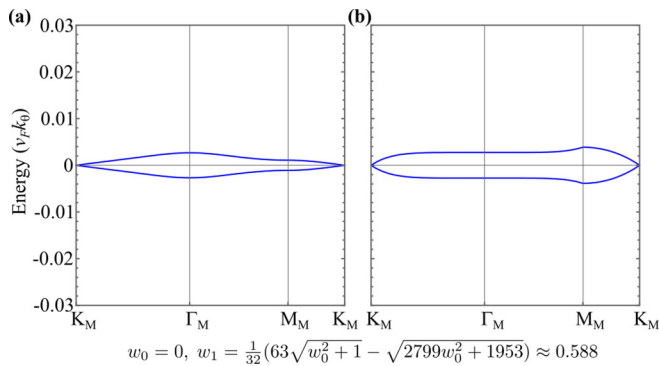


FIG. 14. Comparison between (a) the active bands of the BM model at the $w_0 = 0, w_1 \approx 0.588$ point and (b) the bands of the two-band first order approximation to $H_{\text{Approx1}}(\mathbf{k})$ in Eq. (33). Notice that the bandwidth at the Γ_M point is virtually identical, that the bands are flat, and that they close gap at the K_M point.

approximations allow for an analytic explanation of several properties of the BM model such as (1) the difficulty to stabilize the gap, in the isotropic limit from active to passive bands over a wide range of angles smaller than the first magic angle. (2) The *almost* double degeneracy of the passive bands in the isotropic limit, even away from the Γ_M point, where no symmetry forces them to be. (3) The determination of the high group velocities of the passive bands. (4) The flatness of the active bands even away from the Dirac point, around the magic angle which has $w_1 = 1/\sqrt{3}$. (5) The large gap, away from the isotropic limit (with $w_1 = 1/\sqrt{3}$), between the active and passive bands, which increases immediately with decreasing w_0 , while the bandwidth of the active bands does not increase. (6) The flatness of bands over the wide range of $w_0 \in [0, 1/\sqrt{3}]$, from chiral to the isotropic limit. Also, we provided a 2×2 $k \cdot p$ Hamiltonian for the active bands, which allowed for an analytic manifold on which the bandwidth is extremely small: $w_1 = 2\sqrt{w_0^2 + 1} - \sqrt{3w_0^2 + 2}$, $w_0 \in [0, 1/\sqrt{3}]$.

However, the most important feature uncovered in this paper is the development of an analytic perturbation theory which justifies neglecting most of the matrix elements [form factors/overlap matrices, see Eq. (19)], which will appear in the Coulomb interaction [108]. The exponential decay of these matrix elements with momentum will justify the use of the “flat metric condition” in Eq. (20) and allow for the determination of exact Coulomb interaction ground states and excitations [108–111].

Future research in the BM model is likely to uncover many surprises. Despite the apparent complexity of the model and the need for numerical diagonalization, one cannot help but think that there is a 2×2 $k \cdot p$ model valid over the whole area of the MBZ, for all w_0, w_1 around the first magic angle. Our two-band model is valid around the Γ_M point—for a large

interval but not for the entire MBZ, although we can fine tune to render the qualitative aspects valid at the K_M point also. A future goal is to find an approximate summation, based on our perturbative expansion, where outer shells can be taken into account more carefully and possibly summed together in a closed-form series, thereby leading to a much more accurate $k \cdot p$ model. We leave this for future research.

ACKNOWLEDGMENTS

We thank Aditya Cowsik and Fang Xie for valuable discussions. B.A.B. thanks Michael Zaletel, Christophe Mora, and

Oskar Vafek for fruitful discussions. This work was supported by the DOE Grant No. DE-SC0016239, the Schmidt Fund for Innovative Research, Simons Investigator Grant No. 404513, and the Packard Foundation. Further support was provided by the NSF-EAGER No. DMR 1643312, NSF-MRSEC No. DMR-1420541 and No. DMR-2011750, ONR No. N00014-20-1-2303, Gordon and Betty Moore Foundation through Grant GBMF8685 towards the Princeton theory program, BSF Israel US foundation No. 2018226, and the Princeton Global Network Funds. B.L. acknowledge the support of Princeton Center for Theoretical Science at Princeton University in the early stage of this work.

APPENDIX A: MATRIX ELEMENTS OF THE Γ_M -CENTERED MODEL

We introduce the shells in the Γ_M -centered model. The An_j sites of the n th A shell [see Fig. 4(a)] are situated at

$$\begin{aligned} Q_{An_j} &= (n-1)(q_1 - q_2) + (j-1)(q_2 - q_3) + q_1, \quad j = 1, \dots, n, \\ Q_{An_{n+j}} &= C_6 Q_{An_j} = (n-1)(q_1 - q_3) + (j-1)(q_2 - q_1) - q_3, \quad j = 1, \dots, n, \\ Q_{An_{2n+j}} &= C_6^2 Q_{An_j} = (n-1)(q_2 - q_3) + (j-1)(q_3 - q_1) + q_2, \quad j = 1, \dots, n, \\ Q_{An_{3n+j}} &= C_6^3 Q_{An_j} = (n-1)(q_2 - q_1) + (j-1)(q_3 - q_2) - q_1, \quad j = 1, \dots, n, \\ Q_{An_{4n+j}} &= C_6^4 Q_{An_j} = (n-1)(q_3 - q_1) + (j-1)(q_1 - q_2) + q_3, \quad j = 1, \dots, n, \\ Q_{An_{5n+j}} &= C_6^5 Q_{An_j} = (n-1)(q_3 - q_2) + (j-1)(q_1 - q_3) - q_2, \quad j = 1, \dots, n. \end{aligned} \quad (A1)$$

There are $6n$ A sites in the n th shell. The Bn_j sites of the n th B shell [see Fig. 4(a)] are situated at

$$\begin{aligned} Q_{Bn_j} &= Q_{An_j} + q_1, \quad Q_{Bn_{n+j}} = Q_{An_{n+j}} - q_3, \quad Q_{Bn_{2n+j}} = Q_{An_{2n+j}} + q_2, \\ Q_{Bn_{3n+j}} &= Q_{An_{3n+j}} - q_1, \quad Q_{Bn_{4n+j}} = Q_{An_{4n+j}} + q_2, \quad Q_{Bn_{5n+j}} = Q_{An_{5n+j}} - q_2, \quad j = 1, \dots, n. \end{aligned} \quad (A2)$$

There are $6n$ B sites in the n th shell. The basis we take for the BM Hamiltonian in Eq. (3) is then

$$(A1, B1, A2, B2, \dots, AN, BN) = (A1_1, A1_2, A1_3, A1_4, A1_5, A1_6, B1_1, B1_2, B1_3, B1_4, B1_5, B1_6, A2_1, A2_2, \dots), \quad (A3)$$

where N is the cutoff in the number of shells that we take. Each shell n has $6n$ A sites and $6n$ B sites.

The separation of shell $n = 1, \dots, \infty$ into A and B is necessary in the Γ_M -centered model due to the structure of the matrix elements. Unlike in the K_M -centered model, where different shells hop from one to another but *not* within a given shell, in the Γ_M -centered model, the A shells hop between themselves too. Explicitly, the nonzero matrix elements within the n th A shell are called $H_{An,An}$:

$$\begin{aligned} H_{An,An} &= An_n \leftrightarrow An_{n+1} : T_2; \quad An_{2n} \leftrightarrow An_{2n+1} : T_1; \quad An_{3n} \leftrightarrow An_{3n+1} : T_3; \\ &An_{4n} \leftrightarrow An_{4n+1} : T_2; \quad An_{5n} \leftrightarrow An_{5n+1} : T_1; \quad An_{6n} \leftrightarrow An_{6n+1} : T_3. \end{aligned} \quad (A4)$$

In the B shell there are no matrix elements between different B sites, but there are matrix elements between the A and B sites in the same shell n . They are called $H_{An,Bn}$ and the nonzero elements are

$$\begin{aligned} H_{An,Bn} &= An_j \leftrightarrow Bn_j : T_1; \quad An_{n+j} \leftrightarrow Bn_{n+j} : T_3; \quad An_{2n+j} \leftrightarrow Bn_{2n+j} : T_2; \\ &An_{3n+j} \leftrightarrow Bn_{3n+j} : T_1; \quad An_{4n+j} \leftrightarrow Bn_{4n+j} : T_3; \quad An_{5n+j} \leftrightarrow Bn_{5n+j} : T_2; \\ &j = 1, \dots, n, \quad n = 1, \dots, \infty. \end{aligned} \quad (A5)$$

Last set of couplings are between the $n-1$ th B shell $Bn-1$ and the n th shell An are $H_{Bn-1,An}$ with nonzero matrix elements given by

$$\begin{aligned} H_{Bn-1,An} &= Bn-1_j \leftrightarrow An_j : T_2, \quad j = 1, \dots, n-1; \quad Bn-1_{j-1} \leftrightarrow An_j : T_3, \quad j = 2, \dots, n; \\ &Bn-1_{n+j} \leftrightarrow An_{n+j} : T_1, \quad j = 1, \dots, n-1; \quad Bn-1_{n+j-1} \leftrightarrow An_{n+j} : T_2, \quad j = 2, \dots, n; \\ &Bn-1_{2n+j} \leftrightarrow An_{2n+j} : T_3, \quad j = 1, \dots, n-1; \quad Bn-1_{2n+j-1} \leftrightarrow An_{2n+j} : T_1, \quad j = 2, \dots, n; \\ &Bn-1_{3n+j} \leftrightarrow An_{3n+j} : T_2, \quad j = 1, \dots, n-1; \quad Bn-1_{3n+j-1} \leftrightarrow An_{3n+j} : T_3, \quad j = 2, \dots, n; \\ &Bn-1_{4n+j} \leftrightarrow An_{4n+j} : T_1, \quad j = 1, \dots, n-1; \quad Bn-1_{4n+j-1} \leftrightarrow An_{4n+j} : T_2, \quad j = 2, \dots, n; \\ &Bn-1_{5n+j} \leftrightarrow An_{5n+j} : T_3, \quad j = 1, \dots, n-1; \quad Bn-1_{5n+j-1} \leftrightarrow An_{5n+j} : T_1, \quad j = 2, \dots, n. \end{aligned} \quad (A6)$$

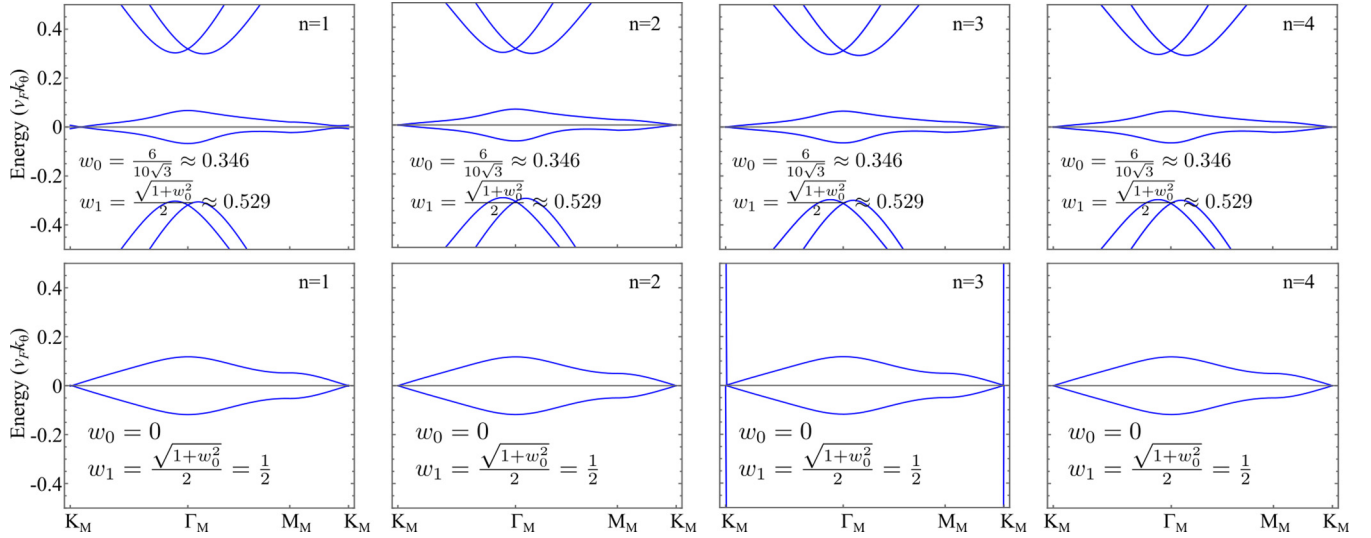


FIG. 15. Plots of the band structure for different parameters around the first magic angle, and for different ranges of the y axis. Notice no change from $n = 2$ to $n = 4$, in agreement with the theoretical discussions.

The diagonal matrix elements are $(k - Q)\sigma\delta_{Q,Q'}$ where the Q' , Q 's are given by the shell distance: We call these H_{kA_n} or H_{kB_n} depending on whether the Q is on the A or B shell. Note that the Hamiltonian within the B shell is H_{kB_n} while the Hamiltonian within the A shell is $H_{kA_n} + H_{A_n,A_n}$. We now have defined all the nonzero matrix elements of the Hamiltonian. In block-matrix form, it takes the expression

$$H = \begin{pmatrix} H_{kA1} + H_{A1,A1} & H_{A1,B1} & 0 & 0 & 0 & \cdots \\ H_{A1,B1}^\dagger & H_{kB1} & H_{B1,A2} & 0 & 0 & \cdots \\ 0 & H_{B1,A2}^\dagger & H_{kA2} + H_{A2,A2} & H_{A2,B2} & 0 & \cdots \\ 0 & 0 & H_{A2,B2}^\dagger & H_{kB2} & H_{B2,A3} & \cdots \\ 0 & 0 & 0 & H_{B2,A3}^\dagger & H_{kA3} + H_{A3,A3} & \cdots \\ \vdots & \vdots & \ddots & \vdots & \vdots & \ddots \end{pmatrix}.$$

APPENDIX B: NUMERICAL CONFIRMATION OF THE PERTURBATIVE FRAMEWORK

What our discussion in Secs. II D and II E shows is that: (1) For the first magic angle, we can neglect all shells greater than 2, while having a good approximation numerically. (2) For the next, smaller, magic angle, we need to keep more shells in order to obtain a good approximation. We have tested that *machine precision* convergence can be obtained for the active bands by choosing a cutoff of 5–6 shells. We test this next, along with other conclusions of Secs. II D and II E. In particular:

(1) We first confirm our analytic conclusion that shells above $n > 2$ do not change the spectrum for the first magic angle (and for larger angles than the first magic angle). Figures 14, 15, and 16 show the spectrum for several values of w_0 , w_1 around (or larger than) the first magic angle characterized by $w_0 = 1/\sqrt{3}$ for the K_M -centered model and by $w_0 = w_1 = 1/\sqrt{3}$ for the Γ_M -centered model in Sec. III. For the K_M -centered model, the magic angle does not depend on w_1 but for the Γ_M -centered model it does, see Sec. III. For either w_0 or $w_1 \leq 1/\sqrt{3}$, we see that the spectrum looks completely unchanged from $n = 2$ to $n = 4$ shells. From $n = 2$ to $n = 4$ shells, the largest change is smaller than 1%, and invisible to the naked eye. Above $n = 4$ shells, the spectrum

is numerically the same within machine precision. We confirm our first conclusion: *To obtain a faithful model for TBG around the first magic angle, we can safely neglect all shells above $n = 2$.* Keeping the $n = 2$ shells gives us a Hamiltonian which contains the $A1, B1, A2, B2$ shells in Fig. 4(a), giving a Hamiltonian that is a 72×72 matrix, too large for analytic tackling. Hence further approximations are necessary, as per Secs. II D and II E, which we further numerically confirm.

(2) We confirmed our perturbation theory predictions of Secs. II D and II E for angles smaller than the first magic angle. In Fig. 17 we confirm the analytic prediction that at angle $1/n$ times the first magic angle, we can neglect all the shells above $n + 1$.

(3) We confirmed our perturbation theory predictions Secs. II D and II E that—for the first magic angle and below ($w_0, w_1 \leq 1/\sqrt{3}$)—keeping only the first shell induces only a 20% error in the band structure. We have already established that keeping up to $n = 2$ shells at the first magic angle gives the correct band structure within less than 5%. Figures 14, 15, and 16 also contain the $n = 1$ shells band structure for a range of angles around and above the first magic angle $w_0, w_1 \geq 1/\sqrt{3}$. We see that the band structures differ little to very little, while keeping the main characteristics, from $n = 1$ to $n = 2$. In particular, in the chiral limit of $w_0 = 0$ and for $w_1 = 1/2$ (along what we call the *second magic manifold*, see

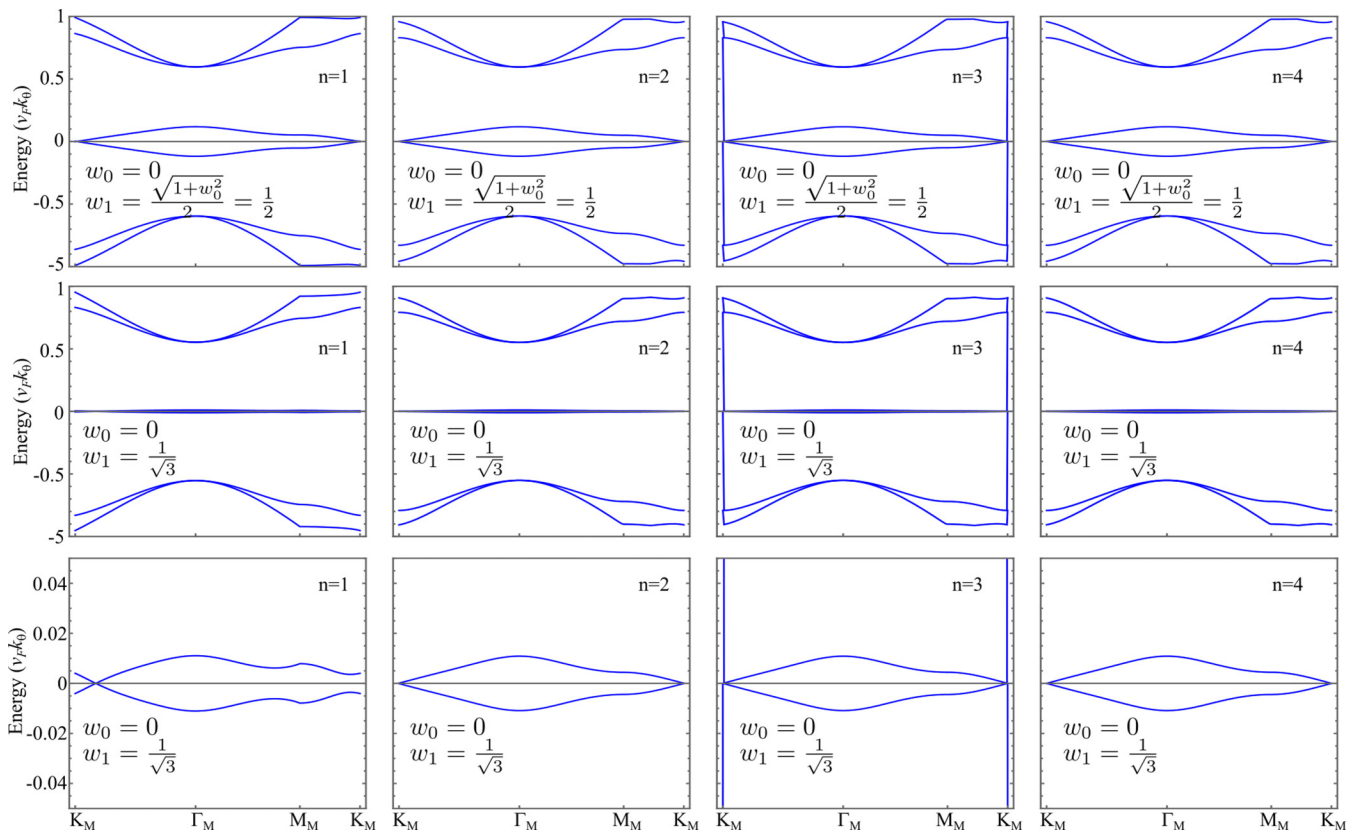


FIG. 16. Plots of the band structure for different parameters around the first magic angle, and for different ranges of the y axis. Notice no change from $n = 2$ to $n = 4$, in agreement with the theoretical discussions.

Sec. IV) the band structures do not visibly differ at all (see Fig. 15, lowest row) from $n = 1$ to $n = 2$. Hence for the first magic angle, to make analytic progress, we will consider only the $n = 1$ shell, to a good approximation. This gives a 24×24 Hamiltonian, which is still analytically unsolvable. Hence further approximations are necessary, such as $H_{\text{Approx1}}(\mathbf{k})$ in Eq. (33).

(4) We test the prediction that $H_{\text{Approx1}}(\mathbf{k})$ in Eq. (33) approximates well the band structure of TBG around (and for angles larger than) the magic angle for a series of

values of $w_0, w_1 \leq 1/\sqrt{3}$, Figs. 18, 19, and 20. We see remarkable agreement between $H_{\text{Approx1}}(\mathbf{k})$ and the $n = 1$ Hamiltonian. We also see good agreement with the large shell limit. For values of the parameters $w_0 = 0, w_1 = \frac{1}{2}$ in the second magic manifold (see Sec. IV), the $H_{\text{Approx1}}(\mathbf{k})$ and the $n = 1, 2, 3, \dots$ shells give rise to bands *undistinguishable by eye* (see Fig. 19, last row). We will hence use $H_{\text{Approx1}}(\mathbf{k})$ as our TBG Hamiltonian. This is a 12×12 Hamiltonian that cannot be solved analytically. Hence further analytic approximations are necessary.

APPENDIX C: EIGENSTATES OF THE HEXAGON MODEL AT THE Γ_M POINT

We provide the explicit expressions for the six-band model approximation for the hexagon model at $w_0 = w_1 = 1/\sqrt{3}$. The basis we choose is made of simultaneous eigenstates of C_{3z} and H for the states $|\psi_j(\mathbf{k} = 0, w_0 = w_1 = \frac{1}{\sqrt{3}})\rangle = |\psi_{E_j}, j = 1, \dots, 6$ in Eq. (41):

$$\psi_{E_1} = \begin{pmatrix} \zeta_1 \\ e^{-i(2\pi/3)\sigma_z} \eta_1 \\ e^{i(2\pi/3)\sigma_z} \zeta_1 \\ \eta_1 \\ e^{-i(2\pi/3)\sigma_z} \zeta_1 \\ e^{i(2\pi/3)\sigma_z} \eta_1 \end{pmatrix}, \quad \zeta_1 = \frac{1}{2\sqrt{2}} \begin{pmatrix} 1 \\ 1 \end{pmatrix}, \quad \eta_1 = \frac{1}{\sqrt{3}} (-2i\sigma_z - \sigma_y) \zeta_1 = \frac{1}{2\sqrt{6}} \begin{pmatrix} -i \\ i \end{pmatrix}, \quad (\text{C1})$$

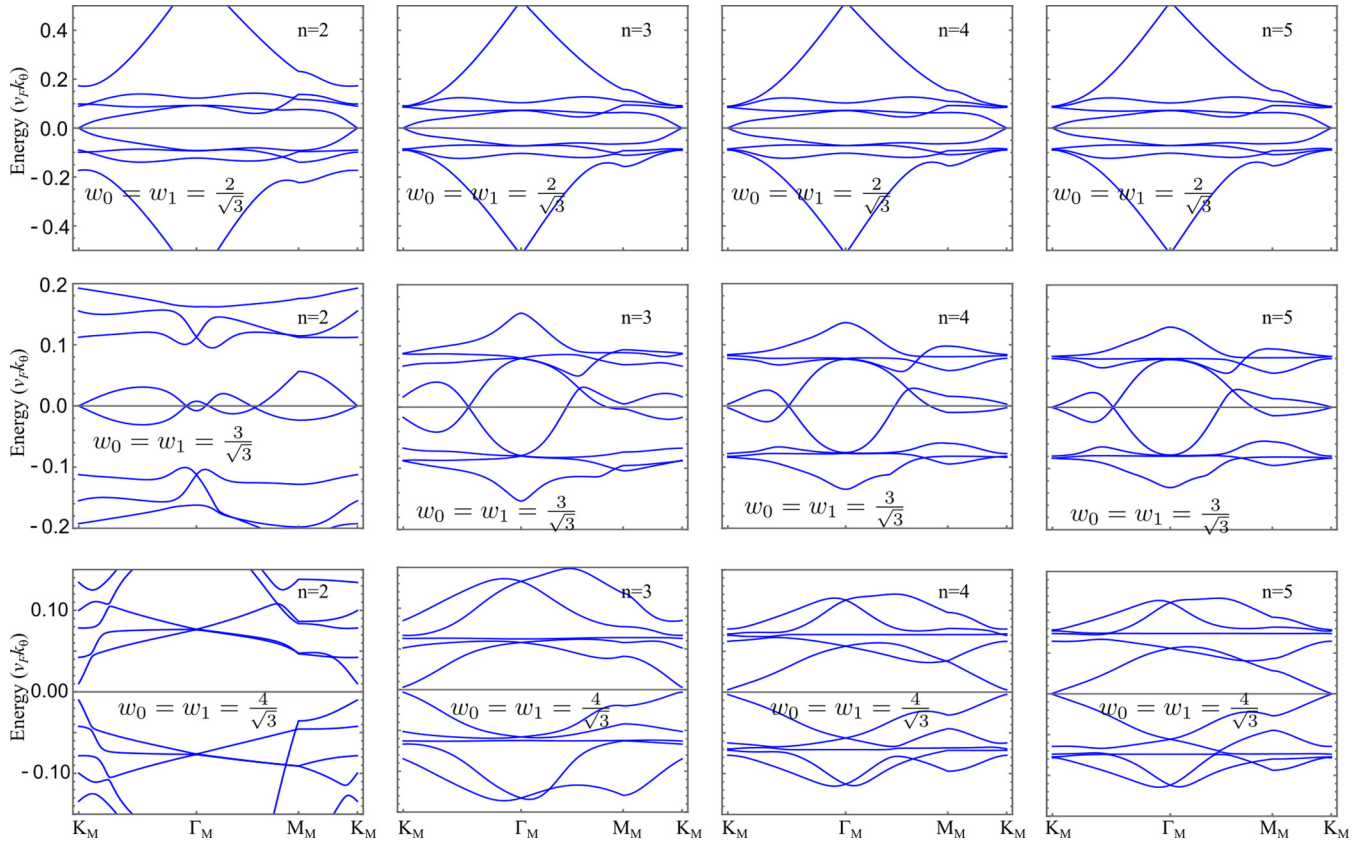


FIG. 17. Plots of the band structure for different parameters far away from the first magic angle: at half, a third, and a fourth of the first magic angle. Notice that for an angle $1/n$ times the magic angle we can neglect all shells above $n + 1$, which confirms our perturbation theory result. For the first magic angle, above $n = 2$ shells, the band structure goes not change. For half the magic angle, the band structure above $n = 3$ shells does not change (but the band structure at $n = 2$ shells is changed compared to the $n = 3$ band structure). For a third of the magic angle, the band structure above $n = 4$ shells does not change (but the band structure at $n = 2, 3$ shells is changed compared to the $n = 4$ band structure). For a quarter of the magic angle, the band structure above $n = 5$ shells does not change (but the band structure at $n = 2, 3, 4$ shells is changed—dramatically—compared to the $n = 6$ band structure).

$$\psi_{E_2} = \begin{pmatrix} \zeta_2 \\ e^{-i(2\pi/3)\sigma_z}\eta_2 \\ e^{i(2\pi/3)\sigma_z}\zeta_2 \\ \eta_2 \\ e^{-i(2\pi/3)\sigma_z}\zeta_2 \\ e^{i(2\pi/3)\sigma_z}\eta_2 \end{pmatrix}, \quad \zeta_2 = \frac{1}{2\sqrt{6}} \begin{pmatrix} 1 \\ -1 \end{pmatrix}, \quad \eta_2 = \frac{1}{\sqrt{3}}(-2i\sigma_z - \sigma_y)\zeta_2 = \frac{1}{2\sqrt{2}} \begin{pmatrix} -i \\ -i \end{pmatrix}, \quad (\text{C2})$$

$$\psi_{E_3} = \begin{pmatrix} \zeta_3 \\ e^{-i(2\pi/3)(\sigma_z - \sigma_0)}\eta_3 \\ e^{i(2\pi/3)(\sigma_z - \sigma_0)}\zeta_3 \\ \eta_3 \\ e^{-i(2\pi/3)(\sigma_z - \sigma_0)}\zeta_3 \\ e^{i(2\pi/3)(\sigma_z - \sigma_0)}\eta_3 \end{pmatrix}, \quad \zeta_3 = \frac{1}{\sqrt{26(5 - \sqrt{13})}} \begin{pmatrix} 2 \\ 3 - \sqrt{13} \end{pmatrix},$$

$$\eta_3 = \frac{1}{\sqrt{3}} \left(\frac{\sigma_y}{2} + \frac{3i}{2}\sigma_x + i\sigma_z \right) \zeta_3 = \frac{i}{\sqrt{78(5 - \sqrt{13})}} \begin{pmatrix} 5 - \sqrt{13} \\ 1 + \sqrt{13} \end{pmatrix}, \quad (\text{C3})$$

$$\psi_{E_4} = \begin{pmatrix} \zeta_4 \\ e^{-i(2\pi/3)(\sigma_z - \sigma_0)}\eta_4 \\ e^{i(2\pi/3)(\sigma_z - \sigma_0)}\zeta_4 \\ \eta_4 \\ e^{-i(2\pi/3)(\sigma_z - \sigma_0)}\zeta_4 \\ e^{i(2\pi/3)(\sigma_z - \sigma_0)}\eta_4 \end{pmatrix}, \quad \zeta_4 = \frac{1}{\sqrt{26(5 + \sqrt{13})}} \begin{pmatrix} 2 \\ 3 + \sqrt{13} \end{pmatrix},$$

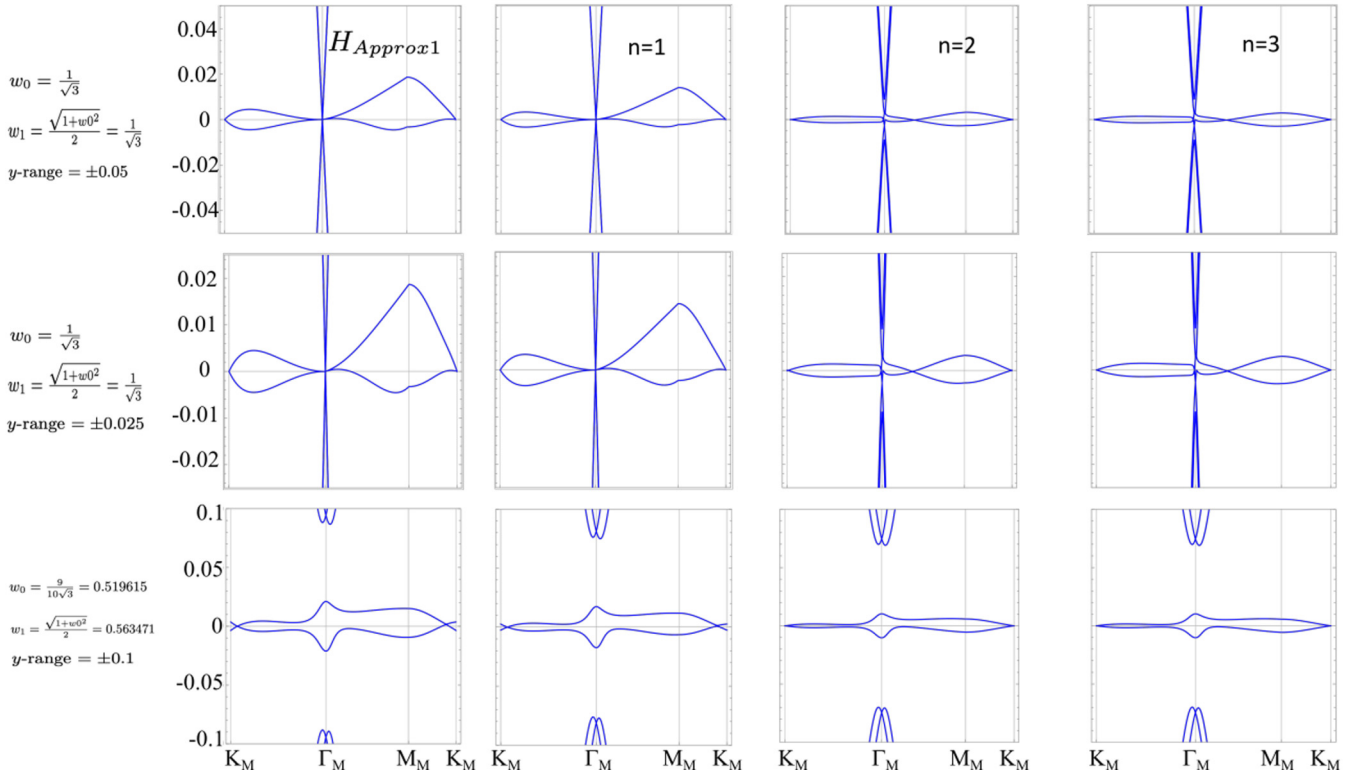


FIG. 18. Plots of the band structure of H_{Approx1} for different parameters around the first magic angle, and for different ranges of the y axis. For convenience we also replot the $n = 1, 2, 3$ shells band structure. Notice the good agreement of H_{Approx1} with the $n = 1$ shell Hamiltonian, and, further on, the good approximation of the $n = 2, 3$ band structures by this Hamiltonian. For the chiral limit $w_0 = 9/10\sqrt{3}$, $w_1 = \sqrt{1 + w_0^2}/2$, the approximate H_{Approx1} is a remarkably good approximation of the $n = 1$ shell and a good approximation to the thermodynamic limit, albeit with the Dirac point slightly shifted.

$$\eta_4 = \frac{1}{\sqrt{3}} \left(\frac{\sigma_y}{2} + \frac{3i}{2} \sigma_x + i\sigma_z \right) \zeta_4 = \frac{i}{\sqrt{78(5 + \sqrt{13})}} \begin{pmatrix} 5 + \sqrt{13} \\ 1 - \sqrt{13} \end{pmatrix}, \quad (\text{C4})$$

$$\psi_{E_5} = \begin{pmatrix} \zeta_5 \\ e^{-i(2\pi/3)(\sigma_z + \sigma_0)} \eta_5 \\ e^{i(2\pi/3)(\sigma_z + \sigma_0)} \zeta_5 \\ \eta_5 \\ e^{-i(2\pi/3)(\sigma_z + \sigma_0)} \zeta_5 \\ e^{i(2\pi/3)(\sigma_z + \sigma_0)} \eta_5 \end{pmatrix}, \quad \zeta_5 = \frac{1}{\sqrt{26(5 - \sqrt{13})}} \begin{pmatrix} 3 - \sqrt{13} \\ 2 \end{pmatrix},$$

$$\eta_5 = \frac{1}{\sqrt{3}} \left(\frac{\sigma_y}{2} - \frac{3i}{2} \sigma_x + i\sigma_z \right) \zeta_5 = \frac{-i}{\sqrt{78(5 - \sqrt{13})}} \begin{pmatrix} 1 + \sqrt{13} \\ 5 - \sqrt{13} \end{pmatrix}, \quad (\text{C5})$$

$$\psi_{E_6} = \begin{pmatrix} \zeta_6 \\ e^{-i(2\pi/3)(\sigma_z + \sigma_0)} \eta_6 \\ e^{i(2\pi/3)(\sigma_z + \sigma_0)} \zeta_6 \\ \eta_6 \\ e^{-i(2\pi/3)(\sigma_z + \sigma_0)} \zeta_6 \\ e^{i(2\pi/3)(\sigma_z + \sigma_0)} \eta_6 \end{pmatrix}, \quad \zeta_6 = \frac{1}{\sqrt{26(5 + \sqrt{13})}} \begin{pmatrix} 3 + \sqrt{13} \\ 2 \end{pmatrix},$$

$$\eta_6 = \frac{1}{\sqrt{3}} \left(\frac{\sigma_y}{2} + \frac{3i}{2} \sigma_x + i\sigma_z \right) \zeta_6 = \frac{-i}{\sqrt{78(5 + \sqrt{13})}} \begin{pmatrix} 1 - \sqrt{13} \\ 5 + \sqrt{13} \end{pmatrix}. \quad (\text{C6})$$

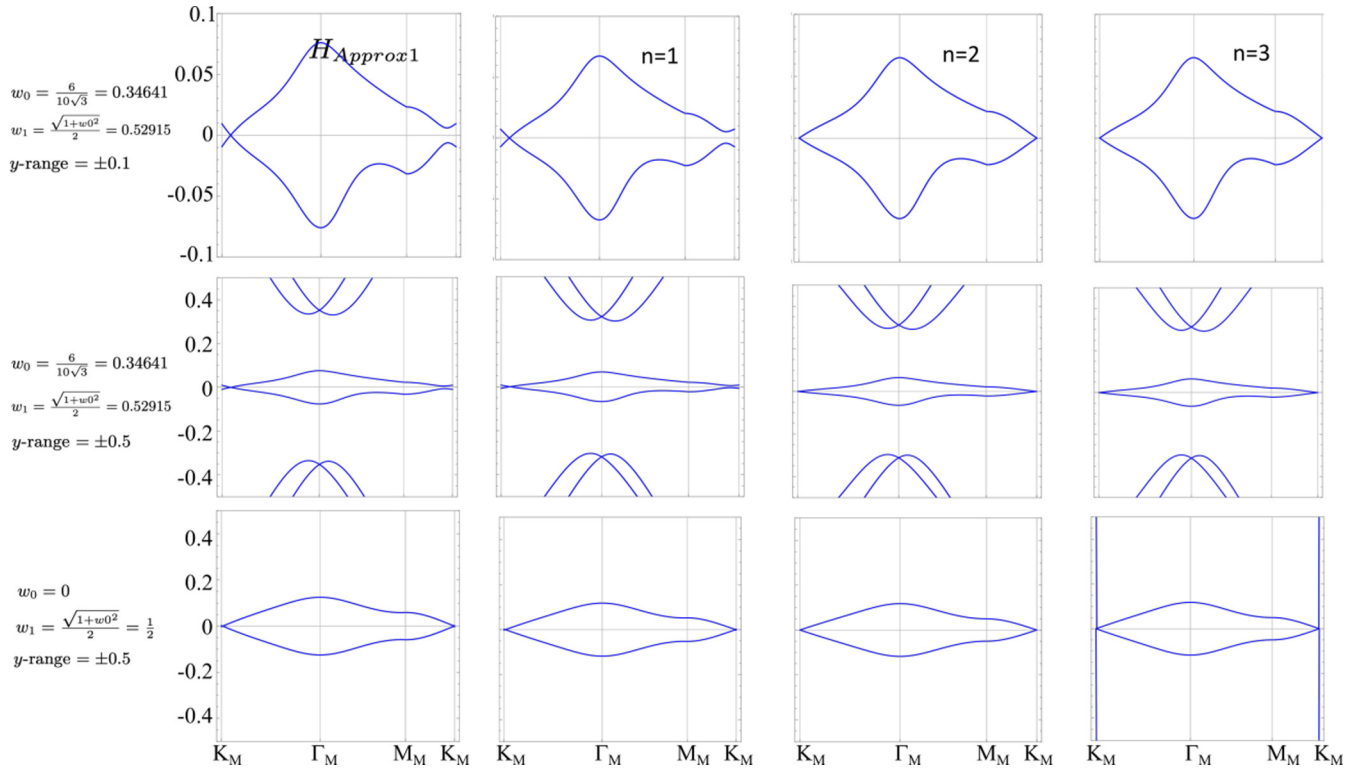


FIG. 19. Plots of the band structure of H_{Approx1} for different parameters around the first magic angle, and for different ranges of the y axis, which helps us focus on different bands. For convenience we also replot the $n = 1, 2, 3$ shells band structure. Notice the remarkable (almost undistinguishable by eye) agreement of H_{Approx1} with the $n = 1$ shell Hamiltonian, and the, further on, good approximation of the $n = 2, 3$ band structures by this Hamiltonian. For the chiral limit $w_0 = 0, w_1 = 1/2$, the approximate H_{Approx1} is a remarkably good approximation of the thermodynamic limit—undistinguishable by eye—while for all other values it is a very good approximation. The Dirac point in the chiral limit $w_0 = 0, w_1 = \sqrt{1 + w_0^2}/2$ is at K_M even for the H_{Approx1} .

The basis ψ_{E_1}, ψ_{E_2} has $C_{3z} = 1$, the basis ψ_{E_3}, ψ_{E_4} has $C_{3z} = e^{i2\pi/3}$, and the basis ψ_{E_5}, ψ_{E_6} has $C_{3z} = e^{-i2\pi/3}$. The 6 by 6 Hamiltonian in Eq. (41) under these 6 basis takes the form

$$H_{ij}^{6\text{-band}}\left(\mathbf{k}, w_0 = w_1 = \frac{1}{\sqrt{3}}\right) = \begin{pmatrix} 0_2 & A_1 k_- & A_2^\dagger k_+ \\ A_1^\dagger k_+ & 0_2 & A_3 k_- \\ A_2 k_- & A_3^\dagger k_+ & 0_2 \end{pmatrix}, \quad (\text{C7})$$

where $k_\pm = k_x \pm ik_y$, 0_2 is the 2 by 2 zero matrix, and

$$A_1 = \begin{pmatrix} \frac{2\sqrt{13}-13}{13\sqrt{5-\sqrt{13}}} & \frac{\sqrt{6\sqrt{13}+22}-1}{\sqrt{13(\sqrt{13}+5)}} \\ \frac{1}{52}(\sqrt{13}-13)\sqrt{\sqrt{13}+5} & \sqrt{\frac{1}{26}(\sqrt{13}+4)} - \sqrt{\frac{3}{13(\sqrt{13}+5)}} \end{pmatrix},$$

$$A_2 = \begin{pmatrix} \frac{2\sqrt{13}-13}{13\sqrt{5-\sqrt{13}}} & -\frac{1}{52}(\sqrt{13}-13)\sqrt{\sqrt{13}+5} \\ \frac{\sqrt{6\sqrt{13}+22}-1}{\sqrt{13(\sqrt{13}+5)}} & -\sqrt{\frac{1}{26}(\sqrt{13}+4)} + \sqrt{\frac{3}{13(\sqrt{13}+5)}} \end{pmatrix}, \quad (\text{C8})$$

$$A_3 = \begin{pmatrix} \frac{1}{\sqrt{13}} & \frac{2\sqrt{13}-5\sqrt{6\sqrt{13}+22}+\sqrt{78\sqrt{13}+286}+2}{52\sqrt{3}} \\ \frac{2\sqrt{13}-5\sqrt{6\sqrt{13}+22}+\sqrt{78\sqrt{13}+286}+2}{52\sqrt{3}} & \frac{2(\sqrt{13}+8)-\sqrt{6\sqrt{13}+22}+\sqrt{78\sqrt{13}+286}}{26(\sqrt{13}+2)} \end{pmatrix}.$$

We note that ψ_{E_1}, ψ_{E_2} also serves as the Gamma point basis of the two-band approximation at $w_1 = \sqrt{1 + w_0^2}/2$ in Sec. IV.

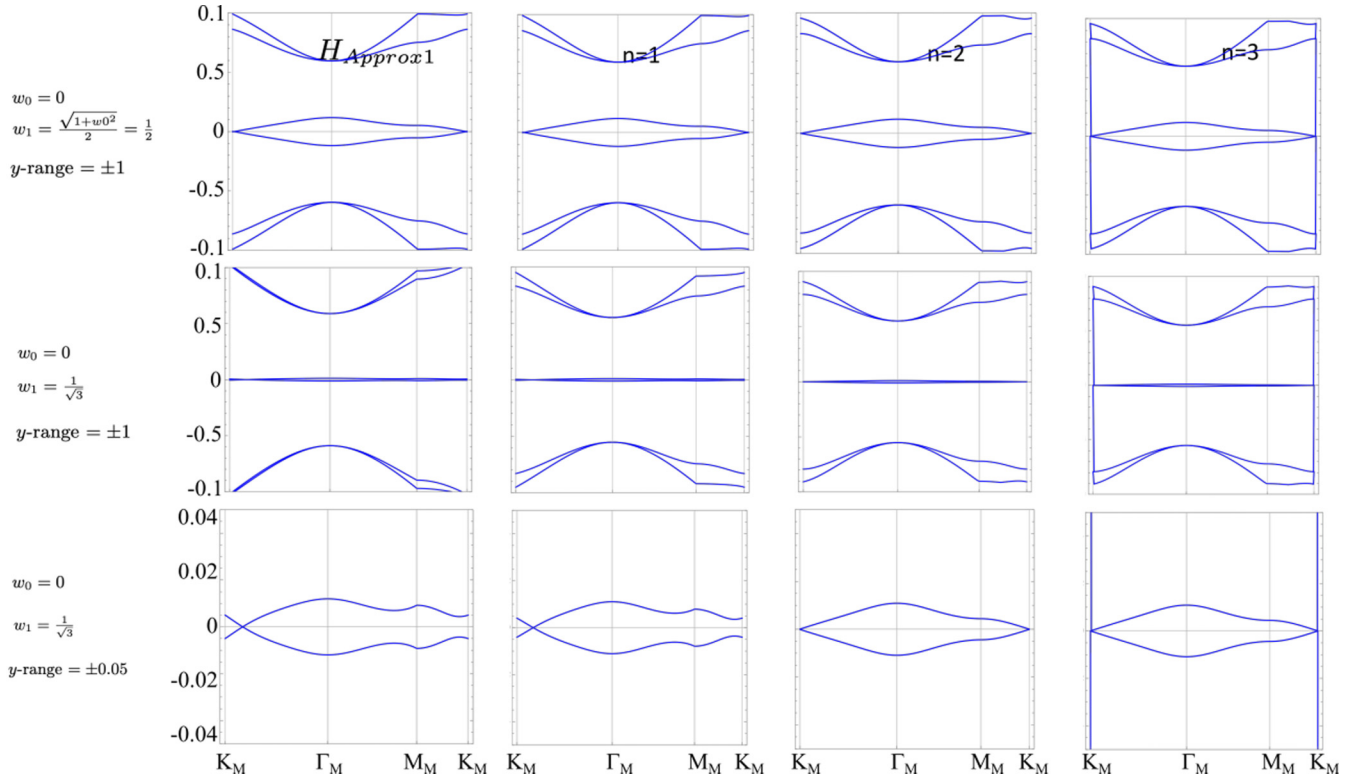


FIG. 20. Plots of the band structure of H_{Approx1} for different parameters around the first magic angle, and for different ranges of the y axis, which helps us focus on different bands. For convenience we also replot the $n = 1, 2, 3$ shells band structure. Notice the remarkable (almost undistinguishable by eye) agreement of H_{Approx1} with the $n = 1$ shell Hamiltonian, and the, further on, good approximation of the $n = 2, 3$ band structures by this Hamiltonian. For the chiral limit $w_0 = 0$, $w_1 = 1/\sqrt{3}$, the approximate H_{Approx1} is a remarkably good approximation of the $n = 1$ Hamiltonian, and a good approximation to the thermodynamic limit. The Dirac point is slightly moved away from the K_M point.

APPENDIX D: EIGENSTATES OF ALONG THE Γ_M - K_M LINE $k_x = 0$ AND ON THE Γ_M - M_M LINE $k_y = 0$

1. Eigenstates of $H_{ij}^{6\text{-band}}[\mathbf{k} = (0, k_y), w_0 = w_1 = \frac{1}{\sqrt{3}}]$

On the Γ_M - K_M line, the energies (already mentioned in the main text) are

$$E_{6\text{-band}}\left[\mathbf{k} = (0, k_y), w_0 = w_1 = \frac{1}{\sqrt{3}}\right] = \left(-2\sqrt{\frac{3}{13}}k_y, -2\sqrt{\frac{3}{13}}k_y, 2\sqrt{\frac{3}{13}}k_y, 2\sqrt{\frac{3}{13}}k_y, 0, 0\right). \quad (\text{D1})$$

The energies have eigenstates (not orthonormalized yet)

$$\begin{aligned} & \psi_{1;6\text{-band}}\left[\mathbf{k} = (0, k_y), w_0 = w_1 = \frac{1}{\sqrt{3}}\right] \\ &= \left(-\frac{1}{200}\sqrt{\frac{1}{221}}(5570051i\sqrt{3} - 153112\sqrt{13} + 1077176i\sqrt{39} + 17078669), \right. \\ & \quad \frac{191760161i\sqrt{3} + 166713618\sqrt{13} - 59265370i\sqrt{39} - 527508405}{200\sqrt{2074}(13477\sqrt{13} - 45994)}, \\ & \quad \left. \frac{-2437915i\sqrt{3} + 698430\sqrt{13} + 569554i\sqrt{39} - 3303424}{100\sqrt{22570}(49\sqrt{13} - 156)}, \frac{23i(26i - 1222\sqrt{3} + 86i\sqrt{13} + 221\sqrt{39})}{1300\sqrt{370}}, 0, 1 \right), \end{aligned}$$

$$\begin{aligned} & \psi_{2;6\text{-band}}\left[\mathbf{k} = (0, k_y), w_0 = w_1 = \frac{1}{\sqrt{3}}\right] \\ &= \left(\frac{1}{200}(-23)\sqrt{\frac{1}{221}}(37641i\sqrt{3} + 808\sqrt{13} - 2136i\sqrt{39} - 91159), \right. \end{aligned}$$

$$\begin{aligned}
& \frac{23}{100} \sqrt{\frac{705768\sqrt{13} - 8i\sqrt{39(886369537 - 160909896\sqrt{13})} + 4606081}{26962}}, \\
& \frac{23[-881719i\sqrt{3} + 56(-687 + 3704i\sqrt{3})\sqrt{13} + 52881]}{600\sqrt{22570}(49\sqrt{13} - 156)}, \frac{104(775 - 596i\sqrt{3}) + 529i(25\sqrt{3} + 23i)\sqrt{13}}{2600\sqrt{370}}, 1, 0), \\
\psi_{3;6\text{-band}} & \left[\mathbf{k} = (0, k_y), w_0 = w_1 = \frac{1}{\sqrt{3}} \right] \\
& = \left(\frac{1}{200} \sqrt{\frac{1}{221} (5570051i\sqrt{3} + 8(19139 - 134647i\sqrt{3})\sqrt{13} + 17078669)}, \right. \\
& \quad \left. \frac{-191760161i\sqrt{3} + 166713618\sqrt{13} - 59265370i\sqrt{39} + 527508405}{200\sqrt{2074}(13477\sqrt{13} + 45994)}, \right. \\
& \quad \left. \frac{2437915i\sqrt{3} + 698430\sqrt{13} + 569554i\sqrt{39} + 3303424}{100\sqrt{22570}(49\sqrt{13} + 156)}, \frac{23(-1222i\sqrt{3} + 86\sqrt{13} - 221i\sqrt{39} - 26)}{1300\sqrt{370}}, 0, 1 \right), \\
\psi_{4;6\text{-band}} & \left[\mathbf{k} = (0, k_y), w_0 = w_1 = \frac{1}{\sqrt{3}} \right] \\
& = \left(\frac{23}{200} \sqrt{\frac{1}{221} i(91159i + 37641\sqrt{3} + 808i\sqrt{13} + 2136\sqrt{39})}, \right. \\
& \quad \left. \frac{23}{100} \sqrt{\frac{-705768\sqrt{13} + 8i\sqrt{39}(160909896\sqrt{13} + 886369537) + 4606081}{26962}}, \right. \\
& \quad \left. \frac{23i[52881i + 881719\sqrt{3} + 56\sqrt{13}(3704\sqrt{3} + 687i)]}{600\sqrt{22570}(49\sqrt{13} + 156)}, \frac{104(775 - 596i\sqrt{3}) + 529(23 - 25i\sqrt{3})\sqrt{13}}{2600\sqrt{370}}, 1, 0 \right), \\
\psi_{5;6\text{-band}} & \left[\mathbf{k} = (0, k_y), w_0 = w_1 = \frac{1}{\sqrt{3}} \right] \\
& = \left(\frac{1}{529} \sqrt{\frac{2}{51}} (710 - 19i\sqrt{3}), \frac{2}{529} \sqrt{\frac{2}{1037}} (-2732 + 659i\sqrt{3}), -\frac{1}{529} \sqrt{\frac{185}{61}} (2483 + 5763i\sqrt{3}), 0, \frac{1}{46} (47 - 19i\sqrt{3}), 1 \right), \\
\psi_{6;6\text{-band}} & \left[\mathbf{k} = (0, k_y), w_0 = w_1 = \frac{1}{\sqrt{3}} \right] \\
& = \left(\frac{1}{46} \sqrt{\frac{185}{17}} (5\sqrt{3} + 11i), \frac{1}{46} \sqrt{\frac{185}{1037}} (-57 - 71i\sqrt{3}), \frac{3(31 - 46i\sqrt{3})}{23\sqrt{61}}, 1, 0, 0 \right). \tag{D2}
\end{aligned}$$

Fundamentally, what we notice is that the bands are k_y independent!

2. Eigenstates of $H_{ij}^{6\text{-band}}[\mathbf{k} = (k_x, 0), w_0 = w_1 = \frac{1}{\sqrt{3}}]$

On the Γ_M - M_M line, the energies (already mentioned in the main text) are

$$\begin{aligned}
& E_{6\text{-band}} \left[\mathbf{k} = (k_x, 0), w_0 = w_1 = \frac{1}{\sqrt{3}} \right] \\
& = \left(-k_x, -k_x, \frac{1}{26} (3\sqrt{13} + 13)k_x, \frac{1}{26} (3\sqrt{13} + 13)k_x, -\frac{1}{26} (3\sqrt{13} - 13)k_x, -\frac{1}{26} (3\sqrt{13} - 13)k_x \right). \tag{D3}
\end{aligned}$$

The energies have eigenstates (not orthonormalized yet)

$$\begin{aligned}
& \psi_{1;6\text{-band}} \left[\mathbf{k} = (k_x, 0), w_0 = w_1 = \frac{1}{\sqrt{3}} \right] \\
& = \left(-\frac{219\sqrt{3} + 115i}{52\sqrt{34}}, \frac{1609 - 63i\sqrt{3}}{52\sqrt{2074}}, \frac{3(1253 + 41i\sqrt{3})}{52\sqrt{22570}}, \frac{69(-5 - 3i\sqrt{3})}{52\sqrt{370}}, 0, 1 \right),
\end{aligned}$$

$$\begin{aligned}
& \psi_{2;6\text{-band}} \left[\mathbf{k} = (k_x, 0), w_0 = w_1 = \frac{1}{\sqrt{3}} \right] \\
&= \left(\frac{69\sqrt{\frac{3}{34}}}{26}, \frac{69(9 - i\sqrt{3})}{52\sqrt{2074}}, -\frac{23i(\sqrt{3} - 151i)}{52\sqrt{22570}}, \frac{277 - 112i\sqrt{3}}{26\sqrt{370}}, 1, 0 \right), \\
& \psi_{3;6\text{-band}} \left[\mathbf{k} = (k_x, 0), w_0 = w_1 = \frac{1}{\sqrt{3}} \right] \\
&= \left(\frac{7(-10569i\sqrt{3} + 17434\sqrt{13} - 2949i\sqrt{39} + 62876)}{\sqrt{34}(3\sqrt{3} - i)(323\sqrt{13} - 65)}, \frac{481425i\sqrt{3} + 307265\sqrt{13} + 145119i\sqrt{39} + 1454167}{4\sqrt{2074}(323\sqrt{13} - 65)}, \right. \\
&\quad \times \left. \frac{9i(10385i + 10526\sqrt{3} + 4333i\sqrt{13} + 736\sqrt{39})}{2\sqrt{22570}(61\sqrt{13} - 247)}, \frac{69(169i\sqrt{3} + 8\sqrt{13} - 45i\sqrt{39} + 26)}{52\sqrt{370}(8\sqrt{13} - 29)}, 0, 1 \right), \\
& \psi_{4;6\text{-band}} \left[\mathbf{k} = (k_x, 0), w_0 = w_1 = \frac{1}{\sqrt{3}} \right] \\
&= \left(\frac{69(-1679i\sqrt{3} + 5303\sqrt{13} - 457i\sqrt{39} + 19129)}{2\sqrt{34}(3\sqrt{3} - i)(323\sqrt{13} - 65)}, \frac{69(6479i\sqrt{3} + 3374\sqrt{13} + 1939i\sqrt{39} + 12004)}{2\sqrt{2074}(323\sqrt{13} - 65)}, \right. \\
&\quad \left. \frac{23i(16877i + 3295\sqrt{3} + 4843i\sqrt{13} + 2705\sqrt{39})}{4\sqrt{22570}(61\sqrt{13} - 247)}, \frac{-36205i\sqrt{3} - 14941\sqrt{13} + 10699i\sqrt{39} + 64675}{104\sqrt{370}(8\sqrt{13} - 29)}, 1, 0 \right), \\
& \psi_{5;6\text{-band}} \left[\mathbf{k} = (k_x, 0), w_0 = w_1 = \frac{1}{\sqrt{3}} \right] \\
&= \left(\frac{69(-1679i\sqrt{3} + 5303\sqrt{13} - 457i\sqrt{39} + 19129)}{2\sqrt{34}(3\sqrt{3} - i)(323\sqrt{13} - 65)}, \frac{69(6479i\sqrt{3} + 3374\sqrt{13} + 1939i\sqrt{39} + 12004)}{2\sqrt{2074}(323\sqrt{13} - 65)}, \right. \\
&\quad \left. \frac{23i(16877i + 3295\sqrt{3} + 4843i\sqrt{13} + 2705\sqrt{39})}{4\sqrt{22570}(61\sqrt{13} - 247)}, \frac{-36205i\sqrt{3} - 14941\sqrt{13} + 10699i\sqrt{39} + 64675}{104\sqrt{370}(8\sqrt{13} - 29)}, 1, 0 \right), \\
& \psi_{6;6\text{-band}} \left[\mathbf{k} = (k_x, 0), w_0 = w_1 = \frac{1}{\sqrt{3}} \right] \\
&= \left(\frac{69(1679i\sqrt{3} + 5303\sqrt{13} - 457i\sqrt{39} - 19129)}{2\sqrt{34}(3\sqrt{3} - i)(323\sqrt{13} + 65)}, \frac{69(-6479i\sqrt{3} + 3374\sqrt{13} + 1939i\sqrt{39} - 12004)}{2\sqrt{2074}(323\sqrt{13} + 65)}, \right. \\
&\quad \left. \frac{23(-3295i\sqrt{3} - 4843\sqrt{13} + 2705i\sqrt{39} + 16877)}{4\sqrt{22570}(61\sqrt{13} + 247)}, \frac{i(64675i + 36205\sqrt{3} + 14941i\sqrt{13} + 10699\sqrt{39})}{104\sqrt{370}(8\sqrt{13} + 29)}, 1, 0 \right). \quad (\text{D4})
\end{aligned}$$

Fundamentally, what we notice is that the bands are k_x independent!

APPENDIX E: SOLUTIONS OF EIGENSTATES FOR THE HEXAGON MODEL

We now solve the eigenvalue equation

$$H_{\text{Hex}}(\mathbf{k}, w_0, w_1)\psi = E\psi \quad (\text{E1})$$

for the hexagon model in Eq. (40) in the basis $\psi(\mathbf{k}, w_0, w_1) = (\psi_{A11}, \psi_{A12}, \psi_{A13}, \psi_{A14}, \psi_{A15}, \psi_{A16})(\mathbf{k}, w_0, w_1)$ where each $\psi_{A1i}(\mathbf{k}, w_0, w_1)$ is a two-component spinor of Fig. 8, for different values of \mathbf{k}, w_0, w_1 .

1. Eigenstate solution at $\mathbf{k} = 0$ for arbitrary w_0, w_1

The eigenvalue equation cannot be solved for general \mathbf{k}, w_0, w_1 and we hence concentrate on several cases. First, we only can solve only the $\mathbf{k} = 0$ point. Using $|\vec{q}_i \cdot \vec{\sigma}| = 1$, we find

$$\begin{aligned}
\psi_6 &= \frac{E + q_2 \cdot \sigma}{E^2 - 1} (T_1\psi_5 + T_3\psi_1), & \psi_4 &= \frac{E + q_1 \cdot \sigma}{E^2 - 1} (T_3\psi_3 + T_2\psi_5), & \psi_2 &= \frac{E + q_3 \cdot \sigma}{E^2 - 1} (T_2\psi_1 + T_1\psi_3), \\
[(E + q_3 \cdot \sigma)(E^2 - 1) - E(T_2^2 + T_1^2) - T_2q_1 \cdot \sigma T_2 - T_1q_2 \cdot \sigma T_1] \psi_5 &= T_2(E + q_1 \cdot \sigma)T_3\psi_3 + T_1(E + q_2 \cdot \sigma)T_3\psi_1, \\
[(E + q_2 \cdot \sigma)(E^2 - 1) - E(T_1^2 + T_3^2) - T_1q_3 \cdot \sigma T_1 - T_3q_1 \cdot \sigma T_3] \psi_3 &= T_1(E + q_3 \cdot \sigma)T_2\psi_1 + T_3(E + q_1 \cdot \sigma)T_2\psi_5, \\
[(E + q_1 \cdot \sigma)(E^2 - 1) - E(T_2^2 + T_3^2) - T_2q_3 \cdot \sigma T_2 - T_3q_2 \cdot \sigma T_3] \psi_1 &= T_2(E + q_3 \cdot \sigma)T_1\psi_3 + T_3(E + q_2 \cdot \sigma)T_1\psi_5, \quad (\text{E2})
\end{aligned}$$

where shorthand notation $T_i = T_i(w_0, w_1)$, $\psi_i = \psi_{A_i}(\mathbf{k} = 0, w_0, w_1)$. Using the expressions of T_i from Eq. (4), we rewrite the last three equations above as

$$\begin{aligned}
& [E(E^2 - 1)\sigma_0 + q_3 \cdot \sigma(E^2 - 1 + w_0^2 + 2w_1^2) - E(2(w_0^2 + w_1^2)\sigma_0 + w_0w_1(\sigma_x + \sqrt{3}\sigma_y))] \psi_5 \\
&= \left\{ E \left[\left(w_0^2 - \frac{w_1^2}{2} \right) \sigma_0 - w_0w_1\sigma_x + \frac{i\sqrt{3}}{2} w_1^2 \sigma_z \right] + (w_0^2 - w_1^2) q_1 \cdot \sigma \right\} \psi_3 \\
&+ \left\{ E \left[\left(w_0^2 - \frac{w_1^2}{2} \right) \sigma_0 + w_0w_1 \frac{1}{2} (\sigma_x - \sqrt{3}\sigma_y) - \frac{i\sqrt{3}}{2} w_1^2 \sigma_z \right] + (w_0^2 - w_1^2) q_2 \cdot \sigma \right\} \psi_1, \\
& [E(E^2 - 1)\sigma_0 + q_2 \cdot \sigma(E^2 - 1 + w_0^2 + 2w_1^2) - E(2(w_0^2 + w_1^2)\sigma_0 + w_0w_1(\sigma_x - \sqrt{3}\sigma_y))] \psi_3 \\
&= \left\{ E \left[\left(w_0^2 - \frac{w_1^2}{2} \right) \sigma_0 + w_0w_1 \frac{1}{2} (\sigma_x + \sqrt{3}\sigma_y) + \frac{i\sqrt{3}}{2} w_1^2 \sigma_z \right] + (w_0^2 - w_1^2) q_3 \cdot \sigma \right\} \psi_1 \\
&+ \left\{ E \left[\left(w_0^2 - \frac{w_1^2}{2} \right) \sigma_0 - w_0w_1\sigma_x - \frac{i\sqrt{3}}{2} w_1^2 \sigma_z \right] + (w_0^2 - w_1^2) q_1 \cdot \sigma \right\} \psi_5, \\
& [E(E^2 - 1)\sigma_0 + q_1 \cdot \sigma(E^2 - 1 + w_0^2 + 2w_1^2) - E(2(w_0^2 + w_1^2)\sigma_0 - 2w_0w_1\sigma_x)] \psi_1 \\
&= \left\{ E \left[\left(w_0^2 - \frac{w_1^2}{2} \right) \sigma_0 + w_0w_1 \frac{1}{2} (\sigma_x + \sqrt{3}\sigma_y) - \frac{i\sqrt{3}}{2} w_1^2 \sigma_z \right] + (w_0^2 - w_1^2) q_3 \cdot \sigma \right\} \psi_3 \\
&+ \left\{ E \left[\left(w_0^2 - \frac{w_1^2}{2} \right) \sigma_0 + w_0w_1 \frac{1}{2} (\sigma_x - \sqrt{3}\sigma_y) + \frac{i\sqrt{3}}{2} w_1^2 \sigma_z \right] + (w_0^2 - w_1^2) q_2 \cdot \sigma \right\} \psi_5. \tag{E3}
\end{aligned}$$

Plugging in the expressions for the energy E , we can obtain the relations between ψ_i . However, these are messy, and we choose to find the eigenstates on several, simpler, manifolds in the w_0, w_1 parameter space.

2. Eigenstate solution at $\mathbf{k} = 0$ for on the second magic manifold $w_1 = \sqrt{1 + w_0^2}/2$

We first solve for the two zero eigenstates $E_{1,2}(\mathbf{k} = 0, w_0, w_1 = \frac{\sqrt{1+w_0^2}}{2}) = 0$ of Table I. Equation (E2) becomes

$$\begin{aligned}
(3w_0^2 - 1)q_3 \cdot \sigma \psi_5 &= \frac{(3w_0^2 - 1)}{2} (q_1 \cdot \sigma \psi_3 + q_2 \cdot \sigma \psi_1), \\
(3w_0^2 - 1)q_2 \cdot \sigma \psi_3 &= \frac{(3w_0^2 - 1)}{2} (q_3 \cdot \sigma \psi_1 + q_1 \cdot \sigma \psi_5), \\
(3w_0^2 - 1)q_1 \cdot \sigma \psi_1 &= \frac{(3w_0^2 - 1)}{2} (q_3 \cdot \sigma \psi_3 + q_2 \cdot \sigma \psi_5). \tag{E4}
\end{aligned}$$

We now have two cases.

a. Zero energy eigenstate solution at $\mathbf{k} = 0$ for on the second magic manifold $w_1 = \sqrt{1 + w_0^2}/2$, $w_0 \neq 1/\sqrt{3}$

In this case $3w_0^2 - 1 \neq 0$ and Eq. (E4) becomes

$$q_3 \cdot \sigma \psi_5 = \frac{1}{2} (q_1 \cdot \sigma \psi_3 + q_2 \cdot \sigma \psi_1); \quad q_2 \cdot \sigma \psi_3 = \frac{1}{2} (q_3 \cdot \sigma \psi_1 + q_1 \cdot \sigma \psi_5); \quad q_1 \cdot \sigma \psi_1 = \frac{1}{2} (q_3 \cdot \sigma \psi_3 + q_2 \cdot \sigma \psi_5), \tag{E5}$$

with solutions (for the two zero energy eigenstates)

$$\begin{aligned}
\psi_1 &= (q_3 \cdot \sigma)(q_2 \cdot \sigma) \psi_3; \\
\psi_5 &= (q_2 \cdot \sigma)(q_3 \cdot \sigma) \psi_3; \\
\psi_4 &= -q_1 \cdot \sigma [T_3 + T_2(q_2 \cdot \sigma)(q_3 \cdot \sigma)] \psi_3; \\
\psi_2 &= -q_3 \cdot \sigma [T_1 + T_2(q_3 \cdot \sigma)(q_2 \cdot \sigma)] \psi_3; \\
\psi_6 &= -q_2 \cdot \sigma [T_3(q_3 \cdot \sigma)(q_2 \cdot \sigma) + T_1(q_2 \cdot \sigma)(q_3 \cdot \sigma)] \psi_3. \tag{E6}
\end{aligned}$$

The two independent zero energy eigenstates on the second magic manifold can be obtained by taking $\psi_3 = (1, 0)$ and $\psi_3 = (0, 1)$, respectively. However, they are not orthonormal and a further Gram-Schmidt must be performed to orthogonalize them.

We obtain

$$\begin{aligned}
\psi_{E_1=0} & \left(\mathbf{k} = 0, w_0, w_1 = \frac{\sqrt{1+w_0^2}}{2} \right) \\
& = \left(-\frac{i(\sqrt{3}-i)}{2\sqrt{6}\sqrt{w_0^2+1}}, 0, -\frac{\sqrt[6]{-1}}{\sqrt{6}}, \frac{iw_0}{\sqrt{6}\sqrt{w_0^2+1}}, \frac{1}{\sqrt{6}\sqrt{w_0^2+1}}, 0, -\frac{(-1)^{5/6}}{\sqrt{6}}, \right. \\
& \quad \left. -\frac{(-1)^{5/6}w_0}{\sqrt{6}\sqrt{w_0^2+1}}, \frac{i(\sqrt{3}+i)}{2\sqrt{6}\sqrt{w_0^2+1}}, 0, \frac{i}{\sqrt{6}}, -\frac{\sqrt[6]{-1}w_0}{\sqrt{6}\sqrt{w_0^2+1}} \right), \\
\psi_{E_2=0} & \left(\mathbf{k} = 0, w_0, w_1 = \frac{\sqrt{1+w_0^2}}{2} \right) \\
& = \left(\frac{i(\sqrt{3}+i)w_0}{2\sqrt{6}\sqrt{w_0^2+1}}, \frac{i(\sqrt{3}+i)}{2\sqrt{6}}, 0, \frac{(-1)^{5/6}}{\sqrt{6}\sqrt{w_0^2+1}}, \right. \\
& \quad \left. -\frac{\sqrt[3]{-1}w_0}{\sqrt{6}\sqrt{w_0^2+1}}, \frac{1}{\sqrt{6}}, 0, \frac{\sqrt[6]{-1}}{\sqrt{6}\sqrt{w_0^2+1}}, \frac{w_0}{\sqrt{6}\sqrt{w_0^2+1}}, -\frac{i(\sqrt{3}-i)}{2\sqrt{6}}, 0, -\frac{i}{\sqrt{6}\sqrt{w_0^2+1}} \right). \tag{E7}
\end{aligned}$$

b. Nonzero energy eigenstate solutions at $\mathbf{k} = 0$ for on the second magic manifold $w_1 = \sqrt{1+w_0^2}/2$, $w_0 \neq 1/\sqrt{3}$

We can adopt the same strategy to build the other, nonzero energy orthonormal eigenstates. It is tedious (analytic diagonalization programs such as Mathematica fail to provide a result, hence the algebra must be performed by hand) to write the details, but the final answer is, for the eigenstates of energies on the first magic manifold given in Table II:

$$\begin{aligned}
\psi_{E_3} & \left(\mathbf{k} = 0, w_0, w_1 = \frac{\sqrt{1+w_0^2}}{2} \right) \\
& = \frac{1}{4\sqrt{6}\sqrt{(w_0^2+4)(10w_0^2+1)}} [(\sqrt{3}+3i)(\sqrt{3}w_0^2+i\sqrt{10w_0^4+41w_0^2+4}), (\sqrt{3}+3i)(-2\sqrt{10w_0^2+1}+iw_0\sqrt{w_0^2+1}), \\
& \quad -(\sqrt{3}-3i)(2\sqrt{w_0^2+1}+\sqrt{3}w_0\sqrt{w_0^2+4}-iw_0\sqrt{10w_0^2+1}), -2i(\sqrt{3}\sqrt{w_0^2+1}\sqrt{w_0^2+4}+6w_0), 12w_0^2, 0, \\
& \quad -(\sqrt{3}+3i)(-2\sqrt{w_0^2+1}+\sqrt{3}w_0\sqrt{w_0^2+4}+iw_0\sqrt{10w_0^2+1}), (\sqrt{3}-i)(\sqrt{3}\sqrt{w_0^2+1}\sqrt{w_0^2+4}-6w_0), \\
& \quad (\sqrt{3}-3i)(\sqrt{3}w_0^2-i\sqrt{10w_0^4+41w_0^2+4}), -2\sqrt{3}(2\sqrt{10w_0^2+1}-iw_0\sqrt{w_0^2+1}), -12w_0\sqrt{w_0^2+4}, -12(\sqrt{3}+i)w_0], \\
\psi_{E_4} & \left(\mathbf{k} = 0, w_0, w_1 = \frac{\sqrt{1+w_0^2}}{2} \right) \\
& = \frac{1}{4\sqrt{6}\sqrt{(w_0^2+4)(10w_0^2+1)}} [-(\sqrt{3}+i)(2\sqrt{10w_0^2+1}+iw_0\sqrt{w_0^2+1}), -(\sqrt{3}+i)(3\sqrt{3}w_0^2+i\sqrt{10w_0^4+41w_0^2+4}), \\
& \quad 2(\sqrt{w_0^4+5w_0^2+4}-6\sqrt{3}w_0), (\sqrt{3}-i)(-2\sqrt{w_0^2+1}+3\sqrt{3}w_0\sqrt{w_0^2+4}-iw_0\sqrt{10w_0^2+1}), \\
& \quad 4(-1)^{5/6}(2\sqrt{10w_0^2+1}+iw_0\sqrt{w_0^2+1}), 4\sqrt{10w_0^4+41w_0^2+4}, i(\sqrt{3}+i)\sqrt{w_0^4+5w_0^2+4}-6(\sqrt{3}-3i)w_0, \\
& \quad (\sqrt{3}+i)(2\sqrt{w_0^2+1}+3\sqrt{3}w_0\sqrt{w_0^2+4}+iw_0\sqrt{10w_0^2+1}), -2w_0\sqrt{w_0^2+1}+4i\sqrt{10w_0^2+1}, \\
& \quad -(\sqrt{3}-i)(3\sqrt{3}w_0^2-i\sqrt{10w_0^4+41w_0^2+4}), 2(1+i\sqrt{3})\sqrt{w_0^4+5w_0^2+4}, -4w_0\sqrt{10w_0^2+1}+8i\sqrt{w_0^2+1}], \tag{E8}
\end{aligned}$$

$$\begin{aligned}
& \psi_{E_5} \left(\mathbf{k} = 0, w_0, w_1 = \frac{\sqrt{1+w_0^2}}{2} \right) \\
&= \frac{1}{4\sqrt{6}\sqrt{(w_0^2+4)(10w_0^2+1)}} [(\sqrt{3}+3i)(\sqrt{3}w_0^2+i\sqrt{10w_0^4+41w_0^2+4}), (\sqrt{3}+3i)(2\sqrt{10w_0^2+1}+iw_0\sqrt{w_0^2+1}), \\
&(\sqrt{3}-3i)(-2\sqrt{w_0^2+1}+\sqrt{3}w_0\sqrt{w_0^2+4}-iw_0\sqrt{10w_0^2+1}), 2i(\sqrt{3}\sqrt{w_0^2+1}\sqrt{w_0^2+4}-6w_0), 12w_0^2, 0, \\
&(\sqrt{3}+3i)(2\sqrt{w_0^2+1}+\sqrt{3}w_0\sqrt{w_0^2+4}+iw_0\sqrt{10w_0^2+1}), i(\sqrt{3}+3i)\sqrt{w_0^2+1}\sqrt{w_0^2+4}-6(\sqrt{3}-i)w_0, \\
&(\sqrt{3}-3i)(\sqrt{3}w_0^2-i\sqrt{10w_0^4+41w_0^2+4}), 2\sqrt{3}(2\sqrt{10w_0^2+1}+iw_0\sqrt{w_0^2+1}), 12w_0\sqrt{w_0^2+4}, -12(\sqrt{3}+i)w_0], \\
& \psi_{E_6} \left(\mathbf{k} = 0, w_0, w_1 = \frac{\sqrt{1+w_0^2}}{2} \right) \\
&= \frac{1}{4\sqrt{6}\sqrt{(w_0^2+4)(10w_0^2+1)}} [2\sqrt{-1}(2\sqrt{10w_0^2+1}-iw_0\sqrt{w_0^2+1}), -(\sqrt{3}+i)(3\sqrt{3}w_0^2+i\sqrt{10w_0^4+41w_0^2+4}), \\
&-2(\sqrt{w_0^4+5w_0^2+4}+6\sqrt{3}w_0), -(\sqrt{3}-i)(2\sqrt{w_0^2+1}+3\sqrt{3}w_0\sqrt{w_0^2+4}-iw_0\sqrt{10w_0^2+1}), \\
&-4(-1)^{5/6}(2\sqrt{10w_0^2+1}-iw_0\sqrt{w_0^2+1}), 4\sqrt{10w_0^4+41w_0^2+4}, (1-i\sqrt{3})\sqrt{w_0^4+5w_0^2+4}-6(\sqrt{3}-3i)w_0, \\
&-(\sqrt{3}+i)(-2\sqrt{w_0^2+1}+3\sqrt{3}w_0\sqrt{w_0^2+4}+iw_0\sqrt{10w_0^2+1}), -2w_0\sqrt{w_0^2+1}-4i\sqrt{10w_0^2+1}, \\
&-(\sqrt{3}-i)(3\sqrt{3}w_0^2-i\sqrt{10w_0^4+41w_0^2+4}), -2i(\sqrt{3}-i)\sqrt{w_0^4+5w_0^2+4}, 4w_0\sqrt{10w_0^2+1}+8i\sqrt{w_0^2+1}], \quad (E9) \\
& \psi_{E_7} \left(\mathbf{k} = 0, w_0, w_1 = \frac{\sqrt{1+w_0^2}}{2} \right) \\
&= \frac{1}{4\sqrt{6}\sqrt{(w_0^2+4)(10w_0^2+1)}} [(\sqrt{3}+3i)(\sqrt{3}w_0^2-i\sqrt{10w_0^4+41w_0^2+4}), (\sqrt{3}+3i)(2\sqrt{10w_0^2+1}+iw_0\sqrt{w_0^2+1}), \\
&-(\sqrt{3}-3i)(2\sqrt{w_0^2+1}+\sqrt{3}w_0\sqrt{w_0^2+4}+iw_0\sqrt{10w_0^2+1}), -2i(\sqrt{3}\sqrt{w_0^2+1}\sqrt{w_0^2+4}+6w_0), 12w_0^2, 0, \\
&-(\sqrt{3}+3i)(-2\sqrt{w_0^2+1}+\sqrt{3}w_0\sqrt{w_0^2+4}-iw_0\sqrt{10w_0^2+1}), (\sqrt{3}-i)(\sqrt{3}\sqrt{w_0^2+1}\sqrt{w_0^2+4}-6w_0), \\
&(\sqrt{3}-3i)(\sqrt{3}w_0^2+i\sqrt{10w_0^4+41w_0^2+4}), 2\sqrt{3}(2\sqrt{10w_0^2+1}+iw_0\sqrt{w_0^2+1}), -12w_0\sqrt{w_0^2+4}, -12(\sqrt{3}+i)w_0], \\
& \psi_{E_8} \left(\mathbf{k} = 0, w_0, w_1 = \frac{\sqrt{1+w_0^2}}{2} \right) \\
&= \frac{1}{4\sqrt{6}\sqrt{(w_0^2+4)(10w_0^2+1)}} [-(\sqrt{3}+i)(2\sqrt{10w_0^2+1}-iw_0\sqrt{w_0^2+1}), (\sqrt{3}+i)(3\sqrt{3}w_0^2-i\sqrt{10w_0^4+41w_0^2+4}), \\
&-2(\sqrt{w_0^4+5w_0^2+4}-6\sqrt{3}w_0), -(\sqrt{3}-i)(-2\sqrt{w_0^2+1}+3\sqrt{3}w_0\sqrt{w_0^2+4}+iw_0\sqrt{10w_0^2+1}), \\
&-2(\sqrt{3}-i)(2\sqrt{10w_0^2+1}-iw_0\sqrt{w_0^2+1}), 4\sqrt{10w_0^4+41w_0^2+4}, (1-i\sqrt{3})\sqrt{w_0^4+5w_0^2+4}+6(\sqrt{3}-3i)w_0, \\
&-(\sqrt{3}+i)(2\sqrt{w_0^2+1}+3\sqrt{3}w_0\sqrt{w_0^2+4}-iw_0\sqrt{10w_0^2+1}), 2w_0\sqrt{w_0^2+1}+4i\sqrt{10w_0^2+1}, \\
&(\sqrt{3}-i)(3\sqrt{3}w_0^2+i\sqrt{10w_0^4+41w_0^2+4}), -2i(\sqrt{3}-i)\sqrt{w_0^4+5w_0^2+4}, -4w_0\sqrt{10w_0^2+1}-8i\sqrt{w_0^2+1}], \quad (E10)
\end{aligned}$$

$$\begin{aligned}
& \psi_{E_9} \left(\mathbf{k} = 0, w_0, w_1 = \frac{\sqrt{1+w_0^2}}{2} \right) \\
&= \frac{1}{4\sqrt{6}\sqrt{(w_0^2+4)(10w_0^2+1)}} [(\sqrt{3}+3i)(\sqrt{3}w_0^2 - i\sqrt{10w_0^4+41w_0^2+4}), -(\sqrt{3}+3i)(2\sqrt{10w_0^2+1} - iw_0\sqrt{w_0^2+1}), \\
&(\sqrt{3}-3i)(-2\sqrt{w_0^2+1} + \sqrt{3}w_0\sqrt{w_0^2+4} + iw_0\sqrt{10w_0^2+1}), 2i(\sqrt{3}\sqrt{w_0^2+1}\sqrt{w_0^2+4} - 6w_0), 12w_0^2, 0, \\
&(\sqrt{3}+3i)(2\sqrt{w_0^2+1} + \sqrt{3}w_0\sqrt{w_0^2+4} - iw_0\sqrt{10w_0^2+1}), -(\sqrt{3}-i)(\sqrt{3}\sqrt{w_0^2+1}\sqrt{w_0^2+4} + 6w_0), \\
&(\sqrt{3}-3i)(\sqrt{3}w_0^2 + i\sqrt{10w_0^4+41w_0^2+4}), -2\sqrt{3}(2\sqrt{10w_0^2+1} - iw_0\sqrt{w_0^2+1}), 12w_0\sqrt{w_0^2+4}, -12(\sqrt{3}+i)w_0], \\
& \psi_{E_{10}} \left(\mathbf{k} = 0, w_0, w_1 = \frac{\sqrt{1+w_0^2}}{2} \right) \\
&= \frac{1}{4\sqrt{6}\sqrt{(w_0^2+4)(10w_0^2+1)}} [(\sqrt{3}+i)(2\sqrt{10w_0^2+1} + iw_0\sqrt{w_0^2+1}), (\sqrt{3}+i)(3\sqrt{3}w_0^2 - i\sqrt{10w_0^4+41w_0^2+4}), \\
&2(\sqrt{w_0^4+5w_0^2+4} + 6\sqrt{3}w_0), (\sqrt{3}-i)(2\sqrt{w_0^2+1} + 3\sqrt{3}w_0\sqrt{w_0^2+4} + iw_0\sqrt{10w_0^2+1}), \\
&4\sqrt{-1}(w_0\sqrt{w_0^2+1} - 2i\sqrt{10w_0^2+1}), 4\sqrt{10w_0^4+41w_0^2+4}, i(\sqrt{3}+i)\sqrt{w_0^4+5w_0^2+4} + 6(\sqrt{3}-3i)w_0, \\
&(\sqrt{3}+i)(-2\sqrt{w_0^2+1} + 3\sqrt{3}w_0\sqrt{w_0^2+4} - iw_0\sqrt{10w_0^2+1}), 2w_0\sqrt{w_0^2+1} - 4i\sqrt{10w_0^2+1}, \\
&(\sqrt{3}-i)(3\sqrt{3}w_0^2 + i\sqrt{10w_0^4+41w_0^2+4}), 2(1+i\sqrt{3})\sqrt{w_0^4+5w_0^2+4}, 4w_0\sqrt{10w_0^2+1} - 8i\sqrt{w_0^2+1}], \tag{E11}
\end{aligned}$$

$$\begin{aligned}
& \psi_{E_{11}} \left(\mathbf{k} = 0, w_0, w_1 = \frac{\sqrt{1+w_0^2}}{2} \right) \\
&= \left[\frac{(\sqrt{3}-3i)(w_0+i)}{12\sqrt{w_0^2+1}}, \frac{1}{12}(-\sqrt{3}+3i), -\frac{1}{2\sqrt{3}}, -\frac{\sqrt{-1}(w_0+i)}{2\sqrt{3}\sqrt{w_0^2+1}}, \frac{(\sqrt{3}+3i)(w_0+i)}{12\sqrt{w_0^2+1}}, \frac{1}{2\sqrt{3}}, \right. \\
&\left. \frac{1}{12}(\sqrt{3}-3i), -\frac{(\sqrt{3}-3i)(w_0+i)}{12\sqrt{w_0^2+1}}, -\frac{w_0+i}{2\sqrt{3}\sqrt{w_0^2+1}}, \frac{1}{12}(-\sqrt{3}-3i), \frac{1}{12}(\sqrt{3}+3i), \frac{w_0+i}{2\sqrt{3}\sqrt{w_0^2+1}} \right], \tag{E12}
\end{aligned}$$

$$\begin{aligned}
& \psi_{E_{12}} \left(\mathbf{k} = 0, w_0, w_1 = \frac{\sqrt{1+w_0^2}}{2} \right) \\
&= \left[\frac{(\sqrt{3}-3i)(w_0-i)}{12\sqrt{w_0^2+1}}, \frac{1}{12}(-\sqrt{3}+3i), \frac{1}{2\sqrt{3}}, \frac{(\sqrt{3}+3i)(w_0-i)}{12\sqrt{w_0^2+1}}, \frac{(\sqrt{3}+3i)(w_0-i)}{12\sqrt{w_0^2+1}}, \frac{1}{2\sqrt{3}}, \right. \\
&\left. \frac{1}{12}(-\sqrt{3}+3i), \frac{(\sqrt{3}-3i)(w_0-i)}{12\sqrt{w_0^2+1}}, -\frac{w_0-i}{2\sqrt{3}\sqrt{w_0^2+1}}, \frac{1}{12}(-\sqrt{3}-3i), \frac{1}{12}(-\sqrt{3}-3i), -\frac{w_0-i}{2\sqrt{3}\sqrt{w_0^2+1}} \right]. \tag{E13}
\end{aligned}$$

c. Zero energy eigenstate solution at $\mathbf{k} = 0$ for on the second magic manifold $w_1 = \sqrt{1+w_0^2}/2 = w_0 = 1/\sqrt{3}$

There are six zero energies in Table I at this point $w_1 = \sqrt{1+w_0^2}/2 = w_0 = 1/\sqrt{3}$. They have already been given in Appendix C.

APPENDIX F: PERTURBATION THEORY FOR $H_{mm'}^{(1)}(\mathbf{k}, \mathbf{w}_0) = 0, E_m = 0$ MANIFOLD

1. Review of perturbation theory

We review the perturbation theory being performed in the main text. This formalism was first presented in Ref. [123], but we go to higher order in current perturbation theory. We have a Hamiltonian H^0 whose eigenstates we know, and is hence purely diagonal in its eigenstate basis. We also have a perturbation Hamiltonian H' , with both diagonal and off-diagonal elements. Among the eigenstates of H^0 we have a set of eigenstates separated by a large gap from the others, which cannot be closed by the addition of H' , and they represent the manifold we want to project in. These states are indexed by m, m', m'', m''', \dots while the rest of the eigenstates are indexed by l, l', l'', l''', \dots . These two form separate subspaces. We now want to find a Hamiltonian $H_{mm'}$ which incorporates the effects of H' up to any desired order. We separate H' into a diagonal part H_1 plus an off-diagonal part H_2 between these manifolds:

$$H' = H_1 + H_2,$$

$$(H_1)_{mm'} = \langle \psi_m | H' | \psi_{m'} \rangle; \quad (H_1)_{ll'} = \langle \psi_l | H' | \psi_{l'} \rangle; \quad (H_2)_{ml} = \langle \psi_m | H' | \psi_l \rangle; \quad (H_2)_{mm'} = (H_2)_{ll'} = (H_1)_{ml} = 0. \quad (\text{F1})$$

We also have

$$H|\psi_m\rangle = E_m|\psi_m\rangle, \quad H|\psi_l\rangle = E_l|\psi_l\rangle. \quad (\text{F2})$$

We look for a unitary transformation:

$$\tilde{H} = e^{-S}(H^0 + H')e^S, \quad (\text{F3})$$

where $S(= -S^\dagger)$ has only matrix elements that are off-diagonal between the subspaces, i.e., $S_{ml} = 0$. The unitary transformation is chosen such that the *off-diagonal* part of \tilde{H} is zero to the desired order ($H_{ml} = 0$). Since we know S, H_2 are off-diagonal and H_1 is diagonal, we find that S can be obtained from the condition

$$\tilde{H}_{\text{off-diagonal}} = \sum_{j=0}^{\infty} \frac{1}{(2j+1)!} [H^0 + H_1, S]^{2j+1} + \sum_{j=0}^{\infty} \frac{1}{(2j)!} [H_2, S]^{2j} = 0 \quad (\text{F4})$$

(the off-diagonal Hamiltonian is zero). Once S is found, the diagonal Hamiltonian is

$$\tilde{H}_{\text{diagonal}} = \sum_{j=0}^{\infty} \frac{1}{(2j)!} [H^0 + H_1, S]^{2j} + \sum_{j=0}^{\infty} \frac{1}{(2j+1)!} [H_2, S]^{2j+1}, \quad (\text{F5})$$

where $[A, B]^j = [[[[[A, B], B], B], \dots], B]$ where the number of B 's is equal to j . We then parametrize $S = S_1 + S_2 + S_3 + \dots$, where S_n is order n in perturbation theory, i.e., in H' (or equivalently, in H_1 or H_2).

The terms up to order 4 are derived in Winkler's book [123], and for our simplified problem, they are presented in the main text. We have numerically checked their correctness. We here also present the fifth order term: this term is tedious, but we use a particularly nice property of our eigenstate space that $(H_1)_{mm'} = \langle \psi_m | H' | \psi_{m'} \rangle = 0, E_m = 0$ for $m = 1, 2$ property is true only for $H' = I_{6 \times 6} \otimes \mathbf{k} \cdot \boldsymbol{\sigma}$ and for the zero energy eigenstates $\psi_m, m = 1, 2$ of $H_0 = H_{\text{Hex}}(\mathbf{k} = 0, \mathbf{w}_0, \mathbf{w}_1 = \sqrt{1 + \mathbf{w}_0^2}/2)$. To the desired order, we find

$$\begin{aligned} (S_1)_{ml} &= \frac{H'_{ml}}{E_l}, \quad (S_1)_{lm} = -\frac{H'_{lm}}{E_l}, \\ (S_2)_{ml} &= -\sum_{l'} \frac{H'_{ml'} H'_{l'l}}{E_l E_{l'}}, \quad (S_2)_{lm} = \sum_{l'} \frac{H'_{ll'} H'_{l'm}}{E_l E_{l'}}, \\ (S_3)_{ml} &= \sum_{l', l''} \frac{H'_{ml'} H'_{l'l''} H'_{l''l}}{E_l E_{l'} E_{l''}} - \frac{1}{3} \sum_{l'm'} H'_{ml'} H'_{l'm'} H'_{m'l} \left(\frac{3}{E_l^2 E_{l'}} + \frac{1}{E_{l'}^2 E_l} \right), \\ (S_3)_{lm} &= -\sum_{l', l''} \frac{H'_{ll'} H'_{l'l''} H'_{l''m}}{E_l E_{l'} E_{l''}} + \frac{1}{3} \sum_{l'm'} H'_{l'm'} H'_{m'l'} H'_{l'm} \left(\frac{3}{E_l^2 E_{l'}} + \frac{1}{E_{l'}^2 E_l} \right). \end{aligned} \quad (\text{F6})$$

Due to our property $(H_1)_{mm'} = \langle \psi_m | H' | \psi_{m'} \rangle = 0, E_m = 0$ on the second magic manifold, we find that the fourth order S_4 is not needed in order to obtain the fifth order diagonal Hamiltonian, as terms in the expression of the Hamiltonian that contain it cancel. We find that the fifth order Hamiltonian is

$$\begin{aligned} \tilde{H}_{\text{diagonal}}^{(5)} &= -S_2 H^0 S_3 - S_3 H^0 S_2 - S_1 H_1 S_3 - S_3 H_1 S_1 - S_2 H_2 S_2 \\ &\quad - \frac{1}{6} (S_1 H^0 S_1 S_2 S_1 + S_1 H^0 S_2 S_1^2 + S_1 H^0 S_1^2 S_2 + S_2 H^0 S_1^3 + S_1 H_1 S_1^3 \\ &\quad + S_1 S_2 S_1 H^0 S_1 + S_2 S_1^2 H^0 S_1 + S_1^2 S_2 H^0 S_1 + S_1^3 H^0 S_2 + S_1^3 H_1 S_1) \end{aligned}$$

$$\begin{aligned}
 & + \frac{1}{6} [H_2 S_2 S_1^2 + H_2 S_1^2 S_2 + H_2 S_1 S_2 S_1 + 3(S_1 S_2 H_2 S_1 + S_2 S_1 H_2 S_1 + S_1^2 H_2 S_2) \\
 & - (S_2 S_1^2 H_2 + S_1^2 S_2 H_2 + S_1 S_2 S_1 H_2) - 3(S_1 H_2 S_1 S_2 + S_1 H_2 S_2 S_1 + S_2 H_2 S_1^2)].
 \end{aligned} \quad (F7)$$

The matrix elements of these terms give

$$\begin{aligned}
 & \frac{1}{6} [H_2 S_2 S_1^2 + H_2 S_1^2 S_2 + H_2 S_1 S_2 S_1 - (S_2 S_1^2 H_2 + S_1^2 S_2 H_2 + S_1 S_2 S_1 H_2)]_{mm'} \\
 & = -\frac{1}{6} \sum_{l,l',l''} \sum_{m''} \frac{H'_{ml} H'_{l'l''} H'_{l'm''} H_{m''l''} H_{l''m'} + H_{m'l''} H_{l''m''} H_{m''l'} H_{l'l} H_{lm}}{E_l E_{l'} E_{l''}} \left(\frac{1}{E_l} + \frac{1}{E_{l'}} + \frac{1}{E_{l''}} \right),
 \end{aligned} \quad (F8)$$

$$\begin{aligned}
 & \frac{1}{6} [3(S_1 S_2 H_2 S_1 + S_2 S_1 H_2 S_1 + S_1^2 H_2 S_2) - 3(S_1 H_2 S_1 S_2 + S_1 H_2 S_2 S_1 + S_2 H_2 S_1^2)]_{mm'} \\
 & = -\frac{1}{2} \sum_{l,l',l''} \sum_{m''} \frac{H'_{ml} H'_{l'l''} H'_{l'm''} H_{m''l''} H_{l''m'} + H_{m'l''} H_{l''m''} H_{m''l'} H_{l'l} H_{lm}}{E_l E_{l'} E_{l''}} \left(\frac{1}{E_l} + \frac{1}{E_{l'}} + \frac{1}{E_{l''}} \right),
 \end{aligned} \quad (F9)$$

$$\begin{aligned}
 & -\frac{1}{6} (S_1 H^0 S_1 S_2 S_1 + S_1 H^0 S_2 S_1^2 + S_1 H^0 S_1^2 S_2 + S_2 H^0 S_1^3 + S_1 H_1 S_1^3 \\
 & + S_1 S_2 S_1 H^0 S_1 + S_2 S_1^2 H^0 S_1 + S_1^2 S_2 H^0 S_1 + S_1^3 H^0 S_2 + S_1^3 H_1 S_1) \\
 & = \frac{1}{6} \sum_{l,l',l''} \sum_{m''} \frac{H'_{ml} H'_{l'l''} H'_{l'm''} H_{m''l''} H_{l''m'} + H_{m'l''} H_{l''m''} H_{m''l'} H_{l'l} H_{lm}}{E_l E_{l'} E_{l''}} \left(\frac{1}{E_l} + \frac{1}{E_{l'}} + \frac{1}{E_{l''}} \right), \\
 & (-S_2 H^0 S_3 - S_3 H^0 S_2 - S_1 H_1 S_3 - S_3 H_1 S_1 - S_2 H_2 S_2)_{mm'} = \sum_{l,l',l'',l'''} \frac{H'_{ml} H'_{l'l''} H'_{l''l'''} H_{l''l'''} H_{l''m'}}{E_l E_{l'} E_{l''} E_{l'''}}.
 \end{aligned} \quad (F10)$$

Hence

$$\tilde{H}_{\text{diagonal}}^{(5)} = \sum_{l,l',l'',l'''} \frac{H'_{ml} H'_{l'l''} H'_{l''l'''} H_{l''l'''} H_{l''m'}}{E_l E_{l'} E_{l''} E_{l'''}} - \frac{1}{2} \sum_{l,l',l''} \sum_{m''} \frac{H'_{ml} H'_{l'l''} H'_{l'm''} H_{m''l''} H_{l''m'} + H_{m'l''} H_{l''m''} H_{m''l'} H_{l'l} H_{lm}}{E_l E_{l'} E_{l''}} \left(\frac{1}{E_l} + \frac{1}{E_{l'}} + \frac{1}{E_{l''}} \right). \quad (F11)$$

2. Calculations of the Hamiltonian matrix elements when first order vanishes

Here we calculate explicitly the perturbations of $H_{\text{perturb}}(\mathbf{k}, w_0) = I_{6 \times 6} \otimes \mathbf{k} \cdot \vec{\sigma}$ in Eq. (47) up to fifth order.

a. First order

The first order perturbation can be easily seen to be zero:

$$H_{mm'}^{(1)}(\mathbf{k}, w_0) = \langle \psi_m | H_{\text{perturb}}(\mathbf{k}, w_0) | \psi_{m'} \rangle = 0. \quad (F12)$$

b. Second order

$$H_{mm'}^{(2)}(\mathbf{k}, w_0) = - \sum_{l=3 \dots 12} \frac{1}{E_l} \langle \psi_m | H_{\text{perturb}}(\mathbf{k}, w_0) | \psi_l \rangle \langle \psi_l | H_{\text{perturb}}(\mathbf{k}, w_0) | \psi_{m'} \rangle = \boxed{-\frac{4w_0^2(k_x^2 + k_y^2)}{3\sqrt{w_0^2 + 1}(3w_0^2 - 1)}(\sigma_y + \sqrt{3}\sigma_x)}. \quad (F13)$$

c. Third order

$$\begin{aligned}
 H_{mm'}^{(3)}(\mathbf{k}, w_0) & = \sum_{l,l'=3 \dots 12} \frac{1}{E_l E_{l'}} \langle \psi_m | H_{\text{perturb}}(\mathbf{k}, w_0) | \psi_l \rangle \langle \psi_l | H_{\text{perturb}}(\mathbf{k}, w_0) | \psi_{l'} \rangle \langle \psi_{l'} | H_{\text{perturb}}(\mathbf{k}, w_0) | \psi_{m'} \rangle \\
 & = \boxed{\frac{4k_x w_0 (w_0^2 - 3)(k_x^2 - 3k_y^2)}{9(1 - 3w_0^2)^2 \sqrt{w_0^2 + 1}} \sigma_0}.
 \end{aligned} \quad (F14)$$

d. Fourth order

For the fourth order, there are two terms: First,

$$\begin{aligned}
 H_{mm'}^{(4_1)}(\mathbf{k}, w_0) &= - \sum_{l, l', l''=3, \dots, 12} \frac{1}{E_l E_{l'} E_{l''}} \langle \psi_m | H_{\text{perturb}}(\mathbf{k}, w_0) | \psi_l \rangle \langle \psi_l | H_{\text{perturb}}(\mathbf{k}, w_0) | \psi_{l'} \rangle \langle \psi_{l'} | H_{\text{perturb}}(\mathbf{k}, w_0) | \psi_{l''} \rangle \\
 &\quad \times \langle \psi_{l''} | H_{\text{perturb}}(\mathbf{k}, w_0) | \psi_{m'} \rangle \\
 &= \frac{8w_0^2(w_0^4 + 16w_0^2 - 9)(k_x^2 + k_y^2)^2}{27(w_0^2 + 1)^{3/2}(3w_0^2 - 1)^3} (\sigma_y + \sqrt{3}\sigma_x).
 \end{aligned} \tag{F15}$$

Second,

$$\begin{aligned}
 H_{mm'}^{(4_2)}(\mathbf{k}, w_0) &= \sum_{l, l'=3, \dots, 12} \sum_{m''=1, 2} \frac{1}{E_l E_{l'}} \left(\frac{1}{E_l} + \frac{1}{E_{l'}} \right) \\
 &\quad \times \langle \psi_m | H_{\text{perturb}}(\mathbf{k}, w_0) | \psi_l \rangle \langle \psi_l | H_{\text{perturb}}(\mathbf{k}, w_0) | \psi_{m''} \rangle \langle \psi_{m''} | H_{\text{perturb}}(\mathbf{k}, w_0) | \psi_{l'} \rangle \langle \psi_{l'} | H_{\text{perturb}}(\mathbf{k}, w_0) | \psi_{m'} \rangle \\
 &= \frac{16w_0^2(17w_0^2 + 9)(k_x^2 + k_y^2)^2}{27\sqrt{w_0^2 + 1}(3w_0^2 - 1)^3} (\sigma_y + \sqrt{3}\sigma_x).
 \end{aligned} \tag{F16}$$

Notice that so far, the eigenstates are not \mathbf{k} dependent, they are just the eigenstates of $(\sigma_y + \sqrt{3}\sigma_x)$.

e. Fifth order

The fifth order perturbation theory is not available in any book. Hence we derived it in Appendix F, for the special case for which the manifold m of states we project in has the first order Hamiltonian $H_{mm'}^{(1)}(\mathbf{k}, w_0) = 0$ and for which its energies are $E_m = 0$.

The fifth order also has two terms, just like the fourth order (see Appendix F). We find

$$\sum_{l, l', l'', l'''} \frac{H'_{ml} H'_{l'l''} H'_{l''l'''} H_{l''m'}}{E_l E_{l'} E_{l''} E_{l'''}} = \frac{32k_x(w_0^2 - 3)^2(2w_0^2 - 1)w_0(k_x^2 - 3k_y^2)(k_x^2 + k_y^2)}{81(w_0^2 + 1)^{3/2}(3w_0^2 - 1)^4} \sigma_0 \tag{F17}$$

and

$$\begin{aligned}
 & - \frac{1}{2} \sum_{l, l', l''} \sum_{m''} \frac{(H'_{ml} H'_{l'l''} H_{l''m''} H_{m''l'} + H_{m''l''} H_{l''m''} H_{m''l'} H_{l'l} H_{lm})}{E_l E_{l'} E_{l''}} \left(\frac{1}{E_l} + \frac{1}{E_{l'}} + \frac{1}{E_{l''}} \right) \\
 &= \frac{16k_x(11w_0^4 - 94w_0^2 - 9)w_0(k_x^2 - 3k_y^2)(k_x^2 + k_y^2)}{27(\sqrt{w_0^2 + 1}(3w_0^2 - 1)^4)} \sigma_0.
 \end{aligned} \tag{F18}$$

We can clearly see the structure of the order n Hamiltonian, as a perturbation in $1/(3w_0^2 - 1)^{n-1}$, with symmetry-preserving functions of \mathbf{k} . The full two-band approximation to the hexagon Hamiltonian is, up to fifth order, is

$$\begin{aligned}
 H_{2\text{band}}^{\text{Hex}} \left(\mathbf{k}, w_0, w_1 = \frac{\sqrt{1 + w_0^2}}{2} \right) &= \frac{4w_0^2}{3\sqrt{w_0^2 + 1}(3w_0^2 - 1)} \left[-1 + \frac{2(35w_0^4 + 68w_0^2 + 9)(k_x^2 + k_y^2)}{9(w_0^2 + 1)(3w_0^2 - 1)^2} \right] (k_x^2 + k_y^2) (\sigma_y + \sqrt{3}\sigma_x) \\
 &+ \frac{4w_0}{9\sqrt{w_0^2 + 1}(1 - 3w_0^2)^2} \left[(w_0^2 - 3) - \frac{4(29w_0^6 - 223w_0^4 - 357w_0^2 - 9)}{9(1 - 3w_0^2)^2(w_0^2 + 1)} (k_x^2 + k_y^2) \right] k_x (k_x^2 - 3k_y^2) \sigma_0
 \end{aligned} \tag{F19}$$

better expressed as

$$H_{2\text{band}}^{\text{Hex}} \left(\mathbf{k}, w_0, w_1 = \frac{\sqrt{1 + w_0^2}}{2} \right) = d_0(\mathbf{k}, w_0) \sigma_0 + d_1(\mathbf{k}, w_0) (\sigma_y + \sqrt{3}\sigma_x), \tag{F20}$$

where

$$d_0(\mathbf{k}, w_0) = \frac{4w_0}{9\sqrt{w_0^2 + 1}(1 - 3w_0^2)^2} \left[(w_0^2 - 3) - \frac{4(29w_0^6 - 223w_0^4 - 357w_0^2 - 9)}{9(1 - 3w_0^2)^2(w_0^2 + 1)} (k_x^2 + k_y^2) \right] k_x (k_x^2 - 3k_y^2) \quad (\text{F21})$$

and

$$d_1 \left(\mathbf{k}, w_0 = \frac{\sqrt{1 + w_0^2}}{2} \right) = \frac{4w_0^2}{3\sqrt{w_0^2 + 1}(3w_0^2 - 1)} \left[-1 + \frac{2(35w_0^4 + 68w_0^2 + 9)(k_x^2 + k_y^2)}{9(w_0^2 + 1)(3w_0^2 - 1)^2} \right] (k_x^2 + k_y^2). \quad (\text{F22})$$

3. Calculations of the Hamiltonian matrix elements when first order does not vanish

We take the unperturbed Hamiltonian to be $H_{\text{Hex}}(\mathbf{k} = 0, w_0, w_1 = \sqrt{1 + w_0^2}/2)$ (the hexagon model on the second magic manifold) in Eq. (40). For this Hamiltonian we are able to obtain *all the eigenstates analytically* in Appendix E 2. The perturbation Hamiltonian, away from the second magic manifold, is

$$\begin{aligned} H_{\text{perturb}}(\mathbf{k}, w_0, w_1) &= H_{\text{Hex}}(\mathbf{k}, w_0, w_1) - H_{\text{Hex}} \left(\mathbf{k} = 0, w_0, w_1 = \frac{\sqrt{1 + w_0^2}}{2} \right) \\ &= I_{6 \times 6} \otimes \mathbf{k} \cdot \vec{\sigma} + H_{\text{Hex}} \left(\mathbf{k} = 0, 0, w_1 = \frac{\sqrt{1 + w_0^2}}{2} \right). \end{aligned} \quad (\text{F23})$$

a. First order

$$H_{mm'}^{(1)}(\mathbf{k}, w_0, w_1) = \langle \psi_m | H_{\text{perturb}}(\mathbf{k}, w_0, w_1) | \psi_{m'} \rangle = \boxed{\left(\frac{\sqrt{w_0^2 + 1}}{2} - w_1 \right) (\sigma_y + \sqrt{3}\sigma_x)}. \quad (\text{F24})$$

Hence there is now a linear term in the Hamiltonian. Because of this, many other terms in the further degree perturbation theory become nonzero.

b. Second order

$$\begin{aligned} H_{mm'}^{(2)}(\mathbf{k}, w_0, w_1) &= - \sum_{l=3, \dots, 12} \frac{1}{E_l} \langle \psi_m | H_{\text{perturb}}(\mathbf{k}, w_0) | \psi_l \rangle \langle \psi_l | H_{\text{perturb}}(\mathbf{k}, w_0) | \psi_{m'} \rangle \\ &= \boxed{- \frac{4w_0^2(k_x^2 + k_y^2)}{3\sqrt{w_0^2 + 1}(3w_0^2 - 1)} (\sigma_y + \sqrt{3}\sigma_x)}. \end{aligned} \quad (\text{F25})$$

The second order perturbation theory is unchanged!

c. Third order

There are now two third order terms, as the first order perturbation terms do not vanish. First,

$$\begin{aligned} H_{mm'}^{(3_1)}(\mathbf{k}, w_0, w_1) &= \sum_{l, l'=3, \dots, 12} \frac{1}{E_l E_{l'}} \langle \psi_m | H_{\text{perturb}}(\mathbf{k}, w_0) | \psi_l \rangle \langle \psi_l | H_{\text{perturb}}(\mathbf{k}, w_0) | \psi_{l'} \rangle \langle \psi_{l'} | H_{\text{perturb}}(\mathbf{k}, w_0) | \psi_{m'} \rangle \\ &= \boxed{\frac{4k_x w_0 (w_0^2 - 3)(k_x^2 - 3k_y^2)}{9(1 - 3w_0^2)^2 \sqrt{w_0^2 + 1}} \sigma_0 - \frac{8w_0^2(k_x^2 + k_y^2)(\sqrt{w_0^2 + 1} - 2w_1)}{9(1 - 3w_0^2)^2} (\sigma_y + \sqrt{3}\sigma_x)}. \end{aligned} \quad (\text{F26})$$

Second,

$$\begin{aligned}
 H_{mm'}^{(3_2)}(\mathbf{k}, w_0, w_1) &= -\frac{1}{2} \sum_{l=3\dots 12} \sum_{m''=1,2} \frac{\langle \psi_m | H_{\text{perturb}}(\mathbf{k}, w_0, w_1) | \psi_l \rangle \langle \psi_l | H_{\text{perturb}}(\mathbf{k}, w_0, w_1) | \psi_{m''} \rangle \langle \psi_{m''} | H_{\text{perturb}}(\mathbf{k}, w_0, w_1) | \psi_{m'} \rangle + \text{H.c.}}{E_l^2} \\
 &= -\frac{2(17w_0^2 + 9)(k_x^2 + k_y^2)(\sqrt{w_0^2 + 1} - 2w_1)}{9(1 - 3w_0^2)^2} (\sigma_y + \sqrt{3}\sigma_x)
 \end{aligned} \tag{F27}$$

(where H.c. is the Hermitian conjugate).

The total third order Hamiltonian then reads

$$\frac{4k_x w_0 (w_0^2 - 3)(k_x^2 - 3k_y^2)}{9(1 - 3w_0^2)^2 \sqrt{w_0^2 + 1}} \sigma_0 - \frac{2(7w_0^2 + 3)(k_x^2 + k_y^2)(\sqrt{w_0^2 + 1} - 2w_1)}{3(1 - 3w_0^2)^2} (\sigma_y + \sqrt{3}\sigma_x). \tag{F28}$$

d. Fourth order

For the fourth order, there are now four terms: First,

$$\begin{aligned}
 H_{mm'}^{(4_1)}(\mathbf{k}, w_0, w_1) &= - \sum_{l,l',l''=3,\dots,12} \frac{1}{E_l E_{l'} E_{l''}} \langle \psi_m | H_{\text{perturb}}(\mathbf{k}, w_0, w_1) | \psi_l \rangle \langle \psi_l | H_{\text{perturb}}(\mathbf{k}, w_0) | \psi_{l'} \rangle \\
 &\quad \times \langle \psi_{l'} | H_{\text{perturb}}(\mathbf{k}, w_0, w_1) | \psi_{l''} \rangle \langle \psi_{l''} | H_{\text{perturb}}(\mathbf{k}, w_0, w_1) | \psi_{m'} \rangle \\
 &= \frac{8w_0(7w_0^2 + 3)k_x(k_x^2 - 3k_y^2)(2w_1 - \sqrt{w_0^2 + 1})}{27(3w_0^2 - 1)^3} \sigma_0 \\
 &\quad + \frac{4w_0^2(k_x^2 + k_y^2)[2(w_0^4 + 16w_0^2 - 9)(k_x^2 + k_y^2) + (w_0^2 + 1)(5w_0^2 - 7)(2w_1 - \sqrt{w_0^2 + 1})^2]}{27(w_0^2 + 1)^{3/2}(3w_0^2 - 1)^3} (\sigma_y + \sqrt{3}\sigma_x).
 \end{aligned} \tag{F29}$$

Second,

$$\begin{aligned}
 H_{mm'}^{(4_2)}(\mathbf{k}, w_0) &= \sum_{l,l'=3,\dots,12} \sum_{m''=1,2} \frac{1}{E_l E_{l'}} \left(\frac{1}{E_l} + \frac{1}{E_{l'}} \right) \langle \psi_m | H_{\text{perturb}}(\mathbf{k}, w_0, w_1) | \psi_l \rangle \langle \psi_l | H_{\text{perturb}}(\mathbf{k}, w_0) | \psi_{m''} \rangle \\
 &\quad \times \langle \psi_{m''} | H_{\text{perturb}}(\mathbf{k}, w_0, w_1) | \psi_{l'} \rangle \langle \psi_{l'} | H_{\text{perturb}}(\mathbf{k}, w_0, w_1) | \psi_{m'} \rangle \\
 &= \frac{16w_0^2(17w_0^2 + 9)(k_x^2 + k_y^2)^2}{27\sqrt{w_0^2 + 1}(3w_0^2 - 1)^3} (\sigma_y + \sqrt{3}\sigma_x).
 \end{aligned} \tag{F30}$$

Third, we have, adopting the notation $\langle \psi_m | H_{\text{perturb}}(\mathbf{k}, w_0) | \psi_l \rangle = H'_{ml}$, etc.,

$$\begin{aligned}
 H_{mm'}^{(4_3)}(\mathbf{k}, w_0, w_1) &= -\frac{1}{2} \sum_{l,m'',m'''} \frac{1}{E_l^3} (H'_{mm''} H'_{m''m'''} H'_{m'''} H'_{l m'} + H'_{ml} H'_{l m''} H'_{m''m'''} H'_{m'''} m') \\
 &= \frac{8w_0^2(35w_0^2 + 23)(k_x^2 + k_y^2)(\sqrt{w_0^2 + 1} - 2w_1)^2}{27\sqrt{w_0^2 + 1}(3w_0^2 - 1)^3} (\sigma_y + \sqrt{3}\sigma_x),
 \end{aligned} \tag{F31}$$

$$\begin{aligned}
 H_{mm'}^{(4_4)}(\mathbf{k}, w_0, w_1) &= \frac{1}{2} \sum_{l,l',m''} \frac{1}{E_l E_{l'}} \left(\frac{1}{E_l} + \frac{1}{E_{l'}} \right) (H'_{ml} H'_{l l'} H'_{l' m''} H'_{m'' m'} + H'_{mm''} H'_{m'' l'} H'_{l' l} H'_{l m'}) \\
 &= \frac{32k_x w_0 (w_0^2 - 15)(k_x^2 - 3k_y^2)(\sqrt{w_0^2 + 1} - 2w_1)}{27(3w_0^2 - 1)^3} \sigma_0 \\
 &\quad + \frac{4(25w_0^4 + 28w_0^2 + 27)(k_x^2 + k_y^2)(\sqrt{w_0^2 + 1} - 2w_1)^2}{27(1 - 3w_0^2)^3 \sqrt{w_0^2 + 1}} (\sigma_y + \sqrt{3}\sigma_x).
 \end{aligned} \tag{F32}$$

The full fourth order Hamiltonian reads

$$\begin{aligned} & \frac{8k_x w_0 (w_0^2 + 21) (k_x^2 - 3k_y^2) (\sqrt{w_0^2 + 1} - 2w_1)}{9(3w_0^2 - 1)^3} \sigma_0 \\ & + \frac{4(k_x^2 + k_y^2) [2w_0^2 (35w_0^4 + 68w_0^2 + 9) (k_x^2 + k_y^2) - 9(w_0^2 + 1) (10w_0^4 + 9w_0^2 + 3) (2w_1 - \sqrt{w_0^2 + 1})^2]}{27(w_0^2 + 1)^{3/2} (3w_0^2 - 1)^3} (\sigma_y + \sqrt{3}\sigma_x). \end{aligned} \quad (\text{F33})$$

If $w_1 = \frac{\sqrt{1+w_0^2}}{2}$, then the expressions reduce to our previous Hamiltonian. We can label the two-band Hamiltonian as

$$H_{2\text{band}}^{\text{Hex}}(\mathbf{k}, w_0, w_1) = d_0(\mathbf{k}, w_0, w_1) \sigma_0 + d_1(\mathbf{k}, w_0, w_1) (\sigma_y + \sqrt{3}\sigma_x), \quad (\text{F34})$$

where

$$d_0(\mathbf{k}, w_0, w_1) = \frac{4k_x w_0 (w_0^2 - 3) (k_x^2 - 3k_y^2)}{9(1 - 3w_0^2)^2 \sqrt{w_0^2 + 1}} - \frac{8k_x w_0 (w_0^2 + 21) (k_x^2 - 3k_y^2) (\sqrt{w_0^2 + 1} - 2w_1)}{9(3w_0^2 - 1)^3} \sigma_0 \quad (\text{F35})$$

and

$$\begin{aligned} d_1(\mathbf{k}, w_0, w_1) = & \left(\frac{\sqrt{w_0^2 + 1}}{2} - w_1 \right) - \frac{4w_0^2 (k_x^2 + k_y^2)}{3\sqrt{w_0^2 + 1} (3w_0^2 - 1)} - \frac{2(7w_0^2 + 3) (k_x^2 + k_y^2) (\sqrt{w_0^2 + 1} - 2w_1)}{3(1 - 3w_0^2)^2} \\ & + \frac{4(k_x^2 + k_y^2) [2w_0^2 (35w_0^4 + 68w_0^2 + 9) (k_x^2 + k_y^2) - 9(w_0^2 + 1) (10w_0^4 + 9w_0^2 + 3) (2w_1 - \sqrt{w_0^2 + 1})^2]}{27(w_0^2 + 1)^{3/2} (3w_0^2 - 1)^3}, \end{aligned} \quad (\text{F36})$$

where the perturbation is made on the zero energy eigenstates of $H_{\text{Hex}}(\mathbf{k} = 0, w_0, w_1 = \frac{\sqrt{1+w_0^2}}{2})$.

Notice that so far, remarkably the eigenstates are not \mathbf{k} dependent, they are just the eigenstates of $(\sigma_y + \sqrt{3}\sigma_x)$. We did not obtain the fifth order for this Hamiltonian: due to the fact that the first order Hamiltonian does not cancel, this is not easy to do.

4. Calculations of the B1 shell first order perturbation

We now compute the shell B1 perturbation Hamiltonian:

$$\begin{aligned} & -H_{A1,B1} H_{kB1}^{-1} H_{A1,B1}^\dagger(\mathbf{k}, w_0, w_1) \\ & = - \begin{pmatrix} \frac{T_1(k-2q_1) \cdot \sigma T_1}{|k-2q_1|^2} & 0 & 0 & 0 & 0 & 0 \\ 0 & \frac{T_3(k+2q_3) \cdot \sigma T_3}{|k+2q_3|^2} & 0 & 0 & 0 & 0 \\ 0 & 0 & \frac{T_2(k-2q_2) \cdot \sigma T_2}{|k-2q_2|^2} & 0 & 0 & 0 \\ 0 & 0 & 0 & \frac{T_1(k+2q_1) \cdot \sigma T_1}{|k+2q_1|^2} & 0 & 0 \\ 0 & 0 & 0 & 0 & \frac{T_3(k-2q_3) \cdot \sigma T_3}{|k-2q_3|^2} & 0 \\ 0 & 0 & 0 & 0 & 0 & \frac{T_2(k+2q_2) \cdot \sigma T_2}{|k+2q_2|^2} \end{pmatrix}. \end{aligned} \quad (\text{F37})$$

We now compute the perturbation Hamiltonian:

$$\begin{aligned} H^{(B1)}(\mathbf{k}, w_0, w_1) & = \langle \psi_m | -H_{A1,B1} H_{kB1}^{-1} H_{A1,B1}^\dagger(\mathbf{k}, w_0, w_1) | \psi_{m'} \rangle \\ & = \frac{1}{\prod_{i=1,2,3} |k-2q_i|^2 |k+2q_i|^2} [\tilde{d}_0(\mathbf{k}, w_0, w_1) \sigma_0 + \tilde{d}_x(\mathbf{k}, w_0, w_1) \sigma_x + \tilde{d}_y(\mathbf{k}, w_0, w_1) \sigma_y + \tilde{d}_z(\mathbf{k}, w_0, w_1) \sigma_z], \end{aligned} \quad (\text{F38})$$

where

$$\tilde{d}_0(\mathbf{k}, w_0, w_1) = \frac{4k_x(k_x^2 - 3k_y^2)(k_x^2 + k_y^2 + 4)[(k_x^2 + k_y^2)^2 - 4(k_x^2 + k_y^2) + 16]w_0(\sqrt{w_0^2 + 1} + w_1 + 1)(\sqrt{w_0^2 + 1} + w_1 - 1)}{\sqrt{w_0^2 + 1}}, \quad (\text{F39})$$

$$\tilde{d}_z(\mathbf{k}, w_0, w_1) = \frac{64k_xk_y(k_x^2 - 3k_y^2)(3k_x^2 - k_y^2)w_0[(\sqrt{w_0^2 + 1}w_1 + w_0^2)^2 + w_0^2]}{(w_0^2 + 1)^{3/2}}, \quad (\text{F40})$$

$$\tilde{d}_x(\mathbf{k}, w_0, w_1) = -\frac{16(\sqrt{3}\sqrt{w_0^2 + 1}[-k_y(3k_x^2 - k_y^2)]^2 + [k_x(k_x^2 - 3k_y^2)]^2 + 64)(w_0^2 - w_1^2) - 2k_xk_y(k_x^2 - 3k_y^2)(3k_x^2 - k_y^2)(\sqrt{w_0^2 + 1}w_1^2 + 2w_0^2w_1 + \sqrt{w_0^2 + 1}w_0^2)}{w_0^2 + 1}, \quad (\text{F41})$$

$$\tilde{d}_y(\mathbf{k}, w_0, w_1) = -\frac{16\{\sqrt{w_0^2 + 1}[-k_x^2(3k_x^2 - k_y^2)]^2 + k_x^2(k_x^2 - 3k_y^2)^2 + 64\}(w_0^2 - w_1^2) + 2\sqrt{3}k_xk_y(3k_x^2 - k_y^2)(k_x^2 - 3k_y^2)(\sqrt{w_0^2 + 1}w_1^2 + 2w_0^2w_1 + \sqrt{w_0^2 + 1}w_0^2)}{w_0^2 + 1}. \quad (\text{F42})$$

This gives the first order term of $H_{\text{Approx1}}(\mathbf{k})$ projected into the zero energy bands in the hexagon model on the second magic manifold.

5. Exact eigenvalues of the one-shell model at Γ_M point

At $w_0 = 0$ we find the Γ_M point eigenenergies of the Hamiltonian $H_{\text{Approx1}} = H_{kA1} + H_{A1,A1} - H_{A1,B1}H_{kB1}^{-1}H_{A1,B1}^\dagger$ in Eq. (33) to be the following:

$$\begin{aligned} & \frac{(-w_1^2 + 4w_1 - 2)}{2}, \frac{(w_1^2 - 4w_1 + 2)}{2}, \frac{(-w_1^2 + 2w_1 - 2)}{2}, \frac{(-w_1^2 + 2w_1 - 2)}{2}, \frac{(w_1^2 - 2w_1 + 2)}{2}, \frac{(w_1^2 - 2w_1 + 2)}{2}, \\ & \frac{(-w_1^2 - 2w_1 - 2)}{2}, \frac{(-w_1^2 - 2w_1 - 2)}{2}, \frac{(w_1^2 + 2w_1 + 2)}{2}, \frac{(w_1^2 + 2w_1 + 2)}{2}, \frac{(-w_1^2 - 4w_1 - 2)}{2}, \frac{(w_1^2 + 4w_1 + 2)}{2}. \end{aligned} \quad (\text{F43})$$

One sees the Γ_M point has zero bandwidth at $w_1 = 2 - \sqrt{2}$, the same as that of the zero-bandwidth manifold $w_1 = 2\sqrt{w_0^2 + 1} - \sqrt{3w_0^2 + 2} = 2 - \sqrt{2}$ in Eq. (58) for the two-band model at $w_0 = 0$.

Furthermore, in the chiral limit $w_0 = 0$, the value $w_1 = 2\sqrt{w_0^2 + 1} - \sqrt{3w_0^2 + 2} = 2 - \sqrt{2}$ for which the bandwidth is 0 in our two-band model is in fact *exact* for the no-approximation Hamiltonian of the $n = 1$ shell Hamiltonian (of $A1, B1$ subshells). We find its eigenvalues at Γ_M to be

$$\begin{aligned} & \frac{(-\sqrt{5w_1^2 - 6w_1 + 9} - w_1 - 1)}{2}, \frac{(-\sqrt{5w_1^2 - 6w_1 + 9} - w_1 - 1)}{2}, \frac{(-\sqrt{5w_1^2 - 6w_1 + 9} + w_1 + 1)}{2}, \\ & \frac{(-\sqrt{5w_1^2 - 6w_1 + 9} + w_1 + 1)}{2}, \frac{(\sqrt{5w_1^2 - 6w_1 + 9} - w_1 - 1)}{2}, \frac{(\sqrt{5w_1^2 - 6w_1 + 9} - w_1 - 1)}{2}, \\ & \frac{(\sqrt{5w_1^2 - 6w_1 + 9} + w_1 + 1)}{2}, \frac{(\sqrt{5w_1^2 - 6w_1 + 9} + w_1 + 1)}{2}, \frac{(-\sqrt{5w_1^2 + 6w_1 + 9} - w_1 + 1)}{2}, \\ & \frac{(-\sqrt{5w_1^2 + 6w_1 + 9} - w_1 + 1)}{2}, \frac{(-\sqrt{5w_1^2 + 6w_1 + 9} + w_1 - 1)}{2}, \frac{(-\sqrt{5w_1^2 + 6w_1 + 9} + w_1 - 1)}{2}, \\ & \frac{(\sqrt{5w_1^2 + 6w_1 + 9} - w_1 + 1)}{2}, \frac{(\sqrt{5w_1^2 + 6w_1 + 9} - w_1 + 1)}{2}, \frac{(\sqrt{5w_1^2 + 6w_1 + 9} + w_1 - 1)}{2}, \\ & \frac{(\sqrt{5w_1^2 + 6w_1 + 9} + w_1 - 1)}{2}, \frac{(-\sqrt{8w_1^2 - 12w_1 + 9} - 2w_1 - 1)}{2}, \frac{(-\sqrt{8w_1^2 - 12w_1 + 9} + 2w_1 + 1)}{2}, \\ & \frac{(\sqrt{8w_1^2 - 12w_1 + 9} - 2w_1 - 1)}{2}, \frac{(\sqrt{8w_1^2 - 12w_1 + 9} + 2w_1 + 1)}{2}, \frac{(-\sqrt{8w_1^2 + 12w_1 + 9} - 2w_1 + 1)}{2}, \\ & \frac{(-\sqrt{8w_1^2 + 12w_1 + 9} - 2w_1 + 1)}{2}, \frac{(\sqrt{8w_1^2 + 12w_1 + 9} - 2w_1 + 1)}{2}, \frac{(\sqrt{8w_1^2 + 12w_1 + 9} + 2w_1 - 1)}{2}. \end{aligned} \quad (\text{F44})$$

Therefore, we see that the active bands have zero bandwidth at $w_0 = 0, w_1 = 2 - \sqrt{2}$ in the $n = 1$ shell model.

- [1] R. Bistritzer and A. H. MacDonald, Moiré bands in twisted double-layer graphene, *Proc. Natl. Acad. Sci.* **108**, 12233 (2011).
- [2] Y. Cao, V. Fatemi, A. Demir, S. Fang, S. L. Tomarken, J. Y. Luo, J. D. Sanchez-Yamagishi, K. Watanabe, T. Taniguchi, E. Kaxiras, R. C. Ashoori, and P. Jarillo-Herrero, Correlated insulator behaviour at half-filling in magic-angle graphene superlattices, *Nature (London)* **556**, 80 (2018).
- [3] Y. Cao, V. Fatemi, S. Fang, K. Watanabe, T. Taniguchi, E. Kaxiras, and P. Jarillo-Herrero, Unconventional superconductivity in magic-angle graphene superlattices, *Nature (London)* **556**, 43 (2018).
- [4] X. Lu, P. Stepanov, W. Yang, M. Xie, M. A. Aamir, I. Das, C. Urgell, K. Watanabe, T. Taniguchi, G. Zhang *et al.*, Superconductors, orbital magnets and correlated states in magic-angle bilayer graphene, *Nature (London)* **574**, 653 (2019).
- [5] M. Yankowitz, S. Chen, H. Polshyn, Y. Zhang, K. Watanabe, T. Taniguchi, D. Graf, A. F. Young, and C. R. Dean, Tuning superconductivity in twisted bilayer graphene, *Science* **363**, 1059 (2019).
- [6] A. L. Sharpe, E. J. Fox, A. W. Barnard, J. Finney, K. Watanabe, T. Taniguchi, M. A. Kastner, and D. Goldhaber-Gordon, Emergent ferromagnetism near three-quarters filling in twisted bilayer graphene, *Science* **365**, 605 (2019).
- [7] Y. Saito, J. Ge, K. Watanabe, T. Taniguchi, and A. F. Young, Independent superconductors and correlated insulators in twisted bilayer graphene, *Nat. Phys.* **16**, 926 (2020).
- [8] P. Stepanov, I. Das, X. Lu, A. Fahimniya, K. Watanabe, T. Taniguchi, F. H. L. Koppens, J. Lischner, L. Levitov, and D. K. Efetov, Untying the insulating and superconducting orders in magic-angle graphene, *Nature (London)* **583**, 375 (2020).
- [9] X. Liu, Z. Wang, K. Watanabe, T. Taniguchi, O. Vafek, and J. I. A. Li, Tuning electron correlation in magic-angle twisted bilayer graphene using Coulomb screening, *Science* **371**, 1261 (2021).
- [10] H. S. Arora, R. Polski, Y. Zhang, A. Thomson, Y. Choi, H. Kim, Z. Lin, I. Z. Wilson, X. Xu, J.-H. Chu *et al.*, Superconductivity in metallic twisted bilayer graphene stabilized by WSe₂, *Nature (London)* **583**, 379 (2020).
- [11] M. Serlin, C. L. Tschirhart, H. Polshyn, Y. Zhang, J. Zhu, K. Watanabe, T. Taniguchi, L. Balents, and A. F. Young, Intrinsic quantized anomalous Hall effect in a moiré heterostructure, *Science* **367**, 900 (2019).
- [12] Y. Cao, D. Chowdhury, D. Rodan-Legrain, O. Rubies-Bigorda, K. Watanabe, T. Taniguchi, T. Senthil, and P. Jarillo-Herrero, Strange Metal in Magic-Angle Graphene with Near Planckian Dissipation, *Phys. Rev. Lett.* **124**, 076801 (2020).
- [13] H. Polshyn, M. Yankowitz, S. Chen, Y. Zhang, K. Watanabe, T. Taniguchi, C. R. Dean, and A. F. Young, Large linear-in-temperature resistivity in twisted bilayer graphene, *Nat. Phys.* **15**, 1011 (2019).
- [14] Y. Saito, J. Ge, L. Rademaker, K. Watanabe, T. Taniguchi, D. A. Abanin, and A. F. Young, Hofstadter subband ferromagnetism and symmetry-broken Chern insulators in twisted bilayer graphene, *Nat. Phys.* **17**, 478 (2021).
- [15] I. Das, X. Lu, J. Herzog-Arbeitman, Z.-D. Song, K. Watanabe, T. Taniguchi, B. A. Bernevig, and D. K. Efetov, Symmetry-broken Chern insulators and Rashba-like Landau-level crossings in magic-angle bilayer graphene, *Nat. Phys.* (2021), doi: 10.1038/s41567-021-01186-3.
- [16] S. Wu, Z. Zhang, K. Watanabe, T. Taniguchi, and E. Y. Andrei, Chern insulators, van Hove singularities and topological flat bands in magic-angle twisted bilayer graphene, *Nat. Mater.* **20**, 488 (2021).
- [17] J. M. Park, Y. Cao, K. Watanabe, T. Taniguchi, and P. Jarillo-Herrero, Flavour Hund's coupling, Chern gaps and charge diffusivity in moiré graphene, *Nature* **592**, 43 (2021).
- [18] Y. Xie, B. Lian, B. Jäck, X. Liu, C.-L. Chiu, K. Watanabe, T. Taniguchi, B. A. Bernevig, and A. Yazdani, Spectroscopic signatures of many-body correlations in magic-angle twisted bilayer graphene, *Nature (London)* **572**, 101 (2019).
- [19] Y. Choi, J. Kemmer, Y. Peng, A. Thomson, H. Arora, R. Polski, Y. Zhang, H. Ren, J. Alicea, G. Refael *et al.*, Electronic correlations in twisted bilayer graphene near the magic angle, *Nat. Phys.* **15**, 1174 (2019).
- [20] A. Kerelsky, L. J. McGilly, D. M. Kennes, L. Xian, M. Yankowitz, S. Chen, K. Watanabe, T. Taniguchi, J. Hone, C. Dean *et al.*, Maximized electron interactions at the magic angle in twisted bilayer graphene, *Nature (London)* **572**, 95 (2019).
- [21] Y. Jiang, X. Lai, K. Watanabe, T. Taniguchi, K. Haule, J. Mao, and E. Y. Andrei, Charge order and broken rotational symmetry in magic-angle twisted bilayer graphene, *Nature (London)* **573**, 91 (2019).
- [22] D. Wong, K. P. Nuckolls, M. Oh, B. Lian, Y. Xie, S. Jeon, K. Watanabe, T. Taniguchi, B. A. Bernevig, and A. Yazdani, Cascade of electronic transitions in magic-angle twisted bilayer graphene, *Nature (London)* **582**, 198 (2020).
- [23] U. Zondiner, A. Rozen, D. Rodan-Legrain, Y. Cao, R. Queiroz, T. Taniguchi, K. Watanabe, Y. Oreg, F. von Oppen, A. Stern *et al.*, Cascade of phase transitions and Dirac revivals in magic-angle graphene, *Nature (London)* **582**, 203 (2020).
- [24] K. P. Nuckolls, M. Oh, D. Wong, B. Lian, K. Watanabe, T. Taniguchi, B. A. Bernevig, and A. Yazdani, Strongly correlated Chern insulators in magic-angle twisted bilayer graphene, *Nature (London)* **588**, 610 (2020).
- [25] Y. Choi, H. Kim, Y. Peng, A. Thomson, C. Lewandowski, R. Polski, Y. Zhang, H. S. Arora, K. Watanabe, T. Taniguchi, J. Alicea, and S. Nadj-Perge, Tracing out correlated Chern insulators in magic angle twisted bilayer graphene, [arXiv:2008.11746](https://arxiv.org/abs/2008.11746).
- [26] Y. Saito, F. Yang, J. Ge, X. Liu, T. Taniguchi, K. Watanabe, J. I. A. Li, E. Berg, and A. F. Young, Isospin Pomeranchuk effect in twisted bilayer graphene, *Nature* **592**, 220 (2021).
- [27] A. Rozen, J. M. Park, U. Zondiner, Y. Cao, D. Rodan-Legrain, T. Taniguchi, K. Watanabe, Y. Oreg, A. Stern, E. Berg, P. Jarillo-Herrero, and S. Ilani, Entropic evidence for a Pomeranchuk effect in magic-angle graphene, *Nature* **592**, 214 (2021).
- [28] X. Lu, B. Lian, G. Chaudhary, B. A. Piot, G. Romagnoli, K. Watanabe, T. Taniguchi, M. Poggio, A. H. MacDonald, B. A. Bernevig, and D. K. Efetov, Fingerprints of fragile topology in the Hofstadter spectrum of twisted bilayer graphene close to the second magic angle, [arXiv:2006.13963](https://arxiv.org/abs/2006.13963).
- [29] G. W. Burg, J. Zhu, T. Taniguchi, K. Watanabe, A. H. MacDonald, and E. Tutuc, Correlated Insulating States in Twisted Double Bilayer Graphene, *Phys. Rev. Lett.* **123**, 197702 (2019).

- [30] C. Shen, Y. Chu, Q. Wu, N. Li, S. Wang, Y. Zhao, J. Tang, J. Liu, J. Tian, K. Watanabe, T. Taniguchi, R. Yang, Z. Y. Meng, D. Shi, O. V. Yazyev, and G. Zhang, Correlated states in twisted double bilayer graphene, *Nat. Phys.* **16**, 520 (2020).
- [31] Y. Cao, D. Rodan-Legrain, O. Rubies-Bigorda, J. M. Park, K. Watanabe, T. Taniguchi, and P. Jarillo-Herrero, Tunable correlated states and spin-polarized phases in twisted bilayer-graphene, *Nature (London)* **583**, 215 (2020).
- [32] X. Liu, Z. Hao, E. Khalaf, J. Y. Lee, K. Watanabe, T. Taniguchi, A. Vishwanath, and P. Kim, Spin-polarized correlated insulator and superconductor in twisted double bilayer graphene, *Nature (London)* **583**, 221 (2020).
- [33] G. Chen, L. Jiang, S. Wu, B. Lyu, H. Li, B. L. Chittari, K. Watanabe, T. Taniguchi, Z. Shi, J. Jung, Y. Zhang, and F. Wang, Evidence of a gate-tunable Mott insulator in a trilayer graphene moiré superlattice, *Nat. Phys.* **15**, 237 (2019).
- [34] G. Chen, A. L. Sharpe, P. Gallagher, I. T. Rosen, E. J. Fox, L. Jiang, B. Lyu, H. Li, K. Watanabe, T. Taniguchi, J. Jung, Z. Shi, D. Goldhaber-Gordon, Y. Zhang, and F. Wang, Signatures of tunable superconductivity in a trilayer graphene moiré superlattice, *Nature (London)* **572**, 215 (2019).
- [35] G. Chen, A. L. Sharpe, E. J. Fox, Y.-H. Zhang, S. Wang, L. Jiang, B. Lyu, H. Li, K. Watanabe, T. Taniguchi, Z. Shi, T. Senthil, D. Goldhaber-Gordon, Y. Zhang, and F. Wang, Tunable correlated Chern insulator and ferromagnetism in a moiré superlattice, *Nature (London)* **579**, 56 (2020).
- [36] G. W. Burg, B. Lian, T. Taniguchi, K. Watanabe, B. A. Bernevig, and E. Tutuc, Evidence of emergent symmetry and valley Chern number in twisted double-bilayer graphene, [arXiv:2006.14000](https://arxiv.org/abs/2006.14000).
- [37] G. Tarnopolsky, A. J. Kruchkov, and A. Vishwanath, Origin of Magic Angles in Twisted Bilayer Graphene, *Phys. Rev. Lett.* **122**, 106405 (2019).
- [38] L. Zou, H. C. Po, A. Vishwanath, and T. Senthil, Band structure of twisted bilayer graphene: Emergent symmetries, commensurate approximants, and Wannier obstructions, *Phys. Rev. B* **98**, 085435 (2018).
- [39] Y. Fu, E. J. König, J. H. Wilson, Y.-Z. Chou, and J. H. Pixley, Magic-angle semimetals, *npj Quantum Mater.* **5**, 71 (2020).
- [40] J. Liu, J. Liu, and X. Dai, Pseudo Landau level representation of twisted bilayer graphene: Band topology and implications on the correlated insulating phase, *Phys. Rev. B* **99**, 155415 (2019).
- [41] D. K. Efimkin and A. H. MacDonald, Helical network model for twisted bilayer graphene, *Phys. Rev. B* **98**, 035404 (2018).
- [42] J. Kang and O. Vafek, Symmetry, Maximally Localized Wannier States, and a Low-Energy Model for Twisted Bilayer Graphene Narrow Bands, *Phys. Rev. X* **8**, 031088 (2018).
- [43] Z. Song, Z. Wang, W. Shi, G. Li, C. Fang, and B. A. Bernevig, All Magic Angles in Twisted Bilayer Graphene are Topological, *Phys. Rev. Lett.* **123**, 036401 (2019).
- [44] H. C. Po, L. Zou, T. Senthil, and A. Vishwanath, Faithful tight-binding models and fragile topology of magic-angle bilayer graphene, *Phys. Rev. B* **99**, 195455 (2019).
- [45] J. Ahn, S. Park, and B.-J. Yang, Failure of Nielsen-Ninomiya Theorem and Fragile Topology in Two-Dimensional Systems with Space-Time Inversion Symmetry: Application to Twisted Bilayer Graphene at Magic Angle, *Phys. Rev. X* **9**, 021013 (2019).
- [46] A. Bouhon, A. M. Black-Schaffer, and R.-J. Slager, Wilson loop approach to fragile topology of split elementary band representations and topological crystalline insulators with time-reversal symmetry, *Phys. Rev. B* **100**, 195135 (2019).
- [47] B. Lian, F. Xie, and B. A. Bernevig, Landau level of fragile topology, *Phys. Rev. B* **102**, 041402(R) (2020).
- [48] K. Hejazi, C. Liu, H. Shapourian, X. Chen, and L. Balents, Multiple topological transitions in twisted bilayer graphene near the first magic angle, *Phys. Rev. B* **99**, 035111 (2019).
- [49] K. Hejazi, C. Liu, and L. Balents, Landau levels in twisted bilayer graphene and semiclassical orbits, *Phys. Rev. B* **100**, 035115 (2019).
- [50] B. Padhi, A. Tiwari, T. Neupert, and S. Ryu, Transport across twist angle domains in moiré graphene, *Phys. Rev. Research* **2**, 033458 (2020).
- [51] C. Xu and L. Balents, Topological Superconductivity in Twisted Multilayer Graphene, *Phys. Rev. Lett.* **121**, 087001 (2018).
- [52] M. Koshino, N. F. Q. Yuan, T. Koretsune, M. Ochi, K. Kuroki, and L. Fu, Maximally Localized Wannier Orbitals and the Extended Hubbard Model for Twisted Bilayer Graphene, *Phys. Rev. X* **8**, 031087 (2018).
- [53] M. Ochi, M. Koshino, and K. Kuroki, Possible correlated insulating states in magic-angle twisted bilayer graphene under strongly competing interactions, *Phys. Rev. B* **98**, 081102(R) (2018).
- [54] X. Y. Xu, K. T. Law, and P. A. Lee, Kekulé valence bond order in an extended Hubbard model on the honeycomb lattice with possible applications to twisted bilayer graphene, *Phys. Rev. B* **98**, 121406(R) (2018).
- [55] F. Guinea and N. R. Walet, Electrostatic effects, band distortions, and superconductivity in twisted graphene bilayers, *Proc. Natl. Acad. Sci.* **115**, 13174 (2018).
- [56] J. W. F. Venderbos and R. M. Fernandes, Correlations and electronic order in a two-orbital honeycomb lattice model for twisted bilayer graphene, *Phys. Rev. B* **98**, 245103 (2018).
- [57] Y.-Z. You and A. Vishwanath, Superconductivity from valley fluctuations and approximate SO(4) symmetry in a weak coupling theory of twisted bilayer graphene, *npj Quantum Mater.* **4**, 16 (2019).
- [58] F. Wu and S. Das Sarma, Collective Excitations of Quantum Anomalous Hall Ferromagnets in Twisted Bilayer Graphene, *Phys. Rev. Lett.* **124**, 046403 (2020).
- [59] B. Lian, Z. Wang, and B. A. Bernevig, Twisted Bilayer Graphene: A Phonon-Driven Superconductor, *Phys. Rev. Lett.* **122**, 257002 (2019).
- [60] F. Wu, A. H. MacDonald, and I. Martin, Theory of Phonon-Mediated Superconductivity in Twisted Bilayer Graphene, *Phys. Rev. Lett.* **121**, 257001 (2018).
- [61] H. Isobe, N. F. Q. Yuan, and L. Fu, Unconventional Superconductivity and Density Waves in Twisted Bilayer Graphene, *Phys. Rev. X* **8**, 041041 (2018).
- [62] C.-C. Liu, L.-D. Zhang, W.-Q. Chen, and F. Yang, Chiral Spin Density Wave and d+ i d Superconductivity in the Magic-Angle-Twisted Bilayer Graphene, *Phys. Rev. Lett.* **121**, 217001 (2018).

- [63] N. Bultinck, S. Chatterjee, and M. P. Zaletel, Mechanism for Anomalous Hall Ferromagnetism in Twisted Bilayer Graphene, *Phys. Rev. Lett.* **124**, 166601 (2020).
- [64] Y.-H. Zhang, D. Mao, Y. Cao, P. Jarillo-Herrero, and T. Senthil, Nearly flat Chern bands in moiré superlattices, *Phys. Rev. B* **99**, 075127 (2019).
- [65] J. Liu, Z. Ma, J. Gao, and X. Dai, Quantum Valley Hall Effect, Orbital Magnetism, and Anomalous Hall Effect in Twisted Multilayer Graphene Systems, *Phys. Rev. X* **9**, 031021 (2019).
- [66] X.-C. Wu, C.-M. Jian, and C. Xu, Coupled-wire description of the correlated physics in twisted bilayer graphene, *Phys. Rev. B* **99**, 161405(R) (2019).
- [67] A. Thomson, S. Chatterjee, S. Sachdev, and M. S. Scheurer, Triangular antiferromagnetism on the honeycomb lattice of twisted bilayer graphene, *Phys. Rev. B* **98**, 075109 (2018).
- [68] J. F. Dodaro, S. A. Kivelson, Y. Schattner, X.-Q. Sun, and C. Wang, Phases of a phenomenological model of twisted bilayer graphene, *Phys. Rev. B* **98**, 075154 (2018).
- [69] J. Gonzalez and T. Stauber, Kohn-Luttinger Superconductivity in Twisted Bilayer Graphene, *Phys. Rev. Lett.* **122**, 026801 (2019).
- [70] N. F. Q. Yuan and L. Fu, Model for the metal-insulator transition in graphene superlattices and beyond, *Phys. Rev. B* **98**, 045103 (2018).
- [71] J. Kang and O. Vafek, Strong Coupling Phases of Partially Filled Twisted Bilayer Graphene Narrow Bands, *Phys. Rev. Lett.* **122**, 246401 (2019).
- [72] N. Bultinck, E. Khalaf, S. Liu, S. Chatterjee, A. Vishwanath, and M. P. Zaletel, Ground State and Hidden Symmetry of Magic-Angle Graphene at Even Integer Filling, *Phys. Rev. X* **10**, 031034 (2020).
- [73] K. Seo, V. N. Kotov, and B. Uchoa, Ferromagnetic Mott State in Twisted Graphene Bilayers at the Magic Angle, *Phys. Rev. Lett.* **122**, 246402 (2019).
- [74] K. Hejazi, X. Chen, and L. Balents, Hybrid Wannier Chern bands in magic angle twisted bilayer graphene and the quantized anomalous Hall effect, *Phys. Rev. Research* **3**, 013242 (2021).
- [75] E. Khalaf, S. Chatterjee, N. Bultinck, M. P. Zaletel, and A. Vishwanath, Charged skyrmions and topological origin of superconductivity in magic angle graphene, *arXiv:2004.00638*.
- [76] H. C. Po, L. Zou, A. Vishwanath, and T. Senthil, Origin of Mott Insulating Behavior and Superconductivity in Twisted Bilayer Graphene, *Phys. Rev. X* **8**, 031089 (2018).
- [77] F. Xie, Z. Song, B. Lian, and B. A. Bernevig, Topology-Bounded Superfluid Weight in Twisted Bilayer Graphene, *Phys. Rev. Lett.* **124**, 167002 (2020).
- [78] A. Julku, T. J. Peltonen, L. Liang, T. T. Heikkilä, and P. Törmä, Superfluid weight and Berezinskii-Kosterlitz-Thouless transition temperature of twisted bilayer graphene, *Phys. Rev. B* **101**, 060505(R) (2020).
- [79] X. Hu, T. Hyart, D. I. Pikulin, and E. Rossi, Geometric and Conventional Contribution to the Superfluid Weight in Twisted Bilayer Graphene, *Phys. Rev. Lett.* **123**, 237002 (2019).
- [80] J. Kang and O. Vafek, Non-Abelian Dirac node braiding and near-degeneracy of correlated phases at odd integer filling in magic-angle twisted bilayer graphene, *Phys. Rev. B* **102**, 035161 (2020).
- [81] T. Soejima, D. E. Parker, N. Bultinck, J. Hauschild, and M. P. Zaletel, Efficient simulation of moire materials using the density matrix renormalization group, *Phys. Rev. B* **102**, 205111 (2020).
- [82] J. H. Pixley and E. Y. Andrei, Ferromagnetism in magic-angle graphene, *Science* **365**, 543 (2019).
- [83] E. J. König, P. Coleman, and A. M. Tsvelik, Spin magnetometry as a probe of stripe superconductivity in twisted bilayer graphene, *Phys. Rev. B* **102**, 104514 (2020).
- [84] M. Christos, S. Sachdev, and M. Scheurer, Superconductivity, correlated insulators, and Wess-Zumino-Witten terms in twisted bilayer graphene, *Proc. Natl. Acad. Sci.* **117**, 29543 (2020).
- [85] C. Lewandowski, D. Chowdhury, and J. Ruhman, Pairing in magic-angle twisted bilayer graphene: Role of phonon and plasmon umklapp, *arXiv:2007.15002*.
- [86] M. Xie and A. H. MacDonald, Nature of the Correlated Insulator States in Twisted Bilayer Graphene, *Phys. Rev. Lett.* **124**, 097601 (2020).
- [87] J. Liu and X. Dai, Theories for the correlated insulating states and quantum anomalous Hall phenomena in twisted bilayer graphene, *Phys. Rev. B* **103**, 035427 (2021).
- [88] T. Cea and F. Guinea, Band structure and insulating states driven by Coulomb interaction in twisted bilayer graphene, *Phys. Rev. B* **102**, 045107 (2020).
- [89] Y. Zhang, K. Jiang, Z. Wang, and F. Zhang, Correlated insulating phases of twisted bilayer graphene at commensurate filling fractions: A Hartree-Fock study, *Phys. Rev. B* **102**, 035136 (2020).
- [90] S. Liu, E. Khalaf, J. Y. Lee, and A. Vishwanath, Nematic topological semimetal and insulator in magic angle bilayer graphene at charge neutrality, *Phys. Rev. Research* **3**, 013033 (2021).
- [91] Y. Da Liao, Z. Y. Meng, and X. Y. Xu, Valence Bond Orders at Charge Neutrality in a Possible Two-Orbital Extended Hubbard Model for Twisted Bilayer Graphene, *Phys. Rev. Lett.* **123**, 157601 (2019).
- [92] Y. D. Liao, J. Kang, C. N. Breið, X. Y. Xu, H.-Q. Wu, B. M. Andersen, R. M. Fernandes, and Z. Y. Meng, Correlation-Induced Insulating Topological Phases at Charge Neutrality in Twisted Bilayer Graphene, *Phys. Rev. X* **11**, 011014 (2021).
- [93] L. Classen, C. Honerkamp, and M. M. Scherer, Competing phases of interacting electrons on triangular lattices in moiré heterostructures, *Phys. Rev. B* **99**, 195120 (2019).
- [94] D. M. Kennes, J. Lischner, and C. Karrasch, Strong correlations and d+id superconductivity in twisted bilayer graphene, *Phys. Rev. B* **98**, 241407(R) (2018).
- [95] P. M. Eugenio and C. B. Dağ, DMRG study of strongly interacting z_2 flatbands: A toy model inspired by twisted bilayer graphene, *SciPost Phys. Core* **3**, 015 (2020).
- [96] Y. Huang, P. Hosur, and H. K. Pal, Deconstructing magic-angle physics in twisted bilayer graphene with a two-leg ladder model, *Phys. Rev. B* **102**, 155429 (2020).
- [97] T. Huang, L. Zhang, and T. Ma, Antiferromagnetically ordered Mott insulator and d+id superconductivity in twisted bilayer graphene: A quantum Monte Carlo study, *Sci. Bull.* **64**, 310 (2019).
- [98] H. Guo, X. Zhu, S. Feng, and R. T. Scalettar, Pairing symmetry of interacting fermions on a twisted bilayer graphene superlattice, *Phys. Rev. B* **97**, 235453 (2018).

- [99] P. J. Ledwith, G. Tarnopolsky, E. Khalaf, and A. Vishwanath, Fractional Chern insulator states in twisted bilayer graphene: An analytical approach, *Phys. Rev. Research* **2**, 023237 (2020).
- [100] C. Repellin, Z. Dong, Y.-H. Zhang, and T. Senthil, Ferromagnetism in Narrow Bands of Moiré Superlattices, *Phys. Rev. Lett.* **124**, 187601 (2020).
- [101] A. Abouelkomsan, Z. Liu, and E. J. Bergholtz, Particle-Hole Duality, Emergent Fermi Liquids, and Fractional Chern Insulators in Moiré Flatbands, *Phys. Rev. Lett.* **124**, 106803 (2020).
- [102] C. Repellin and T. Senthil, Chern bands of twisted bilayer graphene: Fractional Chern insulators and spin phase transition, *Phys. Rev. Research* **2**, 023238 (2020).
- [103] O. Vafek and J. Kang, Towards the Hidden Symmetry in Coulomb Interacting Twisted Bilayer Graphene: Renormalization Group Approach, *Phys. Rev. Lett.* **125**, 257602 (2020).
- [104] R. M. Fernandes and J. W. F. Venderbos, Nematicity with a twist: Rotational symmetry breaking in a moiré superlattice, *Sci. Adv.* **6**, eaba8834 (2020).
- [105] J. H. Wilson, Y. Fu, S. Das Sarma, and J. H. Pixley, Disorder in twisted bilayer graphene, *Phys. Rev. Research* **2**, 023325 (2020).
- [106] J. Wang, Y. Zheng, A. J. Millis, and J. Cano, Chiral approximation to twisted bilayer graphene: Exact intra-valley inversion symmetry, nodal structure and implications for higher magic angles, [arXiv:2010.03589](https://arxiv.org/abs/2010.03589).
- [107] Z.-D. Song, B. Lian, N. Regnault, and B. A. Bernevig, Twisted bilayer graphene. II. Stable symmetry anomaly, *Phys. Rev. B* **103**, 205412 (2021).
- [108] B. A. Bernevig, Z.-D. Song, N. Regnault, and B. Lian, Twisted bilayer graphene. III. Interacting Hamiltonian and exact symmetries, *Phys. Rev. B* **103**, 205413 (2021).
- [109] B. Lian, Z.-D. Song, N. Regnault, D. K. Efetov, A. Yazdani, and B. A. Bernevig, Twisted bilayer graphene. IV. Exact insulator ground states and phase diagram, *Phys. Rev. B* **103**, 205414 (2021).
- [110] B. A. Bernevig, B. Lian, A. Cowsik, F. Xie, N. Regnault, and Z.-D. Song, Twisted bilayer graphene. V. Exact analytic many-body excitations in Coulomb Hamiltonians: Charge gap, Goldstone modes, and absence of Cooper pairing, *Phys. Rev. B* **103**, 205415 (2021).
- [111] F. Xie, A. Cowsik, Z.-D. Song, B. Lian, B. A. Bernevig, and N. Regnault, Twisted bilayer graphene. VI. An exact diagonalization study at nonzero integer filling, *Phys. Rev. B* **103**, 205416 (2021).
- [112] C. Mora, N. Regnault, and B. A. Bernevig, Flatbands and Perfect Metal in Trilayer Moiré Graphene, *Phys. Rev. Lett.* **123**, 026402 (2019).
- [113] K. Uchida, S. Furuya, J.-I. Iwata, and A. Oshiyama, Atomic corrugation and electron localization due to moiré patterns in twisted bilayer graphenes, *Phys. Rev. B* **90**, 155451 (2014).
- [114] M. M. van Wijk, A. Schuring, M. I. Katsnelson, and A. Fasolino, Relaxation of moiré patterns for slightly misaligned identical lattices: Graphene on graphite, *2D Mater.* **2**, 034010 (2015).
- [115] S. Dai, Y. Xiang, and D. J. Srolovitz, Twisted bilayer graphene: Moiré with a twist, *Nano Lett.* **16**, 5923 (2016).
- [116] S. K. Jain, V. Juričić, and G. T. Barkema, Structure of twisted and buckled bilayer graphene, *2D Mater.* **4**, 015018 (2016).
- [117] H. C. Po, H. Watanabe, and A. Vishwanath, Fragile Topology and Wannier Obstructions, *Phys. Rev. Lett.* **121**, 126402 (2018).
- [118] J. Cano, B. Bradlyn, Z. Wang, L. Elcoro, M. G. Vergniory, C. Felser, M. I. Aroyo, and B. A. Bernevig, Topology of Disconnected Elementary Band Representations, *Phys. Rev. Lett.* **120**, 266401 (2018).
- [119] J. Jung, A. Raoux, Z. Qiao, and A. H. MacDonald, *Ab initio* theory of moiré superlattice bands in layered two-dimensional materials, *Phys. Rev. B* **89**, 205414 (2014).
- [120] S. Carr, S. Fang, Z. Zhu, and E. Kaxiras, Exact continuum model for low-energy electronic states of twisted bilayer graphene, *Phys. Rev. Research* **1**, 013001 (2019).
- [121] M. Koshino and N. N. T. Nam, Effective continuum model for relaxed twisted bilayer graphene and moiré electron-phonon interaction, *Phys. Rev. B* **101**, 195425 (2020).
- [122] Z. Bi, N. F. Q. Yuan, and L. Fu, Designing flat bands by strain, *Phys. Rev. B* **100**, 035448 (2019).
- [123] R. Winkler, Quasi-degenerate perturbation theory, *Spin-Orbit Coupling Effects in Two-Dimensional Electron and Hole Systems* (Springer, New York, 2003), p. 201.